

LUND UNIVERSITY

Mechanical behaviour of glassy polymers: experiments and modelling

Engqvist, Jonas

2016

Document Version:
Publisher's PDF, also known as Version of record

Link to publication

Citation for published version (APA):
Engqvist, J. (2016). *Mechanical behaviour of glassy polymers: experiments and modelling*. Division of Solid Mechanics.

Total number of authors:
1

General rights
Unless other specific re-use rights are stated the following general rights apply:
Copyright and moral rights for the publications made accessible in the public portal are retained by the authors and/or other copyright owners and it is a condition of accessing publications that users recognise and abide by the legal requirements associated with these rights.
• Users may download and print one copy of any publication from the public portal for the purpose of private study or research.
• You may not further distribute the material or use it for any profit-making activity or commercial gain
• You may freely distribute the URL identifying the publication in the public portal

Read more about Creative commons licenses: https://creativecommons.org/licenses/

Take down policy
If you believe that this document breaches copyright please contact us providing details, and we will remove access to the work immediately and investigate your claim.

LUND UNIVERSITY

PO Box 117
221 00 Lund
+46 46-222 00 00

Department of Construction Sciences
Solid Mechanics

ISRN LUTFD2/TFHF-16/1054-SE(1-134)
ISBN: 978-91-7623-816-5 (print)
ISBN: 978-91-7623-817-2 (pdf)

Mechanical behaviour of glassy polymers: experiments and modelling

Doctoral Dissertation by

Jonas Engqvist

Copyright © 2016 by Jonas Engqvist
Printed by Media-Tryck AB, Lund, Sweden
For information, adress:
Division of Solid Mechanics, Lund University, Box 118, SE-221 00 Lund, Sweden
Homepage: http://www.solid.lth.se

Till Kajsa, mina syskon och mina föräldrar

Preface

This thesis is the result of my Ph.D studies conducted at the Division of Solid Mechanics at Lund University between summer 2012 and spring 2016.

First and foremost I would like to take the opportunity to thank my main supervisor Prof. Mathias Wallin without whom I seriously doubt that this thesis would have been written. Mathias introduced me to the research topic and has been of invaluable assistance during my scientific work conducted at the division so far. I would also like to direct a heartfelt thanks to my co-supervisors Assoc. Prof. Stephen Hall and Prof. Matti Ristinmaa. Without Stephen, it is safe to assume that the experimental part of this thesis would rapidly been approaching zero. As a consequence of this, the work leading up to this thesis would had been very different and, I will have to admit, not as fun and interesting. Our technician Zivorad Zivkovic deserves a special thanks for his hard work and craftsmanship building the test devices used within this work, and his patience with the requests (which were not always well defined) during the experimental work. My fellow Ph.D students and the rest of the staff at the Division of Solid Mechanics all deserve a big thanks for making the time at the division so joyful. Sara and Johan both deserve a special thanks for all the interesting and fruitful discussions over the years, as well as all the fun at, and outside, of work. Finally, I want to thank my family, and especially Kajsa, for helping me to fill my spare time with things other than the mechanics of polymers.

Lejons, May 1st 2016.

Jonas Engqvist

Abstract

This thesis presents experimental investigation and modelling of the mechanical response of glassy polycarbonate (PC) during deformation. The mechanical response is studied experimentally over a wide range of length-scales using X-ray scattering techniques and optical full-field deformation measurement by Digital Image Correlation (DIC). Results from the experimental work have been used to develop an elasto-viscoplastic model for glassy polymers. The thesis includes an introductory section on glassy polymers, aspects of the experimental procedures and a summary of the key aspects of the constitutive modelling, and four papers.

An experimental method combining X-ray scattering, full-field DIC and tensile loading has been developed and used within this thesis. Details about the experimental method are presented in Paper A. By combining the, individually well established, experimental techniques, the deformation of a material can be studied simultaneously over a wide range of length-scales, from the macroscopic response down to the behaviour of the molecular structure. Results from experiments performed using the developed method are also presented in Paper B. Novel observations of the deformation and reorientation of the microstructure of glassy PC are presented and related to relevant local macroscopic measures of deformation.

The experimental results presented in Paper B have been used to develop a constitutive model for glassy polymers in Paper C. A separate microstructural deformation gradient is introduced to model the deformation of the polymer network. Moreover, the reorientation of the microstructure, shown in Paper B, is introduced by an evolution of the directions of the network chains. By incorporating the evolving reorientation and the deformation of the microstructure shown by the experiments, the model is able to capture the deformation at the macroscopic, the mesoscopic and the microscopic levels.

In Paper D, the mechanical behaviour of glassy PC is studied using biaxial tension loading and DIC. The experiments performed in Paper D show a significant influence of the multi-axial loading on the localisation behaviour. It is also found that the commonly used quadratic form of the elastic free energy results in a too stiff initial response during biaxial loading. To this end, a new format for the volumetric part of the elastic free energy is proposed which results in a softer response with increasing volumetric deformation. The proposed format also improves the ability to capture the non-linear, pre-peak behaviour exhibited by PC.

Sammanfattning

Polymerer används ofta som konstruktionsmaterial i såväl konsument- som industriprodukter. För att säkerställa att produkten klarar av de mekaniska påfrestningar den kan komma att utsättas för under dess livstid är det viktigt att förstå hur materialet beter sig under olika belastningsförhållanden. Då polymerer oftast framställs från icke förnyelsebar råvaror är det även viktigt att förstå, och kunna förutse, dess beteende så att en produkt utformas så att den är hållbar utan att mer material än nödvändigt förbrukas vid framställningen. Såväl experimentell verksamhet, som teoretiska modeller är viktiga verktyg för att öka kunskapen om ett materials beteende.

Inom ramen för detta forskningsprojekt har en testmetod utvecklats vilken kombinerar avancerade experimentella tekniker för att undersöka det mekaniska beteendet hos material. Röntgenspridningsmetoder har använts för att studera hur den molekylär strukturen inuti material deformeras. Samtidigt som röntgenstrålningen används för att mäta molekylernas rörelse mäts deformationen på ytan av provbiten med två kameror kalibrerade för djupseende. Genom att kombinera olika tekniker kan ett enda experiment ge stora mängder information, från hur provbiten som helhet beter sig ända ner till hur molekylerna inuti materialet rör sig. På detta sätt kan deformationen på olika längdskalor i materialet kopplas samman. Kunskapen om deformationen på olika nivåer i material kan sedan användas för att förklara olika deformationsfenomen och även för att etablera noggrannare teoretiska modeller för att förutse det mekaniska beteendet hos ett material.

Detta forskningsprojekt har fokuserat på polymerer i glastillstånd och främst polykarbonat. Experiment utförda med den, inom projektet, utvecklade testmetoden har visat på hur molekylerna i polykarbonat orienteras under deformation. Denna uppkomna orientering kvarstår efter att provbiten avlastats viket visar att den molekylära strukturen av material har deformerats permanent. Förutom detta har även experimenten visat på att molekylerna i materialet sträcks då provbiten belastas. Till skillnad från orienteringen av molekylstrukturen kvarstår inte förlängningen av molekylerna efter att provbiten avlastats.

Information från experimenten som genomförts med den framtagna metoden har använts för att utveckla en teoretisk modell för att beskriva och förutse det mekaniska beteendet hos polymerer i glastillstånd. Modellen innehåller en evolution av orienteringen av mikrostrukturen likt den som observerats experimentellt. Genom att inkludera den permanenta orienteringen av molekylstrukturen förmår modellen att prediktera det mekaniska beteendet av polykarbonat från det makroskopiska ner till mikrostrukturen.

List of appended papers

This doctoral thesis is based on the following manuscripts:

Paper A
Jonas Engqvist, Stephen Hall, Mathias Wallin, Matti Ristinmaa and Tomás Plivelic (2014)
Multi-scale measurement of (amorphous) polymer deformation: simultaneous X-ray scattering, digital image correlation and in-situ loading.
Experimental Mechanics, 54 (2014) 1373-1383

Paper B
Jonas Engqvist, Mathias Wallin, Stephen Hall, Matti Ristinmaa and Tomás Plivelic (2014)
Measurement of multi-scale deformation of polycarbonate using X-ray scattering with in-situ loading and digital image correlation.
Polymer, 82 (2016) 190-197

Paper C
Jonas Engqvist, Mathias Wallin, Matti Ristinmaa, Stephen Hall and Tomás Plivelic (2016)
Modelling multi-scale deformation of amorphous glassy polymers with experimentally motivated evolution of the microstructure
Submitted for international publication

Paper D
Jonas Engqvist, Mathias Wallin, Matti Ristinmaa and Stephen Hall (2016)
Modelling and experiments of glassy polymers using biaxial loading and digital image correlation
To be submitted for publication

Own Contribution. The author of this thesis has taken the main responsibility for the preparation and writing of all papers. In all papers, the development of the model and analysis of results have been conducted in collaborations with the co-authors. The numerical implementation has been made by the author. The experimental measurements in Paper D have been carried out by the main author while the experimental measurements in Paper A and Paper B have been carried out by the main author in collaboration with the co-authors.

Contents

1 Introduction **1**

2 Mechanical characterisation of polymers **2**

3 Experimental method **6**
3.1 Material and specimens 6
3.2 Macroscopic loading 6
3.3 Mesoscopic deformation measurement using DIC 9
3.4 Microscopic deformation measured using X-ray scattering 10

4 Constitutive modelling of glassy polymers **13**
4.1 Kinematic framework for the continuum 14
4.2 Kinematic framework for the microstructure 15
4.3 Thermodynamic framework 16
4.4 Elasticity 16
4.5 Viscoplasticity 17

5 Summary **18**

6 Future work **18**

7 Summary of the papers **19**

Paper A

Paper B

Paper C

Paper D

1 Introduction

In an amorphous state, polymer chains are randomly distributed, as opposed to a crystalline state where the chains are highly ordered, see Figure 1. The lack of order in an amorphous state implies that the onset of molecular motion can take place at a temperature, the glass transition temperature, that is lower than the melting point for the crystallites, cf. Cowie and Arrighi (2007). In a glassy state, i.e., at temperatures lower than the glass transition temperature, the mobility of the polymer chains is low resulting in a relatively stiff and brittle material. When the molecular motion increases, as the temperature increases, the physical properties change and the polymer undergoes a transition from a glassy state, through a rubber-like state until it melts.

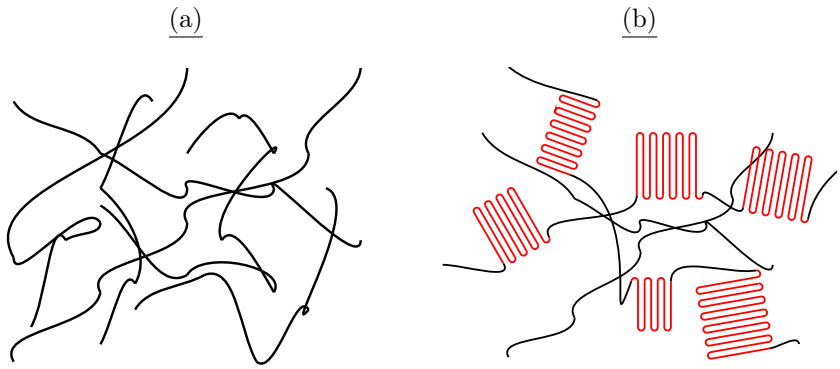

Figure 1: Schematic of the chain structure of an amorphous polymer (a) and a semi-crystalline polymer (b).

Glassy polymers are, due to their favourable mechanical and manufacturing properties, commonly used as, e.g., containers or substitute for glass in the electronics and automotive industry, machine guards and safety glass. Since glassy polymers, such as polycarbonate (PC) at room temperature, are used in load carrying structures, they are subjected to complex loading patterns, which may result in deformation phenomena such as necking, deformation hardening and evolving anisotropy. The ability to accurately predict these deformation phenomena is evidently of great importance when simulating the mechanical response of polymer structures.

To characterise the mechanical behaviour of a material, or to evaluate the mechanical performance of a product, experimental testing can be conducted. It may, however, be difficult as well as time consuming to design an experiment to probe the desired property of the material and to fully understand the outcome of the experiment. To this end, theoretical modelling can be of great importance to increase the understanding and ability to predict the behaviour of a structure. In this work, experimental testing has been carried out to investigate the mechanical behaviour of glassy PC. The experiments involved *in-situ* uni-axial tensile tests during X-ray scattering experiments and biaxial tensile tests. Furthermore, the experimental results have been used to develop a theoretical model to

describe the mechanical behaviour of glassy polymers.

2 Mechanical characterisation of polymers

To characterise the mechanical behaviour of a material, experimental testing needs to be conducted. The mechanical response of polymers is often characterised by the macroscopic response from tension or compression tests where the deformation is measured at the boundaries of the specimen or locally using strain gauges or extensometers, e.g., Treloar (1944); G'sell and Jonas (1979); Arruda et al. (1995); Dreistadt et al. (2009); Ames et al. (2009). The output of such a test is a single force-displacement (or equivalently stress-strain) curve, see Figure 2.

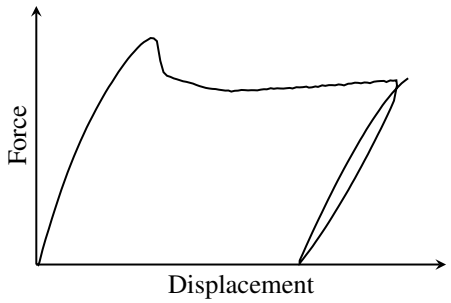

Figure 2: Characteristic macroscopic force-displacement curve from a uni-axial tensile test, using a symmetrically notched polycarbonate specimen shown in Figure 6.

In order for the deformation measured at the boundary of a specimen (or even locally using, e.g., an extensometer) to be representative, the deformation needs to be homogeneous within the gauge section. However, in the presence of inhomogeneous deformation phenomena, such as necking, barreling or strain localisation, it is evident that these conventional techniques of measuring the deformation are inadequate. Instead, full-field techniques, such as digital image correlation (DIC), must be used. Besides the benefit of being a full-field method, DIC also possesses the advantage of being a non-contact method, which reduces the influence of the measurement on the result. In DIC, pixel subsets in a reference image are correlated to subsets in images of the specimen taken throughout the loading history. By tracking the motion of these subsets, the displacement field and the corresponding strain field can be constructed at different states of deformation (e.g. Parsons et al. (2004); Viggiani and Hall (2008); Sutton et al. (2009); Poulain et al. (2013)). When using images from a single camera for DIC, a two dimensional deformation field can be reconstructed. By using two cameras calibrated for stereo-vision and so-called 3D-surface DIC or stereo correlation, it is possible to measure the out-of-plane deformation as well as the in-plane deformation. This technique involves stereo-correlation of pairs of images of the specimen surface taken simultaneously by the two cameras. A requirement for DIC is that the specimen has a random surface texture that is consistent during the deformation.

If the natural surface of the specimen is too homogeneous, as is the case for PC, a random speckle pattern can be applied to facilitate the correlation.

Full-field measurements enable deformation to be measured even if the experiment is performed under inhomogeneous conditions. Therefore, the material behaviour can be studied under more complex deformations compared to when using boundary measures. Also, even in what is often regarded as simple test, such as uni-axial tensile tests, inhomogeneous deformation phenomena, e.g. strain localisation or necking, are not uncommon. In this work, DIC has been used to capture the full deformation field to provide both correct local strain measurements and characterisation of heterogeneous responses, e.g., strain localisation. Due to the large amount of data acquired using DIC, it is also possible to identify larger sets of constitutive parameters from fewer tests, performed under multi-axial and/or inhomogeneous deformation, cf. Hild and Roux (2006); Avril et al. (2008).

Several techniques have been used to achieve multi-axial deformation. Ravi-Chandar and Ma (2000) achieved multi-axial, homogeneous compression of glassy polymers by using different confining cylinders. Hu et al. (2003) subjected tube-shaped specimens of epoxy to multi-axial deformation by combining internal pressure with axial and torsional loads. Another experimental technique to bring about multi-axial deformation is biaxial tension loading, e.g., Chevalier et al. (2001); Johlitz and Diebels (2011). As described in Section 3.2 and Paper D, this technique has been utilised within this work to study the mechanical behaviour of glassy PC during multi-axial deformation and to evaluate the model developed in Paper C,

While surface DIC is able to capture the deformation at the surface of a specimen, it is not possible to retrieve information on the deformation within the material using this technique. To gain knowledge of the internal structure of a material, techniques such as X-ray or neutron scattering can be used (e.g. Schubach and Heise (1986); Rössle et al. (1989); Toki et al. (2003)). In this work, X-ray scattering has been used to study the behaviour of the internal microstructure of glassy PC during deformation.

X-ray scattering is a technique used to examine the microstructure of a material by measuring the intensity of scattered X-rays at different angles due to the interaction of the incoming beam with the material. Scattering can, for example, be described in terms of Bragg's law,

$$\sin\theta = \frac{\lambda}{2d}, \tag{1}$$

where 2θ is the scattering angle, λ is the wavelength of the X-rays and d is the size of the repeating structure or, in crystallographic terms, the distance between crystallographic planes, see Figure 3. As the scattering angle is dependent on the wavelength of the incoming beam, it is sometimes more convenient to use q, defined as

$$q = \frac{4\pi}{\lambda}\sin\theta, \tag{2}$$

where q is related to the distance d as

$$q = \frac{2\pi}{d}. \tag{3}$$

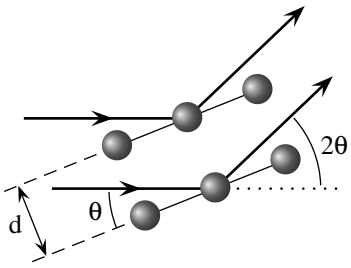

Figure 3: Incoming beams with the incident angle θ, relative to the two crystallographic planes with the separation d, and the scattering angle 2θ.

In practice, the minimum measurable q-value is governed by the quality of the collimation system whereas the maximum q-value is govern by the level of noise in the signal, cf. Schnablegger and Singh (2013). The measurable q-range can be altered by changing the wavelength or, equivalently, the energy of the X-rays or by changing the distance between the sample and the detector (changing the detectable scattering angles, 2θ); see Figure 4.

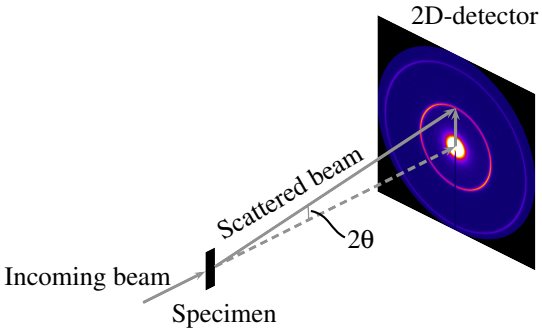

Figure 4: Principle sketch of the X-ray scattering showing the incoming and scattering beams, the scattering angle 2θ and the 2D scattering pattern.

The measured scattering intensity is an average value over all objects in the illuminated sample volume, as the whole sample cross section is investigated. As a consequence of this, details of e.g., shape, size or orientation will not be visible unless they are representative of the whole volume, cf. Schnablegger and Singh (2013). Furthermore, to be able to examine the microstructure using X-ray scattering there must be a difference of electron density between different parts of the microstructure in the same way that there must exist an optical contrast between different phases in order for microscopy to work.

It is common to make a distinction between small and wide angle X-ray scattering (SAXS/WAXS). When using WAXS, the maximum detectable scattering angle is, as the name suggests, larger than in SAXS. By studying larger angles, the size of the studied structures decreases, cf. Bragg's law (1). As indicated in Figure 5, WAXS is typically used to study the short-range order at the sub-nanometre scale, e.g., intramolecular distances or intermolecular packing, while SAXS can be used to examine structures with a size in

the order of 1 nm or larger, e.g. the size of crystallites in semi-crystalline polymers, cf. Roe (2000).

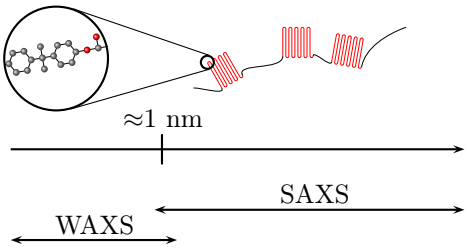

Figure 5: Schematic of the length-scales studied using WAXS and SAXS. WAXS is typically used to study the intramolecular distances while SAXS can be used to study structures with a size larger than 1 nm, e.g. the size of crystallites in semi-crystalline polymers.

SAXS has been used to examine the microstructure of semi-crystalline polymers such as polyethylene (e.g. Hubert et al. (2004); Humbert et al. (2009); Farge et al. (2013)). However, the work done using SAXS to study amorphous polymers, such as polycarbonate, is very limited. This is most likely a consequence of the assumed lack of long-range order in amorphous polymers and, thus, the information gained by SAXS is assumed to be limited. However, Lin and Kramer (1973) showed that the SAXS signal from PC is due to the structure of the material and not due to defects such as voids. To investigate the influence of deformation on the long-range order in the microstructure of amorphous PC, this work contains experiments where SAXS has been used in combination with *in-situ* loading, i.e. tensile loading while measuring the X-ray scattering. Although the cause is not yet fully investigated, the experimental results show a clear change of the SAXS signal due to the deformation. This is discussed in Paper A.

WAXS has been used to study the microstructure of semi-crystalline (e.g. Brown et al. (2008); Stoclet et al. (2012); Guo et al. (2015)) and amorphous polymers (e.g. Mitchell and Windle (1985); Schubach and Heise (1986); Stoclet et al. (2010)). Schubach and Heise (1986) used WAXS to study the short range order of in PC and they concluded that the peaks appearing in the WAXS data originated from intra- and intermolecular distances within the material. They also studied the orientation of the scattering on specimens that were stretched *ex-situ* just above the glass transition temperature.

In this thesis, WAXS measurements were performed to study the behaviour of the structure of glassy PC on a molecular scale during macroscopic deformation. The measurements show a clear reorientation of the chain network, a permanent change in the distance between neighbouring chains and an elastic response of the molecular segments. Furthermore, the experiments also revealed a fourth, not previously reported, WAXS peak within the studied q-range. Even though the origin of this peak is not fully determined, the behaviour of the scattering suggests that the peak is related to correlation between closely positioned entities along the polymer chain. A detailed discussion of the results are presented in Paper B.

3 Experimental method

During this work, experiments have been performed to characterise the mechanical response of glassy, amorphous PC. The experiments can be separated into two main categories: (1) X-ray scattering experiments with simultaneous *in-situ* uni-axial loading and DIC; (2) biaxial stretching with DIC. The X-ray scattering experiments were performed at the I911-SAXS beamline at the synchrotron facility MAX IV Laboratory (Lund University, Sweden) (Labrador et al. (2013)).

3.1 Material and specimens

The specimens used in the experiments were machined from sheets of transparent, commercial PC. No additional treatment of the material was performed, beside the machining. To obtain good quality scattering data, the choice of specimen thickness has to be balanced between the scattering intensity, which increases with thickness, and the absorption, which attenuates the beam with increasing thickness. The maximum intensity is found when the thickness, t, is

$$t = \frac{\cos\theta}{\mu(E)}, \tag{4}$$

where 2θ is the scattering angle and $\mu(E)$ is the energy dependent linear absorption coefficient, cf. Roe (2000). Having the absorption coefficient and the X-ray absorption, it is possible to estimate the current specimen thickness as

$$t = \frac{\ln(I_0/I_T)}{\mu(E)}, \tag{5}$$

where I_0/I_T is the absorption, I_0 is the incident beam intensity and I_T is the transmitted beam intensity. Using $\mu = 1.328$ cm^{-1} for PC at the energy $E = 13.6$ keV an optimal thickness of about 7.5 mm is found (μ is given by tabulated values, cf. The Center for X-Ray Optics (CXRO) at Lawrence Berkeley National Laboratory (2016)). Because of practical reasons related to the test device the specimen thickness was chosen as 5 mm instead of the optimal 7.5 mm. For the experiments with biaxial loading, a sheet thickness of 2 mm was chosen due to limitations in the grips of the test device.

Two geometries, one symmetrically notched and one asymmetrically notched, were used during the X-ray scattering experiments, see Figure 6. Both geometries were designed to focus the deformation into a small area of the specimen in order to have a well defined area where to measure the X-ray scattering. The asymmetrically notched geometry was chosen to promote shearing deformation between the notches. For the biaxial tension experiments, the asymmetrically notched geometry was extended to allow biaxial loading, see Figure 7.

3.2 Macroscopic loading

To investigate the mechanical response of amorphous PC, cold drawing experiments have been performed where the material was stretched uni-axially and biaxially using the custom

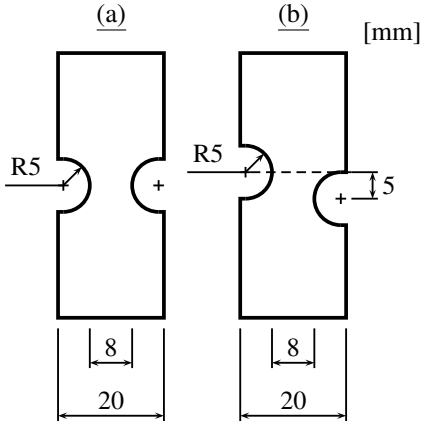

Figure 6: The geometry of the specimen for uni-axial deformation: (a) symmetrically notched; (b) asymmetrically notched.

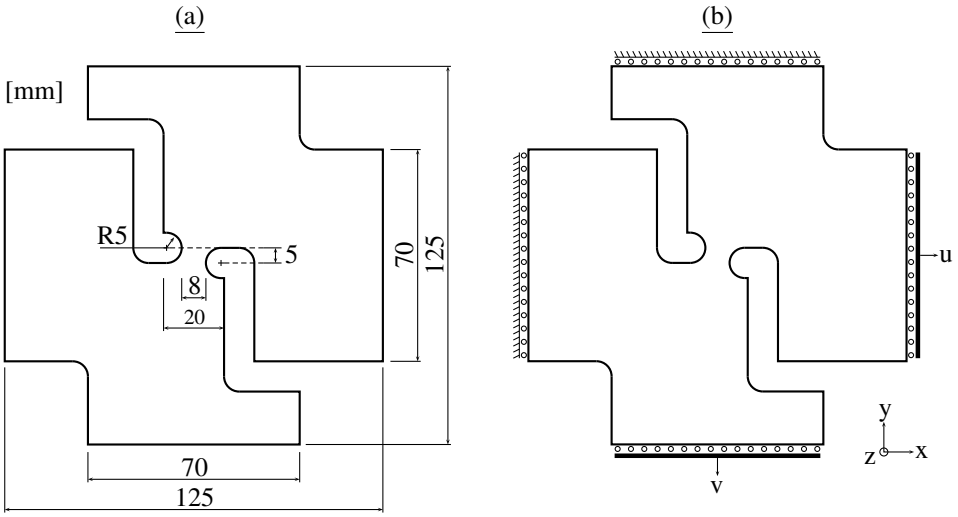

Figure 7: The dimensions of the specimen used in the biaxial deformation experiments (a) and the boundary conditions during loading and simulation (b).

built tensile test devices seen in Figure 8. The uni-axial tensile test machine was designed to fit into the I911-SAXS beamline at MAX IV Laboratory to be able to deform specimens *in-situ* while measuring the X-ray scattering. During the scattering experiments, the specimens were loaded using a constant displacement rate of 0.01 mm/min, measured on the moving machine grips. The low loading rate was chosen to be able to load continuously during the X-ray scattering measurements without any significant deformation of the specimen during each exposure (using an exposure time of 30 s). As discussed in Paper A, an alternative approach could have been to use intermittent loading with a higher displacement rate and keeping the deformation fixed during the X-ray measurements. However, while more time efficient, intermittent loading was found to lead to significant relaxation

of the material while keeping the deformation fixed. Moreover, when reloading the PC sample after relaxation beyond the macroscopic force peak, the force-displacement curve shows a new force peak, see Figure 9. This recurrent force peak and the relaxation makes it difficult to relate the force-displacement curve from a test with intermittent loading to a test with monotonic loading. It is also not obvious that the results from the X-ray measurements will be the same from a test with intermittent loading as the measurements will be made on a relaxed material instead of a material during loading.

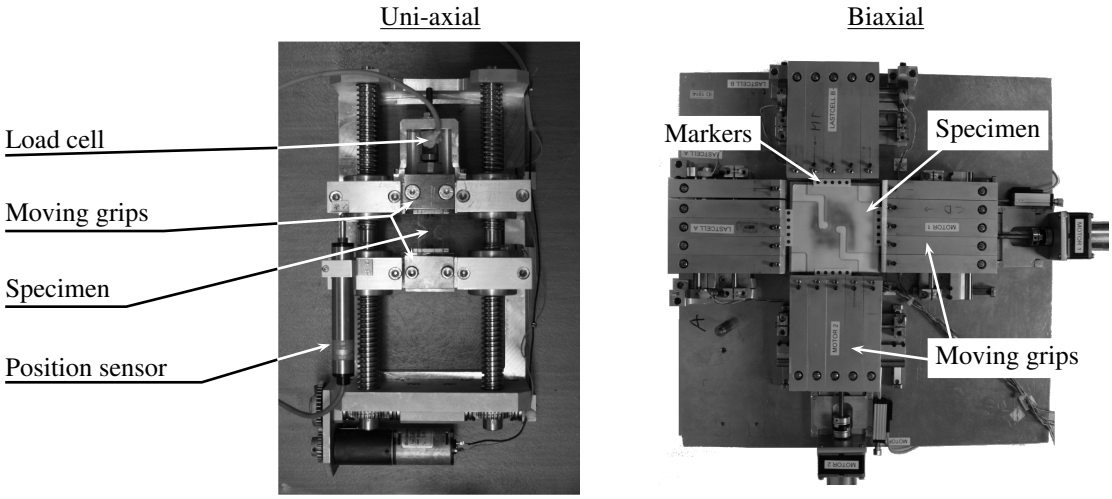

Figure 8: Custom built tensile test devices used in this thesis.

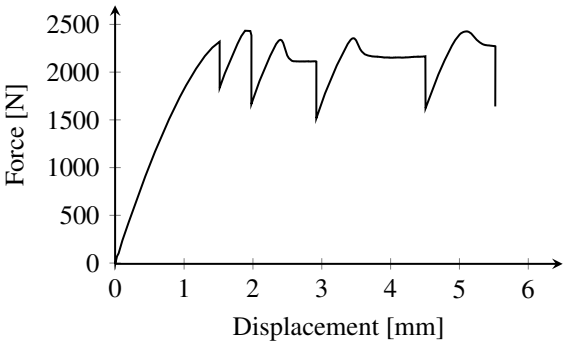

Figure 9: Force-displacement curve from a test with intermittent loading using a symmetrically notched specimen. The response clearly shows significant relaxation of the material when the deformation is fixed as well as the recurrent force peak on reload.

To study the strain localisation due to lateral deformation, biaxial loading was performed using a tensile test machine with two loading axis, arranged in a cruciform manner, see Figure 8. By controlling the motor of each of the two axes independently, the device allows for individual control of the loading along each axis. The four grips used to clamp the specimen are designed to move freely in the lateral direction, see Figure 7b. As the

biaxial test device is designed to allow lateral movement, in order not to subject the specimen to unwanted bending moments and to be able to use non-symmetrical specimens, the compliance of the grips is larger than when using fixed grips. To measure the displacements at the boundary of the specimen, without the compliance of the machine influencing the result, a camera system that follows the movement of markers placed on the specimen close to the grips was used, see Figure 8b. The camera system consisted of a 5 megapixel digital camera that acquired images with an approximate frame rate of 3 frames per second and an inhouse developed point-tracking code. The rate control of the machine used linear displacement sensors measuring the displacement of the two moving grips. These displacements were also recorded, along with the axial forces, during the experiments.

3.3 Mesoscopic deformation measurement using DIC

The DIC system used in this work involved two 29-Megapixel Prosilica GT6600 (Allied Vision) digital cameras, calibrated for stereo-vision. The image correlation, as well as the stereo-calibration, was made using the commercial software Vic-3D 7^{TM} (Correlated Solutions). When calibrating the system for stereo-vision, a series of images were acquired of a specifically designed calibration pattern in different positions and rotations, cf. Correlated Solutions (2010).

The displacement fields from the correlation software were used to calculate the displacement gradients using the closest neighbour subsets on a regular pixel grid, with an in-house developed code. These displacement gradients were, in turn, used to construct the strain fields. Since the deformation is measured at the surface of the specimen, it is necessary to approximate the out-of-plane displacement when calculating the displacement gradient. By assuming that the deformation is homogeneous through the thickness of the specimen, and by introducing a fixed Cartesian coordinate system, the deformation gradient can be written as

$$\boldsymbol{F}^{DIC} = \begin{bmatrix} 1+\frac{\partial u}{\partial X} & \frac{\partial u}{\partial Y} & 0 \\ \frac{\partial v}{\partial X} & 1+\frac{\partial v}{\partial Y} & 0 \\ \frac{\partial w}{\partial X} & \frac{\partial w}{\partial Y} & 1+\frac{2w}{T_0} \end{bmatrix}, \tag{6}$$

where u, v and w are the displacements in the x, y and z directions, measured by DIC at the surface and T_0 is the thickness of the undeformed specimen in the z-direction (out-of-plane direction).

To facilitate the DIC, a random speckle pattern was applied to the surface of the specimens using a water based paint, see Figure 10a. The water based paint was chosen to ensure that the paint did not react with, or damage, the polymer. For the SAXS/WAXS experiments, the area where the X-ray beam hit the specimen was left unpainted to ensure that the speckle pattern did not affect the result of the measurements. This resulted in a blank area in the deformation fields, see Figure 10b. The deformation in the blank area can however be approximated by interpolating the measured data around the blank area. This was done in order to get the current specimen thickness, which was used to

normalise the X-ray data in Paper A, B and C. When calculating the current thickness of the specimens from DIC, care was taken to remove rigid body motion. The thickness, calculated from DIC, showed good agreement with the specimen thickness calculated from the X-ray attenuation using (5).

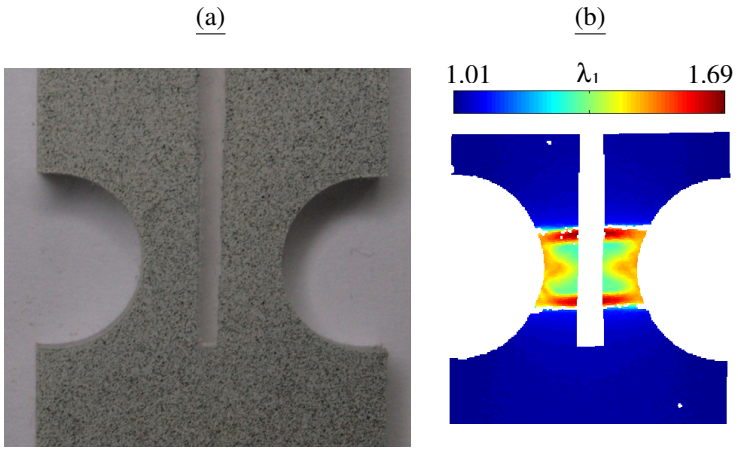

Figure 10: (a) Image showing a specimen for uni-axial deformation with a random speckle pattern applied. (b) A major principle stretch field from DIC. The blank area down the middle of the specimen is where the X-ray beam hit the specimen during the scattering experiments.

3.4 Microscopic deformation measured using X-ray scattering

To investigate the behaviour of the microstructure of glassy PC during deformation, small and wide angle X-ray scattering (SAXS/WAXS) experiments were performed. Due to the design of the beamline, the SAXS and WAXS measurements were performed at separate times using the set-ups shown in Figure 11. Scattering experiments were performed a total of five times, three times using SAXS and two times using WAXS. The SAXS experiments included an introductory experiment without *in-situ* DIC. Specimens of amorphous, glassy PC were deformed *in-situ* during the scattering measurements, as discussed in Section 3.2. Both monotonic and cyclic loading were performed during the experiments, using both geometries shown in Figure 6. At this time, only results from experiments with monotonic loading have been studied in detail. To be able to correlate the behaviour of the microstructure and the mesoscopic deformation, 3D-surface DIC was used to measure the deformation at the surface of the specimen *in-situ*, simultaneously as the scattering was measured. The three different systems used during the scattering experiments, the uni-axial loading system, the DIC system and the X-ray scattering were synchronised using a trigger signal from the X-ray detector.

Even though a distinction is made between SAXS and WAXS, the two techniques are very similar from the point of performing the measurements and the experimental set-up. The scattering data were recorded using a bi-directional hybrid pixel X-ray detector

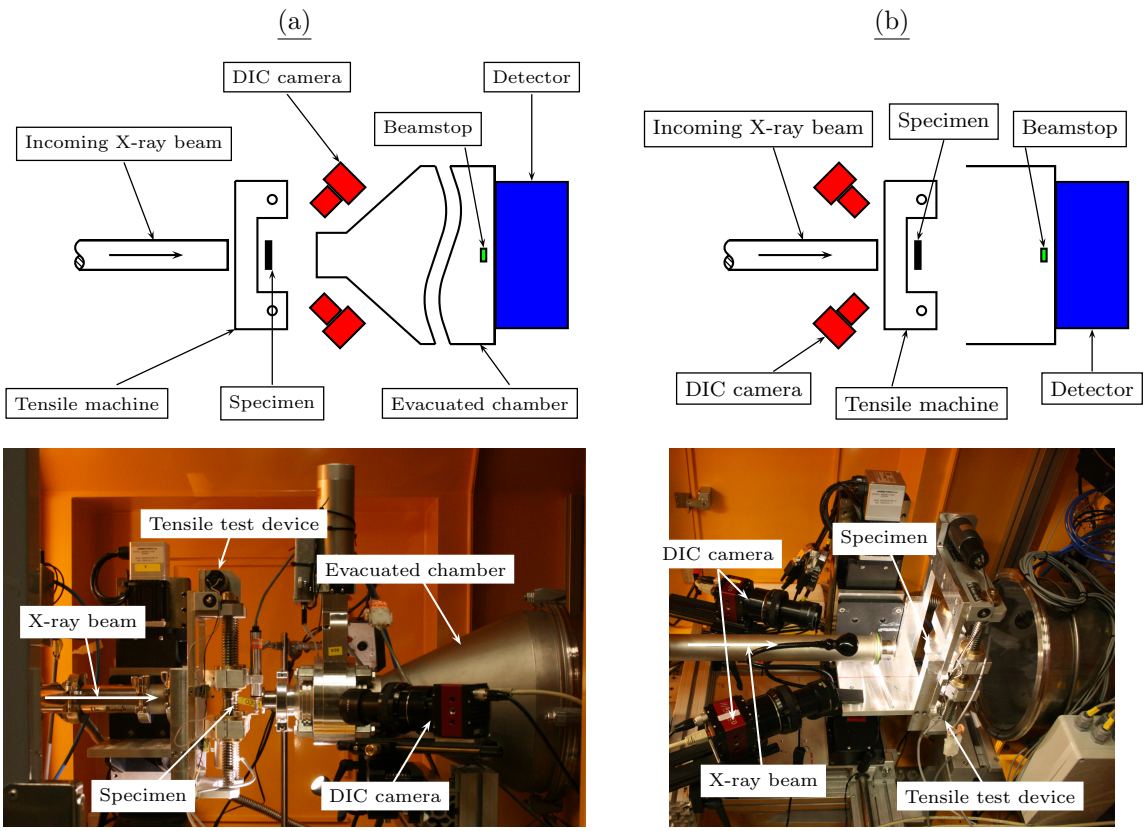

Figure 11: Experimental set-ups used during the X-ray scattering experiments. The figures on the left shows the SAXS set-up and on the right is the WAXS set-up. On top is a sketch of set-ups showing the X-ray beam path, the tensile test machine and the two DIC cameras (the sketch is not to scale). On the bottom are the actual set-ups inside the hutch of the beamline.

(Dectris Pilatus 1M). To get the scattering from the sample, the recorded data need to be corrected. The recorded scattering data were corrected by considering: (1) the transmission of the X-rays estimated from the intensity of the direct beam using a pin-diode detector placed on the beamstop; (2) the current specimen thickness at each spatial point, calculated from the out-of-plane deformation measurement from the DIC; (3) air scattering by subtraction the background scattering. Figure 12a shows a normalised two dimensional scattering pattern. From such scattering patterns, data profiles were extracted in two ways: (1) radially averaged azimuthal profiles or (2) radial profiles averaged over an angular sector, see Figure 12. The azimuthal profile ($I(\varphi)$ vs φ where φ is the azimuthal angle) can provide information on the orientation of the scattering at the length scale over which the averaging is made whereas radial profiles ($I(q)$ vs q) can provide details about the size and shape of the scattering entities.

In isotropic samples, the scattered intensity is constant around the azimuth. If, on the other hand, there exists a preferred orientation in the specimen at the studied length-scale,

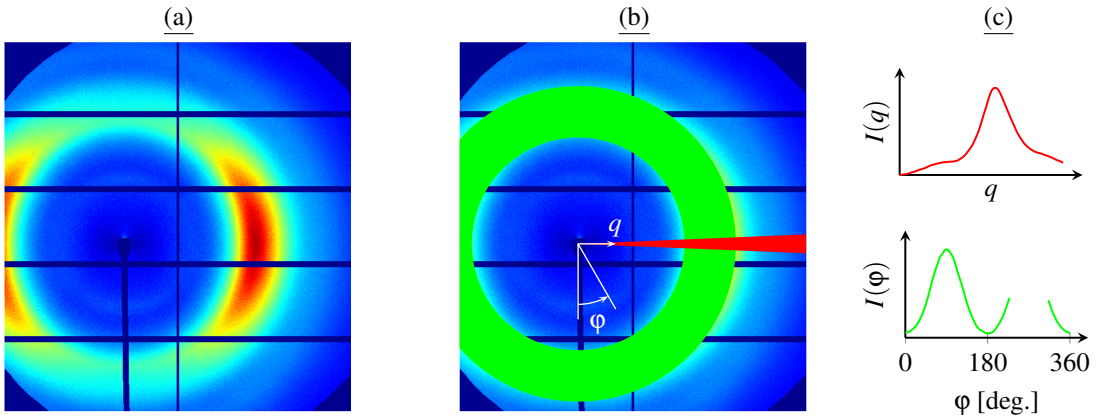

Figure 12: (a) X-ray scattering pattern as recorded by a 2D-detector. (c) Radial- (red) and azimuthal (green) profile averaged over the sectors indicated over the pattern in (b). The rectangular mesh in the scattering patterns is due to space between the modules of the Pilatus detector used to collect the scattering data. The gap in the azimuthal profile is due to the asymmetry of the pattern.

the intensity around the azimuth oscillates or shows peaks at certain angles, see Figure 12c. The degree of orientation can be described using different measures. One such measure is the Hermans orientation parameter, defined as

$$A^{nano} = \frac{3\left\langle \cos^2\varphi \right\rangle - 1}{2}, \tag{7}$$

where

$$\left\langle \cos^2\varphi \right\rangle = \frac{\int_0^\pi I(\varphi)\cos^2\varphi \sin\varphi \mathrm{d}\varphi}{\int_0^\pi I(\varphi)\sin\varphi \mathrm{d}\varphi}, \tag{8}$$

I is the intensity and φ is the azimuthal angle, cf. Roe (2000). The Hermans orientation parameter takes the value 0 for isotropy and 1 or -0.5 for full orientation parallel to the vertical and horizontal directions, respectively.

Depending on the scattering technique and prior knowledge of the scattering system, different approaches are available to analyse the radial profiles. If the radial profile shows peaks at certain q-values, the corresponding correlation distance can be determined by fitting probability density functions, e.g., Gaussian, to the data (see e.g. Stoclet et al. (2011); Guo et al. (2015)). An example of such a fitting is shown in Figure 13 where the sum of five Gaussian functions is fitted to experimental data. The resulting position of the peak(s) can then be used to determine the size of the objects through Bragg's law (1).

To investigate the spatial variation of the scattering, line scans were used to collect scattering data at points along the vertical centreline of the specimens. As discussed in Paper A and B, the spatial mapping revealed different behaviour of the scattering from points with different deformation history. This shows the importance of measuring at different points on the specimen. By mapping the spatial variation of the scattering while

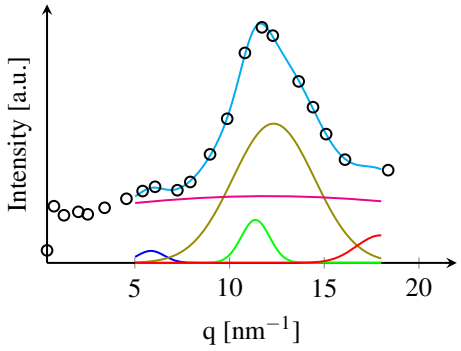

Figure 13: Analysis of a radial scattering profile by fitting the sum (cyan curve) of five Gaussian functions to the experimental data (open symbols).

deforming the specimen *in-situ*, a single experiment provides data from several points with different deformation histories as opposed to experiments were the scattering is measured at a single point. As discussed in Paper A, the spatial mapping can reveal unique characteristics in the scattering at other spatial locations than the centre points, which often is the most natural point to study when measuring at a single point.

By combining spatially resolved X-ray scattering with simultaneous 3D-surface DIC and *in-situ* loading, the local deformation, in terms of orientation and strain in the molecular structure, can be linked to local macroscopic measures of strain, while the specimen is deformed. This method provides a large amount of data from a single experiment and, by using the different techniques simultaneously, the coupling of the different measurements is more reliable, as the uncertainties related to combining data from different experiments are avoided.

4 Constitutive modelling of glassy polymers

A considerable work has been done over the years to improve the constitutive models used to predict the mechanical behaviour of glassy polymers. Boyce et al. (1988) proposed a 3-chain model to represent the polymer network using the non-Gaussian statistical model by Wang and Guth (1952). In the 3-chain model, the polymer network is represented by three chains, aligned along the sides of a cube. This approach is, however, unable to accurately distinguish between different states of deformation. To this end, Arruda and Boyce (Arruda and Boyce (1991, 1993)) proposed the 8-chain model which uses eight chains to represent the polymer network. In the 8-chain model, which better reproduces the mechanical response of glassy polymers, the chains extend along the diagonals from the centre to the corners of a unit cube. Another way of representing the underlying polymer network is to use a chain orientation distribution function (CODF) to distribute a large number of chains in space during the deformation. This approach was used by Wu and van der Giessen (1993) where they used the full-network model by Treloar and Riding (1979) to model the response of glassy PC under three dimensional loading. The approach

of using a CODF to distribute the chains was later used by Harrysson et al. (2010), who proposed a model capable of having a non-affine evolution of the microstructure.

The non-linear response at small strains before the macroscopic force peak, exhibited by many amorphous polymers, has been addressed in different fashions. Hasan and Boyce (1995) developed a one-dimension framework for the viscoplastic flow of glassy polymers based on evolving free volume. The flow theory by Hasan and Boyce, which uses a set of internal state variables to describe the evolution of the microstructure, predicts a smooth pre-peak behaviour. Anand and Gurtin (2003) used an approach with one internal variable related to the local free volume to predict the pre-peak behaviour. Chowdhury et al. (2008) proposed a split of the variable related to the strain softening in two parts. The split results in a smoother transition from elastic to viscoplastic response compared to the original model.

4.1 Kinematic framework for the continuum

Consider a body in the reference configuration $\Omega_0 \in \mathbb{R}^3$ at time t_0. The motion of this body from the reference configuration to the current configuration $\Omega \in \mathbb{R}^3$ at time $t > t_0$ is described by the non-linear mapping $\boldsymbol{\chi}(\boldsymbol{X}, t)$, where $\boldsymbol{X}$ denotes the position of a material particle in Ω_0 and the position of the same particle is $\boldsymbol{x} = \boldsymbol{\chi}(\boldsymbol{X}, t)$. The deformation of the body is described by the deformation gradient, $\boldsymbol{F} = \nabla_{\boldsymbol{x}} \boldsymbol{\chi}$ with $J = \det(\boldsymbol{F}) > 0$. Elasto-viscoplasticity is modelled by assuming that a multiplicative split of the deformation gradient can be used, i.e.,

$$\boldsymbol{F} = \boldsymbol{F}^e \boldsymbol{F}^{vp}, \tag{9}$$

where $\boldsymbol{F}^e$ defines the elastic deformation and $\boldsymbol{F}^{vp}$ the viscoplastic deformation. The multiplicative split (9) introduces a stress free intermediate configuration; see Figure 14. The elastic and viscoplastic deformation gradients can be split into a stretch part and a rotational part using polar decomposition, i.e.,

$$\boldsymbol{F}^e = \boldsymbol{V}^e \boldsymbol{R}^e \quad \text{and} \quad \boldsymbol{F}^{vp} = \boldsymbol{V}^{vp} \boldsymbol{R}^{vp}, \tag{10}$$

where $\boldsymbol{V}^e$ and $\boldsymbol{V}^{vp}$ are the symmetric, positive definite, left elastic and viscoplastic stretch tensors and $\boldsymbol{R}^e$ and $\boldsymbol{R}^{vp}$ are the orthogonal elastic and viscoplastic rotation tensors. Following Boyce et al. (1988), the elastic rotation tensor will be assumed to be equal to unity, i.e. $\boldsymbol{R}^e = \boldsymbol{1}$. This choice leads to a symmetric elastic deformation gradient, $\boldsymbol{F}^e = \boldsymbol{F}^{eT}$.

The evolution of the viscoplastic deformation is given by

$$\dot{\boldsymbol{F}^{vp}} = \boldsymbol{L}^{vp} \boldsymbol{F}^{vp}, \tag{11}$$

where a superposed dot denotes the material time derivative, $\boldsymbol{L}^{vp}$ is the material viscoplastic velocity gradient which can be additively decomposed as

$$\boldsymbol{L}^{vp} = \mathrm{sym}(\boldsymbol{L}^{vp}) + \mathrm{skew}(\boldsymbol{L}^{vp}) = \boldsymbol{D}^{vp} + \boldsymbol{W}^{vp}, \tag{12}$$

where $\boldsymbol{D}^{vp}$ is the symmetric viscoplastic rate of deformation tensor and $\boldsymbol{W}^{vp}$ is the skew-symmetric viscoplastic spin tensor.

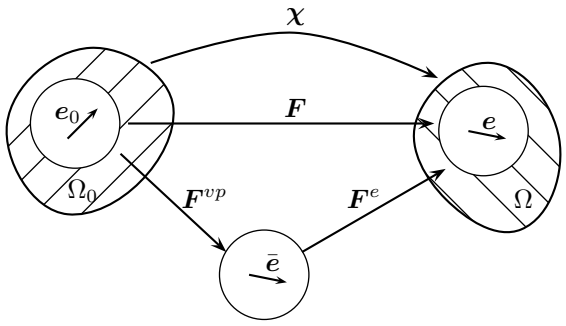

Figure 14: Illustration of the kinematic description of the continuum and the microstructure.

4.2 Kinematic framework for the microstructure

The results from the X-ray scattering experiments presented in Paper B show that the deformation of the microstructure differs from that measured on the macroscopic scale. Based on this observation, in Paper C it is assumed that the deformation of the microstructure can be described by a microstructural deformation gradient, denoted $\bar{\boldsymbol{F}}$. This approach has previously been used by Wallin et al. (2003) and Wallin and Ristinmaa (2005) to model the deformation of the crystal lattice in metal. Similar to (11), the evolution of the microstructural deformation is given by

$$\dot{\bar{\boldsymbol{F}}} = \bar{\boldsymbol{l}}\bar{\boldsymbol{F}}, \tag{13}$$

where $\bar{\boldsymbol{l}}$ is the microstructural velocity gradient. By splitting $\bar{\boldsymbol{l}}$ into a symmetric and a skew-symmetric part and following the discussion in Dafalias (2001), the microstructural velocity gradient is postulated as

$$\bar{\boldsymbol{l}} = \bar{\boldsymbol{d}} + \bar{\boldsymbol{w}} = \eta \boldsymbol{D}^p + \boldsymbol{W}^p, \tag{14}$$

where η is a parameter associated with the deformation of the microstructure. If $\eta = 1$, the microstructural deformation follows the macroscopic, viscoplastic deformation while $\eta \neq 1$ results in a microstructural deformation that differs from the macroscopic since $\bar{\boldsymbol{l}}$ will differ from $\boldsymbol{L}^{vp}$.

The model in Paper C also includes a permanent reorientation of the microstructure by introducing a set of unit vectors, $\bar{\boldsymbol{e}}$, describing the orientation of the microstructure. The director vectors, $\bar{\boldsymbol{e}}$, are obtained by mapping a set of vectors in the reference configuration, $\boldsymbol{e}_0$, to the intermediate configuration using $\bar{\boldsymbol{F}}$, i.e.,

$$\bar{\boldsymbol{e}} = \frac{\bar{\boldsymbol{F}}\boldsymbol{e}_0}{\|\bar{\boldsymbol{F}}\boldsymbol{e}_0\|}. \tag{15}$$

This reorientation of the microstructure is justified by the experimental results in Paper B, which clearly show a permanent reorientation of the molecule segments.

4.3 Thermodynamic framework

The thermodynamic framework can be used to derive constitutive relations. In this work, a hyperelastic format is used. The hyperelastic format implies the existence of a potential, i.e., the Helmholtz free energy ψ, which is a function of variables that characterise the system. These variables are defined as state variables, which must be chosen with some care since the choice will dictate which features of the system that will be modelled.

By fulfilling the dissipation inequality, it is ensured that a model obeys the second law of thermodynamics, which should be fulfilled for a physically sound model. Using isothermal conditions, the dissipation inequality can be formulated as

$$\mathcal{D} = \boldsymbol{\tau} : \boldsymbol{d} - \dot{\psi} \geq 0, \tag{16}$$

where ψ is the Helmholtz free energy per unit volume in the reference configuration, $\boldsymbol{\tau}$ is the Kirchhoff stress and $\boldsymbol{d}$ is the symmetric part of the spatial velocity gradient, $\boldsymbol{l} = \dot{\boldsymbol{F}}\boldsymbol{F}^{-1}$. In Paper C, the Helmholtz free energy is split into an elastic part, ψ^e and an inelastic part, ψ^{ie}, i.e.,

$$\psi(\boldsymbol{C}^e, \bar{\boldsymbol{C}}) = \psi^e(\boldsymbol{C}^e) + \psi^{ie}(\bar{\boldsymbol{C}}), \tag{17}$$

where $\boldsymbol{C}^e$ and $\bar{\boldsymbol{C}}$ are the elastic and microstructural right Cauchy-Green tensors respectively defined as

$$\boldsymbol{C}^e = \boldsymbol{F}^{eT}\boldsymbol{F}^e \quad \text{and} \quad \bar{\boldsymbol{C}} = \bar{\boldsymbol{F}}^T\bar{\boldsymbol{F}}, \tag{18}$$

which are used as state variables that characterise the deformation of the system.

4.4 Elasticity

The initial response of the material is assumed to be isotropic and any resulting anisotropy is assumed to be a consequence of permanent reorientation of the microstructure, thus elastic anisotropy is neglected. Furthermore, a decoupled volumetric-isochoric format of the elastic response is used, i.e.,

$$\psi^e = \psi^{e,vol} + \psi^{e,iso}. \tag{19}$$

Through the experiments in Paper D, it was found that the quadratic form of ψ^e commonly used to model the elastic response of glassy polymers, results in a too stiff initial response when the material is loaded in biaxial tension. To this end, a format of the volumetric part of the elastic free energy, that results in a softer response with increasing volumetric deformation, was chosen, i.e.,

$$\psi^{e,vol} = \frac{K_1}{2}(\ln J^e)^2 + K_2 \arctan(\beta(J^e - 1))(J^e - 1) - \frac{K_2}{2\beta}\ln\left((\beta(J^e - 1))^2 + 1\right), \tag{20}$$

where K_1, K_2 and β are model parameters and $J^e = \det(\boldsymbol{F}^e)$. To get the correct initial response, K_2 is defined as $K_2 = \frac{K - K_1}{\beta}$ where K is the initial bulk modulus. In addition to an improved initial stiffness, the proposed format of the elastic free energy also improves the behaviour around the macroscopic force peak, see Figure 15.

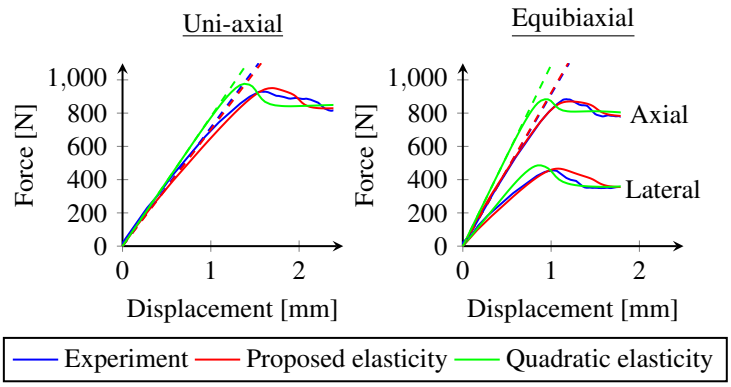

Figure 15: Comparison of the initial macroscopic response during biaxial loading from the experiment, the model using the proposed volumetric part of the elastic free energy in (20) and the model using a quadratic form of the elastic free energy. The dashed lines show the initial slope of the curves.

4.5 Viscoplasticity

The polymer network is modelled using the inelastic part of the Helmholtz free energy, ψ^{ie} in (17), from non-Gaussian statistical mechanics. Each chain in the network is modelled as an ideal free chain, assumed to consist of N rigid segments of equal length l, i.e., the total contour length, L, is $L = Nl$. The force, acting on the chain is related to the stretch of the chain, $\bar{\lambda} = \frac{r}{r_0}$, where r is the current end-to-end distance and r_0 is the end-to-end distance of the unstrained chain. Each free chain can be described by a random walk, neglecting any interactions between the segments, leading to $r_0 = \sqrt{N}l$. As the chain becomes fully extended, the end-to-end distance approaches the contour length, L, and the chain stretch approaches the limit stretch $\bar{\lambda} = \sqrt{N}$. The deformation of the chain network is taken as the orientation average of the stretch of the chains therein. By using the m-root average operator, the network stretch is calculated as

$$\lambda^{NW} = \sqrt[m]{\frac{1}{4\pi}\int_{\mathbb{U}^2}[\bar{\lambda}^m]\mathrm{d}A}, \tag{21}$$

where $m > 0$ and $\mathbb{U}^2$ is the unit sphere, cf. Miehe et al. (2004). An alternative kinematic variable is the relative stretch, λ_r, defined as

$$\lambda_r = \frac{\lambda^{NW}}{\sqrt{N}}, \tag{22}$$

approaching unity as the network is fully extended.

Since each chain is assumed to be ideal, thus rotations about the bonds are considered to be unrestricted, the internal energy of the chain is the same for all conformations and the Helmholtz free energy is determined by the entropy term. It is further assumed that

the entropy of the network is equal to the sum of the entropies of the individual chains, i.e., the inelastic free energy is

$$\psi^{ie} = n\psi^{chain}, \tag{23}$$

where n is the number of chains in the network. The free energy of one chain, ψ_{chain}, is, following e.g. Treloar (1975), taken as

$$\psi_{chain} = kN\theta \left(\lambda_r \mathcal{L}^{-1}(\lambda_r) + \ln \frac{\mathcal{L}^{-1}(\lambda_r)}{\sinh \mathcal{L}^{-1}(\lambda_r)} \right) - \psi_0, \tag{24}$$

where θ is the absolute temperature, k is the Boltzmann constant, ψ_0 is an arbitrary constant and $\mathcal{L}^{-1}$ is the inverse of the Langevin function.

5 Summary

Through the course of the work resulting in this thesis, an experimental method has been developed that combines X-ray scattering with simultaneous *in-situ* tensile loading and full-field deformation measurement using DIC. The developed method has been used to investigate the deformation of glassy PC over a wide range of length-scales. The experiments have resulted in novel observations on the correlation of the evolution of the molecular structure and the relevant local macroscopic measures of strain. Furthermore, biaxial tension experiments of glassy PC have been performed with 3D-surface DIC measurements. The experiments, in comparison with the model, revealed that the commonly used quadratic form of the elastic free energy results in a too stiff initial response as the material is deformed biaxially.

The motivation for performing the experiments has been based on the constitutive modelling of glassy polymers and the ambition of developing a model based on a sound experimental foundation. Based on the experimental results, a model that includes evolving directions of the idealised chain network and a microstructural deformation gradient has been developed. The model shows good agreement with the experimental data for the macroscopic force-displacement response, the local mesoscopic deformation in terms of strain fields and evolving orientation of the network. On the basis of this thesis it can be concluded that experiments performed using advanced experimental techniques, traditionally used by chemists and physicists, can provide important information when developing macroscopic constitutive models.

6 Future work

It is evident that much more work remains to be done to fully understand, and to fully be able to predict, the mechanical behaviour of glassy polycarbonate. To gain a more profound understanding of the link between micro- and macroscopic deformation, *in-situ* experiments combing multiple techniques such as X-ray or neutron scattering, full-field

deformation measurements and macroscopic deformation could be utilized to a greater extent.

In the presented work, the spatial variation of the scattering has been investigated by measuring at fixed spatial positions on the specimens. It would be desirable to instead follow the same material points during deformation. This, however, will require closed loop control where real time DIC controls the translation stage on the beamline, which positions the beam on the specimen.

The current work does not consider several important effects, such as temperature and strain rate dependence. By taking advantage of modern synchrotron facilities that allow for shorter exposure times, it will be possible to increase the loading rate without having to stop the loading while collecting the scattering data. Even without measuring the scattering, it would be of interest to include DIC to a greater extent when investigating the temperature and rate dependence.

The model parameters used in Paper C and Paper D (except the elastic parameters E and ν and the microscopic parameters η) have been found by fitting the model to macroscopic experimental data from uni-axial and plane strain compression tests with assumed homogeneous deformation. Since the assumption of homogeneous deformation may be questioned, a more appealing method of finding the parameters would be to minimize the deviation between deformation fields acquired using DIC and the model, cf. Hild and Roux (2006); Avril et al. (2008).

7 Summary of the papers

Paper A: In Paper A, an experimental method to simultaneously investigate the behaviour of (polymeric) materials over a wide range of length-scales by combining X-ray scattering with *in-situ* digital image correlation (DIC) and tensile loading is presented. The method is applied to experiments on specimens of amorphous, glassy polycarbonate. Using the presented method, the deformation is measured *in-situ*, simultaneously across different scales from the macroscopic deformation, measured using sensors on the tensile machine, to the full-field mesoscopic deformation, measured using DIC, down to the deformation of the nano-scale structure, studied using small and wide angle X-ray scattering (SAXS/WAXS). The evolution of the microstructure, with respect to both load level and spatial position, is given by measuring the X-ray scattering at several spatial points during continuous loading. By using spatial mapping of the scattering, characteristics in the scattering are observed that would not be seen when only measuring at the centre point of the specimen or when measuring on a large area of the specimen, e.g. wide beam SAXS/WAXS. The SAXS data show an orientation of the microstructure, in the SAXS region, follows the direction of the mesoscopic deformation, measured with DIC. Studying the intensities of radial profiles shows some elastic recovery in the SAXS data, while the scattering intensities remain unchanged after unload in WAXS. The azimuthal profiles from SAXS also show an elastic rebound of the orientation after unload. This indicates that the elastic recovery of the deformation after unload is due to reversible mechanisms in the SAXS range, while residual

deformation is mostly due to changes in the intermolecular structure of the material.

Paper B: In Paper B, the deformation of amorphous, glassy polycarbonate is characterised over a wide range of length-scales using tensile loading, DIC and WAXS with the method presented in Paper A. Novel observations of the evolution of the molecular structure, as the specimen deforms, linked to local macroscopic measures of deformation are shown. By measuring the scattering while deforming the specimen, a fourth, not previously reported WAXS peak is observed. Strains and evolving anisotropy are observed, and quantified, at different length scales identified from the WAXS measurements connected to inter- and intra-molecular structures. After unloading the specimen to zero macroscopic force, the inter-molecular structures show permanent deformations in the form of unrecoverable strains and reorientations. The intra-molecular structure, i.e. the chain segments, shows recoverable strains and unrecoverable reorientations after unload.

Paper C: A constitutive model for amorphous glassy polymers is developed in Paper C, motivated by the experimental results presented in Paper B. The model utilises a microstructural deformation gradient to incorporate the experimentally obtained deformation, and evolving orientation, of the microstructure. Using this approach, the model is able to accurately predict the deformation of glassy polycarbonate over a wide range of length-scales, from the macroscopic response down to the deformation of the microstructure. The proposed model is evaluated by comparing the numerical response to experimental results from an inhomogeneous cold drawing experiment of glassy polycarbonate, presented in Paper B. The simulated response is compared to experimental data of the macroscopic response, the mesoscopic deformation measured using DIC and the microscopic response measured using X-ray scattering. The model shows good agreement with the experimental data throughout the studied length scales.

Paper D: In Paper D, the mechanical behaviour of glassy polycarbonate is studied during biaxial tension loading. The biaxial loading is found to have a significant influence on the localisation behaviour, captured using DIC. By comparing the constitutive model developed in Paper C to the experimental data, it is found that the commonly used quadratic form of the elastic free energy results in a too stiff initial response during biaxial loading. To this end, a new format for the volumetric part of the elastic free energy, which results in a softer response with increasing volumetric deformation, is proposed. The proposed elastic free energy also improves the ability to accurately capture the non-linear, pre-peak behaviour exhibited by glassy PC.

References

Ames, N. M., Srivastava, V., Chester, S. A., Anand, L., 2009. A thermo-mechanically coupled theory for large deformations of amorphous polymers. Part II: Applications. International Journal of Plasticity 25 (8), 1495–1539.

Anand, L., Gurtin, M. E., 2003. A theory of amorphous solids undergoing large deforma-

tions, with application to polymeric glasses. International Journal of Solids and Structures 40 (6), 1465–1487.

Arruda, E. M., Boyce, M. C., 1991. Evolution of plastic anisotropy in amorphous polymers during finite straining. In: Boehler, J.-P., Khan, A. S. (Eds.), Anisotropy and Localization of Plastic Deformation. Elsevier Applied Science, London, pp. 483–488.

Arruda, E. M., Boyce, M. C., 1993. A three-dimensional constitutive model for the large stretch behavior of rubber elastic materials. Journal of the Mechanics and Physics of Solids 41 (2), 389–412.

Arruda, E. M., Boyce, M. C., Jayachandran, R., 1995. Effects of strain rate, temperature and thermomechanical coupling on the finite strain deformation of glassy polymers. Mechanics of Materials 19 (2), 193–212.

Avril, S., Bonnet, M., Bretelle, A.-S., Grediac, M., Hild, F., Ienny, P., Latourte, F., Lemosse, D., Pagano, S., Pagnacco, E., et al., 2008. Overview of identification methods of mechanical parameters based on full-field measurements. Experimental Mechanics 48 (4), 381–402.

Boyce, M. C., Parks, D. M., Argon, A. S., 1988. Large inelastic deformation of glassy polymers. Part I: rate dependent constitutive model. Mechanics of Materials 7 (1), 15–33.

Brown, E. N., Rae, P. J., Dattelbaum, D. M., Clausen, B., Brown, D. W., 2008. In-situ measurement of crystalline lattice strains in polytetrafluoroethylene. Experimental Mechanics 48 (1), 119–131.

Chevalier, L., Calloch, S., Hild, F., Marco, Y., 2001. Digital image correlation used to analyze the multiaxial behavior of rubber-like materials. European Journal of Mechanics - A/Solids 20 (2), 169–187.

Chowdhury, K., Talreja, R., Benzerga, A. A., 2008. Effects of manufacturing-induced voids on local failure in polymer-based composites. Journal of Engineering Materials and Technology 130 (2), 021010.

Correlated Solutions, 2010. Vic-3D Testing Guide. Correlated Solutions.

Cowie, J. M. G., Arrighi, V., 2007. Polymers: chemistry and physics of modern materials. CRC press.

Dafalias, Y. F., 2001. Orientation distribution function in non-affine rotations. Journal of the Mechanics and Physics of Solids 49 (11), 2493–2516.

Dreistadt, C., Bonnet, A.-S., Chevrier, P., Lipinski, P., 2009. Experimental study of the polycarbonate behaviour during complex loadings and comparison with the Boyce, Parks and Argon model predictions. Materials & Design 30 (8), 3126–3140.

Farge, L., André, S., Meneau, F., Dillet, J., Cunat, C., 2013. A common multiscale feature of the deformation mechanisms of a semicrystalline polymer. Macromolecules 46 (24), 9659–9668.

G'sell, C., Jonas, J., 1979. Determination of the plastic behaviour of solid polymers at constant true strain rate. Journal of Materials Science 14 (3), 583–591.

Guo, H., Wang, J., Zhou, C., Zhang, W., Wang, Z., Xu, B., Li, J., Shang, Y., de Claville Christiansen, J., Yu, D., et al., 2015. Direct investigations of deformation and yield induced structure transitions in polyamide 6 below glass transition temperature with waxs and saxs. Polymer.

Harrysson, M., Ristinmaa, M., Wallin, M., Menzel, A., 2010. Framework for deformation induced anisotropy in glassy polymers. Acta Mechanica 211 (3-4), 195–213.

Hasan, O., Boyce, M., 1995. A constitutive model for the nonlinear viscoelastic viscoplastic behavior of glassy polymers. Polymer Engineering & Science 35 (4), 331–344.

Hild, F., Roux, S., 2006. Digital image correlation: from displacement measurement to identification of elastic properties–a review. Strain 42 (2), 69–80.

Hu, Y., Xia, Z., Ellyin, F., 2003. Deformation behavior of an epoxy resin subject to multiaxial loadings. part i: Experimental investigations. Polymer Engineering & Science 43 (3), 721–733.

Hubert, L., David, L., Seguela, R., Vigier, G., 2004. Small-angle x-ray scattering investigation of the deformation processes in the amorphous phase of high density polyethylene. Polymer International 53 (5), 582–585.

Humbert, S., Lame, O., Vigier, G., 2009. Polyethylene yielding behaviour: What is behind the correlation between yield stress and crystallinity? Polymer 50 (15), 3755–3761.

Johlitz, M., Diebels, S., 2011. Characterisation of a polymer using biaxial tension tests. part i: Hyperelasticity. Archive of Applied Mechanics 81 (10), 1333–1349.

Labrador, A., Cerenius, Y., Svensson, C., Theodor, K., Plivelic, T., 2013. The yellow minihutch for saxs experiments at max iv laboratory. In: Journal of Physics: Conference Series. Vol. 425. IOP Publishing, p. 072019.

Lin, W., Kramer, E. J., 1973. Small-angle x-ray scattering from amorphous polycarbonate. Journal of Applied Physics 44 (10), 4288–4292.

Miehe, C., Göktepe, S., Lulei, F., 2004. A micro-macro approach to rubber-like materials – Part I: the non-affine micro-sphere model of rubber elasticity. Journal of the Mechanics and Physics of Solids 52 (11), 2617–2660.

Mitchell, G. R., Windle, A. H., 1985. The effect of annealing on the local structure of glassy polycarbonate. Colloid and Polymer Science 263 (4), 280–285.

Parsons, E., Boyce, M., Parks, D., 2004. An experimental investigation of the large-strain tensile behavior of neat and rubber-toughened polycarbonate. Polymer 45 (8), 2665–2684.

Poulain, X., Kohlman, L., Binienda, W., Roberts, G., Goldberg, R., Benzerga, A., 2013. Determination of the intrinsic behavior of polymers using digital image correlation combined with video-monitored testing. International Journal of Solids and Structures 50 (11), 1869–1878.

Ravi-Chandar, K., Ma, Z., 2000. Inelastic deformation in polymers under multiaxial compression. Mechanics of Time-Dependent Materials 4 (4), 333–357.

Roe, R. J., 2000. Methods of X-ray and neutron scattering in polymer science. Vol. 739. Oxford University Press New York.

Rössle, W., Lindner, P., Dettenmaier, M., 1989. Deformation of glassy polycarbonate studied by neutron scattering. Physica B: Condensed Matter 156, 414–416.

Schnablegger, H., Singh, Y., 2013. The saxs guide: getting acquainted with the principles. Anton Paar GmbH 2.

Schubach, H. R., Heise, B., 1986. Structure and anisotropy in polycarbonate. i. short range order of amorphous polycarbonate revealed by waxs. Colloid and Polymer Science 264 (4), 335–342.

Stoclet, G., Seguela, R., Lefebvre, J., Li, S., Vert, M., 2011. Thermal and strain-induced chain ordering in lactic acid stereocopolymers: influence of the composition in stereomers. Macromolecules 44 (12), 4961–4969.

Stoclet, G., Seguela, R., Lefebvre, J.-M., Rochas, C., 2010. New insights on the strain-induced mesophase of poly (d, l-lactide): in situ waxs and dsc study of the thermomechanical stability. Macromolecules 43 (17), 7228–7237.

Stoclet, G., Seguela, R., Vanmansart, C., Rochas, C., Lefebvre, J.-M., 2012. Waxs study of the structural reorganization of semi-crystalline polylactide under tensile drawing. Polymer 53 (2), 519–528.

Sutton, M. A., Orteu, J.-J., Schreier, H. W., 2009. Image correlation for shape, motion and deformation measurements: basic concepts, theory and applications. Springer.

The Center for X-Ray Optics (CXRO) at Lawrence Berkeley National Laboratory, April 2016. Cxro x-ray interactions with matter.
URL `http://henke.lbl.gov/optical_constants/`

Toki, S., Sics, I., Ran, S., Liu, L., Hsiao, B. S., 2003. Molecular orientation and structural development in vulcanized polyisoprene rubbers during uniaxial deformation by in situ synchrotron x-ray diffraction. Polymer 44 (19), 6003–6011.

Treloar, L., 1944. Stress-strain data for vulcanised rubber under various types of deformation. Transactions of the Faraday Society 40, 59–70.

Treloar, L., Riding, G., 1979. A non-Gaussian theory for rubber in biaxial strain. I. Mechanical properties. In: Proceedings of the Royal Society of London A: Mathematical, Physical and Engineering Sciences. Vol. 369. The Royal Society, pp. 261–280.

Treloar, L. R. G., 1975. The physics of rubber elasticity. Oxford University Press, USA.

Viggiani, G., Hall, S. A., 2008. Full-field measurements, a new tool for laboratory experimental geomechanics. In: Proceedings of the 4th International Symposium on Deformation Characteristics of Geomaterials (Burns SE, Mayne PW and Santamarina JC (Eds.)). pp. 3–26.

Wallin, M., Ristinmaa, M., 2005. Deformation gradient based kinematic hardening model. International Journal of Plasticity 21 (10), 2025–2050.

Wallin, M., Ristinmaa, M., Ottosen, N. S., 2003. Kinematic hardening in large strain plasticity. European Journal of Mechanics-A/Solids 22 (3), 341–356.

Wang, M. C., Guth, E., 1952. Statistical theory of networks of non-gaussian flexible chains. The Journal of Chemical Physics 20, 1144.

Wu, P., van der Giessen, E., 1993. On improved network models for rubber elasticity and their applications to orientation hardening in glassy polymers. Journal of the Mechanics and Physics of Solids 41 (3), 427–456.

Paper A

Jonas Engqvist, Stephen A. Hall, Mathias Wallin,
Matti Ristinmaa and Tomás S. Plivelic

Multi-scale measurement of (amorphous) polymer deformation: Simultaneous X-ray scattering, digital image correlation and in-situ loading

Experimental Mechanics 55 (2014), 1373-1383

Multi-scale measurement of (amorphous) polymer deformation: Simultaneous X-ray scattering, digital image correlation and *in-situ* loading.

Jonas Engqvist[a], Stephen A. Hall[a,b], Mathias Wallin[a], Matti Ristinmaa[a] and Tomás S. Plivelic[c]

[a]Division of Solid Mechanics Lund University, Box 118, S-221 00 Lund, Sweden

[b]European Spallation Source AB, P.O. Box 176, 221 00, Lund, Sweden

[c]MAX IV Laboratory, Lund University, P.O. Box 118, 221 00, Lund, Sweden

Abstract

This paper presents a method to investigate the behaviour of polymers on different scales during deformation using simultaneously collected synchrotron X-ray scattering, digital image correlation (DIC) and tensile loading. The method is demonstrated through experiments made on specimens of amorphous polycarbonate. Deformation is measured *in-situ*, simultaneously across different scales from the macroscopic deformation, measured using sensors on the tensile machine, to the full-field mesoscopic deformation, measured using DIC, down to the deformation of the nano-scale structure, studied using small and wide angle X-ray scattering (SAXS/WAXS). The DIC reveals highly inhomogeneous deformations that render conventional techniques for measuring deformation, such as extensiometers, virtually useless. The X-ray scattering is measured in several spatial points during continuous loading giving the evolution of the microstructure with respect to both spatial location and load level. The spatial mapping of the scattering reveals characters that would not be observed when only measuring at the centre point or measuring on a large area of the specimen, e.g. wide beam SAXS/WAXS or small angle neutron scattering (SANS). With these data, the macroscopic and the mesoscopic deformation can be correlated to the behaviour of the microstructure providing relevant information when developing micro-mechanical based constitutive models. The experimental results shown here indicate a direct correlation between the major principal strain direction and the maximum anisotropy direction of the SAXS patterns. The current approach can be extended to any kind of polymeric materials or polymer-based nano-composites.

1 Introduction

For many polymers inhomogeneous deformation phenomena, such as necking and strain localisation, occur at relatively small strains (e.g. Lu and Ravi-Chandar (1999)). These phenomena have been seen to involve micro- and nano-scale rearrangement of the polymer material (e.g. Humbert et al. (2009); Choi et al. (2012)). Accurate material models should describe these different scale-length mechanisms. However, whilst a number of models have been proposed that include the evolution of the polymer arrangement and might be able to capture the inhomogeneous deformation (e.g. Wu and van der Giessen (1993); Miehe et al. (2009); Harrysson et al. (2010)), the experimental support and understanding to describe the micro-structural mechanisms is limited. This limited understanding arises largely due to the heterogeneous nature of the deformation and the need to capture a variety of mechanisms occurring over a wide range of length-scales.

Nuclear magnetic resonance (NMR), small and wide angle X-ray scattering (SAXS/ WAXS) and small angle neutron scattering (SANS) have been used previously to investigated the evolution of nano- and micro-structural order in polymers during, or resulting from, deformation (e.g. Vogt et al. (1990); Hubert et al. (2004); Schubach and Heise (1986); Rössle et al. (1989)), but in general taken as an average over a large area of the specimen. Furthermore, in such experiments, the stresses and strains of the material are only measured globally. Such measurements can not be regarded as representative of the material behaviour in the presence of the observed, significant heterogeneity of the processes. In this work we present an approach to monitor the heterogeneity of the different processes across the different scales using three experimental techniques simultaneously: (i) spatially resolved X-ray scattering (SAXS and WAXS) to investigate polymer ordering at the nano- and micro-scales associated with (ii) concurrent mechanical loading (with measurement of the global stress-strain response) and (iii) simultaneous measurement of mesoscopic strain fields by digital image correlation (DIC). An overview of the different methods for experimental characterisation and theoretical modelling of polymer deformation is first presented. This is followed by a description of the experimental set-up. The approach is demonstrated with an example involving application to an amorphous glassy polymer (polycarbonate) using SAXS and WAXS with *in-situ* loading and DIC. The example is followed by a discussion of the results, conclusions and perspectives for future work.

2 Experimental observations and modelling of deformation mechanisms in polymers at different scales

Methods for measuring the heterogeneous deformation of polymeric materials at large strains have been developed during the last four decades. For example, G'sell and Jonas (1979) developed a method of conducting tensile tests at constant local strain rate using hourglass shaped specimen and a circumference gauge to control the tensile machine. This

allowed true stress vs true strain curves to be measured at constant local strain rate. In Buisson and Ravi-Chandar (1990) the true stress vs stretch variation along the necking zone of polycarbonate (PC) specimen was estimated using a fine mesh applied on the surface of specimen, with square cross section, that was photographed during loading. The displacements were calculated from the images, which in turn were used to calculate the displacement gradient by a polynomial fit. Assuming the same stretch along the two lateral directions, due to square cross section area, they were able to study variation of the stretch along the necking zone. They measured the true stress using photoelasticity. A similar, more automated, method where a grid was screen printed on the surface of a specimen was used by Haynes and Coates (1996).

Full-field methods, such as the grid based methods above, have been shown to have an advantage in that they provide insight into the heterogeneity of the deformation. Digital image correlation (DIC) has become a more standard full-field technique for displacement and strain field measurement. Using DIC, the displacement field is constructed by correlating pixel subsets in a reference image of the undeformed specimen to subsets in the image of the specimen in the deformed state. The correlation requires a random surface texture, if the natural surface is too homogeneous a random speckle pattern can be applied to enable the correlation. The displacement data can be used to construct the displacement gradients which in turn can be used to calculate the full strain field (e.g. Viggiani and Hall (2008); Sutton et al. (2009)). Parsons et al. (2004) used 2D-surface DIC with a single charge coupled device (CCD) camera to measure the in-plane deformation field of rectangular bar-type PC specimen with different compositions. True stress-strain curves and full-field strain plots were constructed from the displacement data. To obtain 3D information two consecutive tests, measuring the 2D displacement fields in the two lateral directions were made. Data from these tests where combined to calculate the volumetric strain. A continuation of these experiments was made by Parsons et al. (2005) where the two lateral directions were depicted simultaneously using a right-angle prism avoiding uncertainties arising when combining data from separate tests. Daiyan et al. (2012) used 3D-surface DIC with two cameras calibrated for stereo-vision to investigate the modes of deformation during shear tests of polypropylene (PP). They concluded that DIC is an important tool that can provide the strain distribution and the ability to observe how the strain state of every point on the specimen changes during shearing. David et al. (2013) investigated the mechanical properties of poly-methyl-methacrylate (PMMA) during uniaxial tension using 2D-surface DIC. The PMMA was reinforced with carbon nanotubes (CNT) to different degree. Using DIC they studied the behaviour of Young's modulus, Poisson's ratio, the ultimate tensile stress and the failure strain at different CNT concentrations. Poulain et al. (2013) used cylindrical specimens of epoxy resin loaded in tension and compression, and measured the strains using 3D-surface DIC and two types of video-based extensometry: video-based surface extensometry (VSE) and video-based radial extensometry (VRE). It was shown that VRE is a simple method to get a very good estimate of the true stress-strain behaviour of the polymer. However, compared to DIC, VSE based on vertical markers is less reliable when the specimen experiences structural instabilities such as necking in tension and barreling in compression.

DIC can provide the full-field deformation of a specimen, but techniques such as X-ray or neutron scattering must be used to gain information on the microstructure within the material. Previously X-ray methods such as small and wide angle X-ray scattering (SAXS/WAXS) have been used to study the microstructure on a nanometre scale of both amorphous and semi-crystalline polymers. For example, the small angle X-ray scattering of PC was investigated by Lin and Kramer (1973). By doping PC specimens with small amounts of iodine and observing a decrease in the scattered intensity, they concluded that the SAXS signal was due to the structure of the material and not due to defects, such as voids. To obtain the microscopic strain, Hubert et al. (2004) measured the interlamellar spacing in two types of high density polyethylene (HDPE) with SAXS, at the centre point of 1 mm thick hourglass shaped specimen while deforming the specimens *in-situ*. The interlamellar spacing was used to calculate the microscopic strains parallel and perpendicular to the loading. These microscopic strains were compared to the macroscopic local strains measured *ex-situ* using video extensometry on a different specimen. They concluded that SAXS with *in-situ* loading could be used to asses the intercrystalline tie chain density of the materials as an alternative to conventional methods. Further in Humbert et al. (2010) the deformation of the microstructure of PE with different degrees of crystallinity was measured. The microscopic strain was measured using SAXS with *in-situ* loading and compared with the macroscopic strain measured using an optical extensometer. The SAXS was measured in the centre point of dumbbell-shaped specimens with a thickness of 500 µm. They concluded that the ratio between the microscopic and macroscopic strain was nearly constant for different degrees of crystallinity. Using WAXS, Schubach and Heise (1986) studied the short range order of the microstructure in PC. They concluded that the scattering signals originated from the intra- and intermolecular length scales within the material. The orientation of the scattering was studied on a stretched specimen that was deformed *ex-situ* above the glass transition temperature. Toki et al. (2003) studied the moleculare orientation and strain-induced crystallisation of rubber using WAXS with *in-situ* uniaxial loading. The WAXS was measured at the same spatial location on the specimen during deformation at a relatively large deformation rate of 10 mm/min with a typical acquisition time of 30 s. They concluded that the main part of the polymer chains remained unoriented even at large strains and that only about 20% of the molecules crystallised. The strain-induced crystallised molecules were highly oriented along the deformation direction. The chain orientation and the amorphous-crystalline microstructure of polyurea (PU) under uniaxial tension has been studied by Choi et al. (2012) using SAXS and WAXS. The specimens used were stretched *ex-situ* and clamped to remain stretched during the X-ray measurements. They showed that the microstructure, and thus the mechanical response, of PU varied continuously with deformation even at a very low deformation rate. They concluded that this contradicts a common assumption when modelling elastomers that strain and strain rate effects are separable, at sufficiently low strain rate, cf. Choi et al. (2012). In the recent work by Farge et al. (2013) the anisotropy of semi-crystalline HDPE was analysed on multiple scales during deformation using data from SAXS, incoherent steady light transport (ISLT), synchrotron radiation X-ray tomographic microscopy (SRXTM) or DIC. During SAXS, ISLT and DIC measurements the specimens were loaded *in-situ* while

the SRXTM were made postmortem. The measurements were made at the centre point of different specimens. It was concluded that the evolution of the anisotropy observed at the micro scales is strongly correlated with the macroscopic behaviour.

In constitutive modelling of polymeric materials different approaches have been used to incorporate the microstructure. Amorphous polymers such as polycarbonate have been modelled using idealised network models to represent the chain structure. These network models include the "3-chain" model by Wang and Guth (1952), the "8-chain" model by Arruda and Boyce (1993) and the full-network model by Wu and van der Giessen (1993). The full-network model considers a large number of polymer chains and averages over all orientations using a chain orientation distribution function (CODF). The CODF has been further utilised by Harren (1995), Harrysson et al. (2010) among others. Miehe et al. (2004) proposed a micro-sphere model with a non-affine coupling of the micro-structural chain network and the macroscopic response. The model makes use of a micro-sphere approach to represent the full chain network using 21 orientations in space.

A key objective of the current work is to use simultaneous X-ray scattering with *in-situ* loading and DIC to provide the experimental data necessary to support micromechanically based models such as those described above. The aim is thus to develop a method that can provide a correct understanding of the relationship of the macro- and meso-scopic deformation with the evolution of the microstructure.

3 Experiments

The experiments in this study were performed at the I911-SAXS beamline at MAX IV Laboratory (Lund University, Lund, Sweden), cf. Labrador et al. (2013). The experiments involved uniaxially loading of specimens *in-situ* during SAXS or WAXS measurements. The deformation of the specimen was measured using 3D-surface DIC. The experimental set-up mounted on the beamline consist of the tensile test machine and two digital cameras for 3D-surface DIC, see Figure 1. The experiments were conducted at room temperature.

3.1 Material and specimens

The specimens used in this study were made of Makroclear®, a transparent, amorphous commercial PC manufactured by Arla Plast. The material was delivered in a sheet of 5 mm thickness. Asymmetrically notched specimen with a vertical offset between the notches were machined from the sheet, see Figure 2. A geometry with offset notches was chosen to promote a shearing mode of deformation.

3.2 *In-situ* loading

The loading device used was a custom built uniaxial tensile test machine, see Figure 3. During the experiment the axial force and displacement of the grips were measured by a force transducer and a linear displacement sensor, respectively. The loading rate was

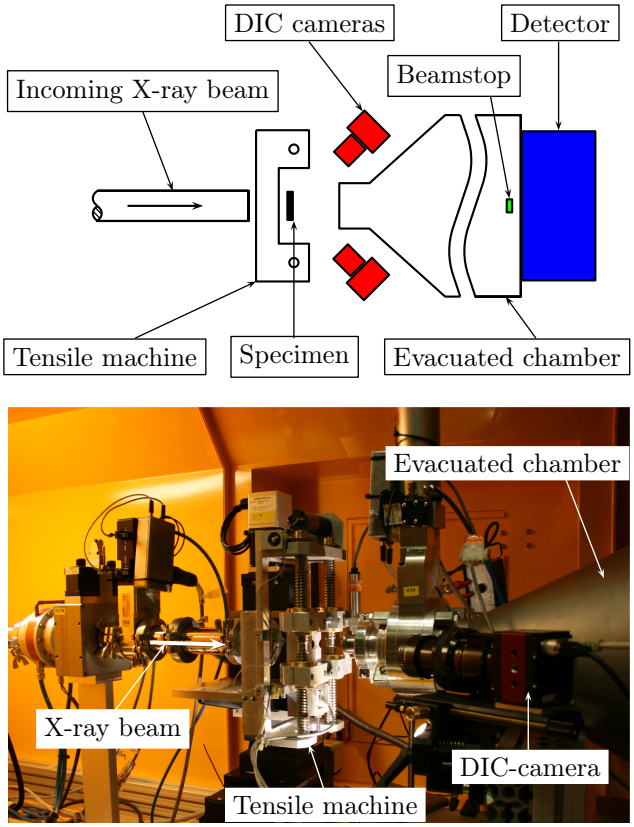

Figure 1: Experimental set-up. On top is a sketch of the set-up showing the X-ray beam path, the tensile machine and both DIC-cameras (not to scale). During the WAXS experiments the DIC-cameras were mounted on the left side of the tensile test machine (the same side as the incoming X-ray beam). On the bottom is the actual set-up for SAXS experiments inside the hutch of the beamline.

0.01 mm/min, measured on the machine grips, which were displaced symmetrically around the centre of the specimen. This slow loading rate was chosen to allow continuous loading during the X-ray measurements and thus avoid relaxation of the material.

3.3 X-ray scattering

SAXS measurements were carried out using a wavelength, λ, of 0.91 Å and a sample-to-detector distance of about 1.94 m giving an approximate q-range from 0.08 to 4 nm^{-1} (where $q = (4\pi/\lambda)\sin(\theta)$ and 2θ is the scattering angle). Q-range calibration was made using silver behenate. The X-ray beam size was 300×300 μm^2. WAXS measurements were carried out using the same equipment as for SAXS, but with a sample-to-detector distance of about 0.37 m giving an approximate range in q from 0.4 to 20 nm^{-1}. The beam size during the WAXS experiments was 500×500 μm^2. The local scattering from the sample

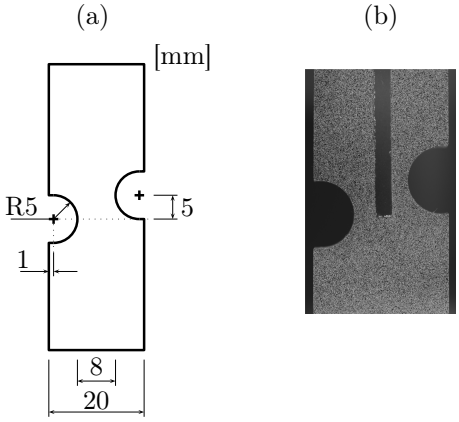

Figure 2: The geometry of the asymmetrically notched specimen (a) and a specimen with painted speckle pattern (b). The unpainted area shown in (b) is where the X-ray beam hit the specimen; this part was not painted to avoid scattering by the paint.

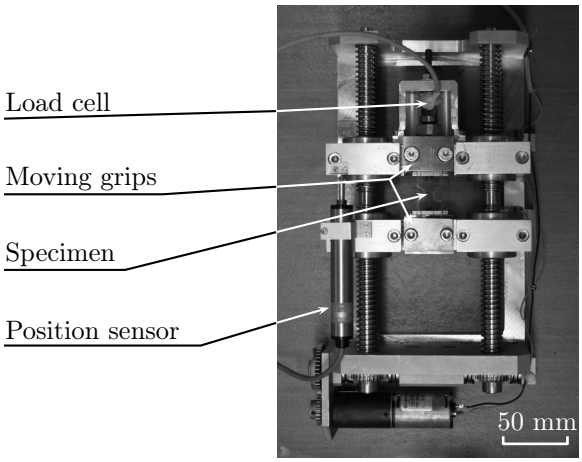

Figure 3: The custom built tensile test machine used for the *in-situ* loading.

was mapped at 30 points, with an equal spacing of 0.3 mm along the vertical centreline of the specimens by moving the translational stage of the beamline on which the loading device was mounted. The translational stage consisted of two Pro115 (Aerotech) linear stages with an accuracy of ± 6 μm and a repeatability of ± 1 μm. The starting point of the X-ray vertical scan was positioned by performing vertical and horizontal transmission scans and considering the geometry of the specimens. The X-ray acquisition times were 30 s per point for both SAXS and WAXS. The scattered X-rays were recorded using a Pilatus 1M (Dectris) 2D hybrid pixel detector and analysed using an in-house developed program. Data correction was made considering the transmission of the X-rays, the thickness of the specimens and subtracting the background contribution to the X-ray data. The transmission of the X-ray through the specimen is estimated measuring the intensity of the direct beam at a pin-diode detector placed on the beamstop. Specimen thickness is

estimated using the out-of-plane deformation measure with DIC. All X-ray scattering data were normalised by the appropriate specimen thickness. Figure 4 shows a corrected 2D SAXS pattern. 1D azimuthal ($I(\varphi)$ vs φ where φ is the azimuthal angle) and radial plots ($I(q)$ vs q) were extracted from the corrected 2D X-ray patterns to quantitatively evaluate the patterns. Azimuthal SAXS plots were made by averaging the scattering intensity at each azimuthal angle over a q-range from 0.25 to 0.61 nm^{-1}, the q-range is indicated in Figure 4. Radial plots from SAXS and WAXS patterns were made by averaging the scattering intensity for each radius over an angular sector of $\pm 10°$ around lines parallel and perpendicular to the loading direction, as indicated in Figure 4.

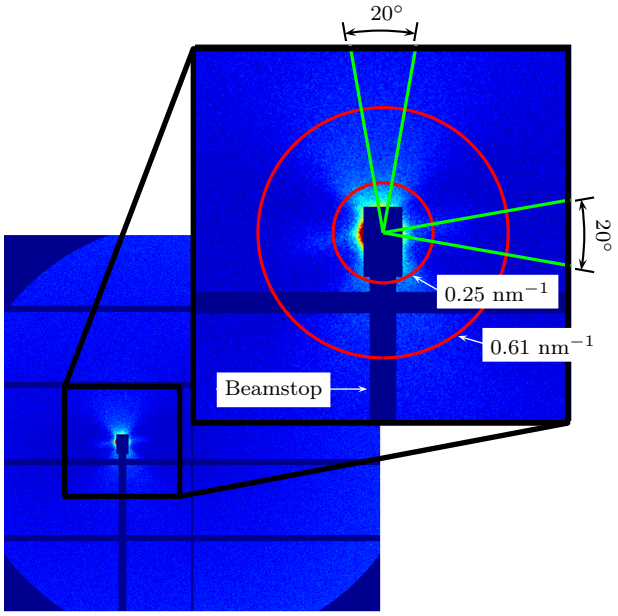

Figure 4: Full SAXS pattern as recorded by the Pilatus sensor on the left. The dark blue rectangular mesh in the images is due to space between the modules of the Pilatus detector. To the right is a magnified view of the area around the centre of the beam. The figure shows the radial interval over which the azimuthal data are averaged (red circles) as well as the two angular sectors over which the radial data are averaged (green lines). The uniaxial loading direction is vertical and is taken as the beginning of the azimuthal plot ($\varphi = 0$ at the bottom of the image).

3.4 Digital image correlation

Mesoscopic displacement fields were measured using 3D-surface digital image correlation (DIC). This was done using two Prosilica GT6600 (Allied Vision Technologies) 29-Megapixel digital cameras. The cameras were calibrated for stereo-vision allowing measurement of the out-of-plane deformation as well as the in-plane deformation. This involved stereo-correlation of pairs of images of the sample surface taken by the two cameras at the

same instance. A random speckle pattern was applied to the specimens surface, to facilitate correlation, using a water based paint (to ensure that the paint did not damage or react with the polymer). To avoid scattering by the paint, the area where the X-ray beam hit the samples was masked during the painting leaving an unpainted area down the centre of the specimen (see Figure 2). Due to this fact there were no deformation measurement at the points where the X-ray beam hit the specimens. This deformation can however be calculated by interpolating the measured deformation obtained in the pained region. This was done when correcting the X-ray data by normalisation using the specimen thickness. The thickness was interpolated linearly over width of the unpainted area. The largest relative error of the calculated thickness was estimated to about 1 % in the areas with the largest thickness gradients, i.e. at the edges of the necking zone. The error estimation is based on tests with full DIC fields (i.e. without the unpainted area). On this DIC field the measured data was removed over an area matching the unpainted area and replaced with a linearly interpolated field. This interpolation was then compared to the measured values. The DIC system was set up to take an image every time the X-ray detector acquired data using a trigger signal from the detector.

The stereo calibration as well as the image correlation was made using the commercial software Vic-3D (Correlated Solutions). The stereo calibration was performed using images of a reference grid in different positions and rotations, cf. Solutions (2010). The overall calibration error was 0.042 and 0.052 pixels for the DIC during the SAXS experiments and the WAXS experiments respectively. The calibration error is defined as the standard deviation of the residuals (i.e. the difference between the measured position of the calibration grid points and their theoretical positions) for all calibration images, cf. Solutions (2010). The image correlation used to calculation of the mesoscopic deformation was made using a correlation window of 61×61 pixels and a step size (the distance between the analysed points) of 10 pixels. The image pixel size for the DIC was approximately 12 µm on the specimen during the SAXS experiments and 13 µm during the WAXS experiments. With this pixel size the physical size of the DIC correlation windows, for deformation calculations, was approximately 730×730 µm^2 and 790×790 µm^2, for the SAXS and WAXS experiments respectively. Pixel subsets in the reference images (of the undeformed specimens) were correlated to subsets in each of the images of the sample in a deformed state. The displacements from the correlation software were used to calculate the displacements gradients using an in-house developed code. These were in turn used to construct the full strain field (using the same code). The strain was calculated using the closest neighbour points on a regular 10 pixel grid.

4 Results

A number of experiments have been performed with the described set-up and a selection of these is presented to illustrate the new insight that can be gained by using this integrated multi-scale approach.

4.1 SAXS with *in-situ* loading and DIC

Figure 5 shows the force-displacement curve measured by the tensile test machine for a characteristic experiment on PC. The slightly noisy response is due to non-optimal gearing on the tensile machine for the low displacement rate. Figure 5 also shows the strain field measured using DIC, the white area down the centre is where the specimen was masked during painting. The presented strain measure, E_1, is the major principal strain, i.e. the largest eigenvalue of the Green-Lagrange strain tensor, $\boldsymbol{E}$, defined as

$$\boldsymbol{E} = \frac{1}{2}(\boldsymbol{F}^T\boldsymbol{F} - \boldsymbol{I}), \tag{1}$$

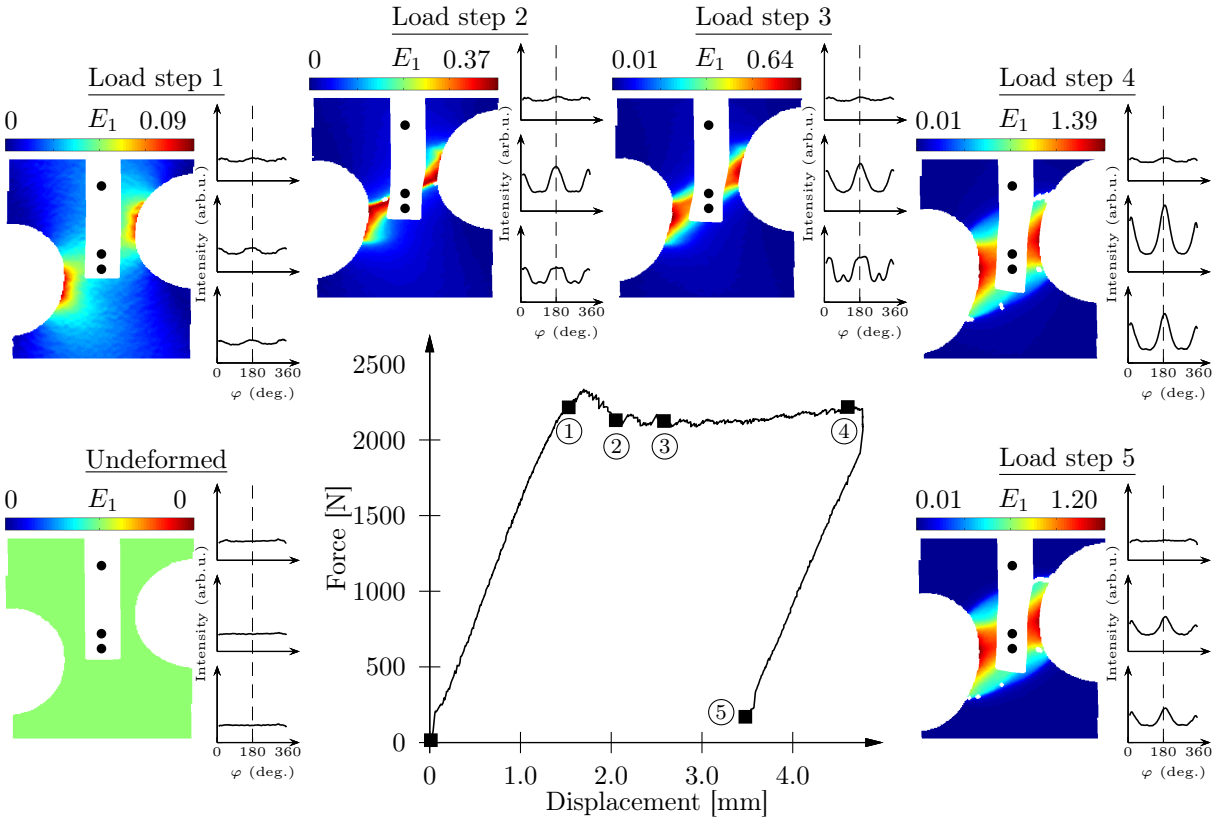

Figure 5: Force-displacement curve measured by the tensile test machine for an asymmetrically notched PC specimen. The test was conducted with a constant displacement rate of 0.01 mm/min. The figure also shows the major principal strain field, E_1, measured using DIC at six load levels, as well as the SAXS azimuthal plots at three spatial points at the six load levels. The scale of the axes are the same for all azimuthal plots. The spatial points are indicated in the DIC images as black dots down the centreline of the specimen. The presented strain fields corresponds to the X-ray measurement at the centre point of the specimen. The loading direction is vertical.

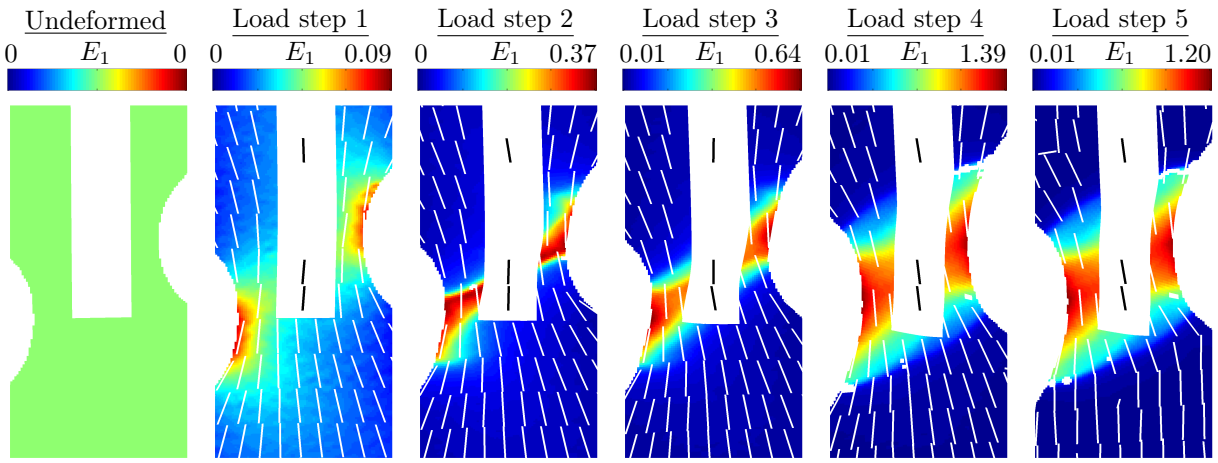

Figure 6: Correlation of the direction of the major principal strain and the orientation of X-ray scattering patterns. The figure shows the major principal strain field, E_1, between the notches. The white lines show the major principal strain direction (from DIC) while the black lines at the central white strip of the specimen indicate the angle of the maximum intensity of the azimuthal SAXS plots (see Figure 5).

where $\boldsymbol{F}$ is the deformation gradient and $\boldsymbol{I}$ is the identity tensor. The DIC result shows an inhomogeneous deformation state before the force peak with strain concentrations at the notches (load step 1). A localised band of high strains evolves around the force peak and broadens with increasing local strain with further increasing grip displacement (load steps 2-4). The unloaded state shows large residual deformations (load step 5).

Azimuthal SAXS plots from three spatial points of the specimen at each load level are also shown in Figure 5. The three points are the start and end points of the line scan and the centre point of the specimen. These were positioned using the coordinates from the DIC and from the translational stage at the beamline. At each X-ray measurement along the vertical line the following was measured simultaneously during the continuous loading: macroscopic force, DIC for mesoscopic deformation measurements and X-ray scattering. The macroscopic grip displacement was 0.005 mm during the 30 s X-ray acquisition. For presentation purposes, the strain fields correspond to the X-ray measurement taken at the centre point, see Figure 5. Due to the low deformation rate, there are no qualitative differences between the presented strain fields and the strain fields corresponding to the X-ray measurements at the other spatial points at the same load step. The azimuthal SAXS plots show an evolution of the scattering, with respect to the load, from an initial isotropic pattern (with the same scattering in all directions) at each point, to an anisotropic scattering. The anisotropic scattering evolves from a broad, almost double, central peak (at $\varphi = 180°$) alignment to a narrow, single central peak (seen in the plots from the lowest spatial point at load step 2-4). The spatial mapping reveals a character in the scattering that is not visible when only looking at the centre point, namely an extra, secondary alignment almost perpendicular to the main alignment. This effect is seen as two extra

peaks (at approximate 90° and 270°) in the azimuthal plots from the lowest spatial point at load step 2 and 3. The secondary alignment is only visible during a limited displacement range following the force peak, after which it is no longer visible. After unloading some of the aligned scattering is still present. The alignment of the strongest SAXS signal is almost parallel to the load direction, which suggests main changes perpendicular to the deformation. The azimuthal SAXS plots from the centre point of the specimen show a similar behaviour, except the secondary alignment and larger intensity at $\varphi = 180°$. The azimuthal plots from the top point show a slight alignment that are more or less constant between load step 1 to 5, after unload this alignment disappears. This is consistent with the strain field from DIC.

The directions of the major principal strain are plotted in Figure 6 together with the direction of the maximum intensity of the azimuthal curves shown in Figure 5. These results indicate a direct correlation between both measurements. The figure shows how the principal direction of the major strain in the bridge between the notches and the direction of maximum intensity of the azimuthal SAXS curves evolves; from a vertical, or slightly right-tilted direction before the macroscopic force peak (load step 1) to a clearly left-tilted direction after the force peak (load step 2-5). The orientations remain after unload (load step 5).

Figure 7 shows radial plots extracted from corrected SAXS patterns from the centre point of the specimen at the load steps shown in Figure 5. The curves obtained parallel to

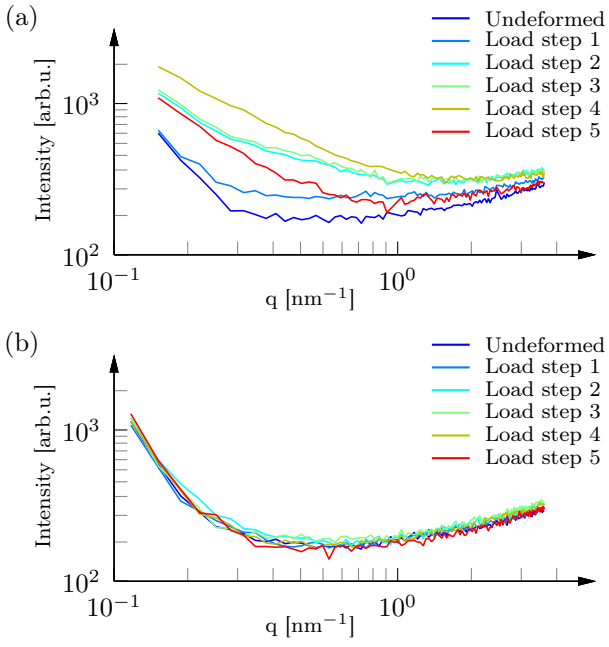

Figure 7: Radial plots extracted from the corrected 2D SAXS patterns from the centre point of the specimen at the load steps shown in Figure 5. (a) Curves parallel to the loading direction and (b) curves perpendicular to the loading direction.

the loading direction (Figure 7a) show a clear change in slope as the specimen is deformed, with a very clear change as the deformation passes beyond the macroscopic force peak (load step 1-2). The change in slope indicates modifications of the size and/or shape of the scattering objects, some of which remains after unload. The curves obtained perpendicular to the loading direction (Figure 7b) do not show any significant change in slope or intensity as the specimen deforms.

4.2 WAXS with *in-situ* loading and DIC

Figure 8 shows results from a test using the WAXS set-up. The figure shows the strain field, E_1, at six load levels measured using DIC, plus 2D WAXS patterns at three spatial points down the centreline of the specimen at each load level. As for the results in Section

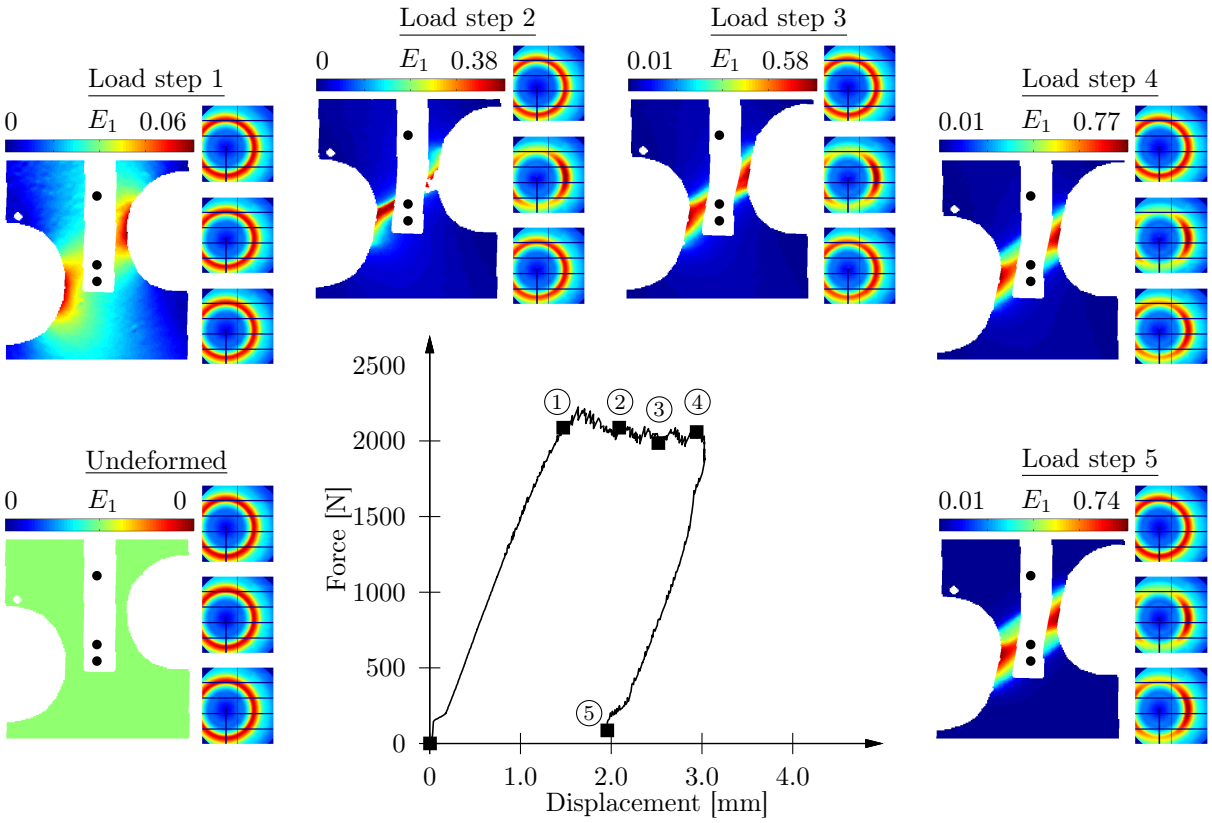

Figure 8: Force-displacement curve measured by the loading device for an asymmetrically notched PC specimen. The test was conducted with a constant displacement rate of 0.01 mm/min. The figure also shows the major principal strain field, E_1, measured using DIC at six load levels, as well as the 2D WAXS patterns at three spatial points at the six load levels. The spatial points are indicated in the DIC images as black dots down the centreline of the specimen. The presented strain fields corresponds to the X-ray measurement at centre point of the specimen. The direction of load is vertical.

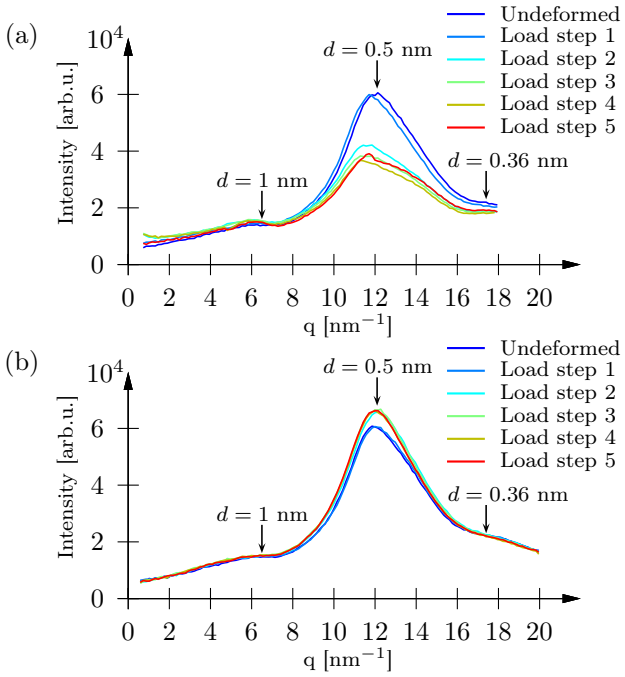

Figure 9: Radial plots from the centre point WAXS patterns shown in Figure 8. (a) Curves parallel to the load direction and (b) curves perpendicular to the loading. The arrows indicate the three main peaks of the diffractogram.

4.1 the presented strain fields in Figure 8 correspond to the X-ray measurement at the centre point of the specimen. The mesoscopic deformation at load steps 1-3 is similar as for load steps 1-3 in Figure 5. Due to time limitation the unloading was made earlier during the WAXS experiments. In the same way as for the SAXS experiments the three points are the start and end point of the line scan and the centre point of the specimen. The WAXS measurements show an initial isotropic scattering at each point that evolves into an anisotropic scattering with a larger intensity in the direction perpendicular to the macroscopic loading direction. Most of the alignment in the WAXS is still present after unload.

Figure 9 shows radial plots extracted from the corrected 2D WAXS patterns from the centre point of the specimen shown in Figure 8. The curves show three main peaks associated with the intermolecular correlation distance ($q = 6.5$ nm^{-1}, $d = 1$ nm), the average correlation distance between neighbouring chains ($q = 12.1$ nm^{-1}, $d = 0.5$ nm) and a combined inter- and intramolecular correlation ($q = 17.4$ nm^{-1}, $d = 0.36$ nm) indicated by arrows in Figure 9. Due to the different q-range in both directions, the third peak ($q = 17.4$ nm^{-1}, $d = 0.36$ nm) is only clearly observed in Figure 9b. The position of these peaks is consistent with the results reported by Schubach and Heise (1986). The positions of the peaks seem to change slightly as the specimen deforms, which indicates small changes in correlation distances. The curves obtained parallel to the macroscopic loading direction (Figure 9a) show a large decrease in intensity of the peak at approximately 12 nm^{-1} as the

specimen is deformed, with a significant decrease in intensity after the macroscopic force peak. The reduced intensity remains after unload. The curves extracted perpendicular to the loading direction (Figure 9b) show an increase in intensity of the peak centred at $q = 12$ nm^{-1} as the specimen is loaded beyond the macroscopic force peak (load step 1-2). Other than this there are no significant changes in intensity in the curves perpendicular to the loading direction.

5 Discussion

5.1 Material response

Due to the highly inhomogeneous deformation revealed by the DIC in the presented tensile tests of PC, it is clear that it is insufficient to use conventional techniques such as extensometers when measuring the deformation. Instead full-field methods such as DIC must be utilised. DIC provides the possibility to output all components of the displacement gradient over the full sample area. Although not fully shown here, this makes it possible to study different modes of deformation such as axial stretching or shearing. The need for 3D-surface DIC is evident due to the large out-of-plane deformation of PC. Relative out-of-plane displacements of over 0.7 mm have been measured in the centre point of the specimen (the relative displacement is zero close to the grips) during the presented experiments, this implies a thickness reduction of over 1.4 mm (about 30 % less than the initial value). 3D-surface DIC allows the true in-plane and out-of-plane deformations to be measured. The measured out-of-plane deformation must be used when correcting the X-ray data for changes in specimen thickness, as the thickness of the specimen will influence the total scattered intensity. If this significant change in thickness is not taken into account, comparisons of the scattering intensity at different load levels of spatial locations will be incorrect.

The azimuthal SAXS plots presented in Figure 5 show a well oriented scattering parallel to the macroscopic loading direction. The plots also show features that would not be observed when only probing the centre point of a specimen or with an average over a large area (e.g. with SANS or NMR). Figure 6 shows a qualitative correlation between the direction of the major principal strain and the orientation of the scattering at small angles. The figure shows that the orientation of the microstructure of PC in the SAXS region follows the directions of the mesoscopic deformation measured with DIC. Similar correlation has previously been shown for semi-crystalline HDPE, e.g. Farge et al. (2013). However, the nature of the SAXS signal for HDPE can have different origin than in our case. The SAXS data show a change in size and/or shape of the scattering objects perpendicular to the macroscopic loading as the specimen is deformed (seen as the change in slope of the curves in Figure 7a). The origin of the scattering entities at small angles is not yet established and is out of the scope of the manuscript.

Following the same tendency as the azimuthal SAXS plots, the WAXS patterns in Figure 8 show oriented scattering. The largest change in the wide angle scattering is in

the direction parallel to the macroscopic loading at the peak centred at $q = 12$ nm^{-1}, see Figure 9a. This result indicates a significant loss of order between neighbouring chains oriented perpendicular to the loading direction. Furthermore, the increase of intensity at the same peak, in the direction perpendicular to the loading, suggests alignment of the polymer chains in the loading direction.

The radial plots shown in Figures 7 and 9 show some elastic recovery of the scattering in the SAXS region, while the scattering remains unchanged after unload in the WAXS region. This indicates that the elastic recovery of the deformation (after unload) shown by DIC in Figure 5 and 8 is due to reversible mechanisms in the SAXS region while the residual deformation is mostly due to changes in the intermolecular structure of the material in the WAXS region.

The use of full-field DIC provides the ability to investigate different modes of deformation (not shown here) on a local scale. By combining DIC with spatial mapping of SAXS and WAXS new insights of the coupling between the local micro-structural behaviour and different mesoscopical deformation modes can be provided.

5.2 Experimental method

The results discussed in this study are from experiments using a constant displacement rate of the machine grips of 0.01 mm/min. This rate was chosen to be able to load continuously without the material undergoing too large deformation while acquire scattering data. An alternative approach is to use intermittent loading with a higher displacement rate and keeping the deformation fixed during the X-ray measurements. While more time efficient, this approach has the negative effect that polymeric material will undergo significant relaxation when the deformation is fixed. When reloading PC after relaxation beyond the force peak the force-displacement curve will show a new force peak. The relaxation and the recurrent force peak make it difficult to relate the measured points to points on a force-displacement curve using monotonic load. Also the X-ray measurements will be made on a relaxed material instead of, as in this study, a loaded material.

The evolution of the scattering, with respect to the deformation, is captured over a large area of the specimen by performing the spatial mapping of the X-ray scattering while deforming the specimens continuously using a slow loading rate. This, in combination with full-field DIC measuring the deformation, provides a large amount of experimental data from a single experiment. This is not only time efficient, but also makes the coupling of the different measurements more reliable since the uncertainties of combining data from different experiments are avoided.

To avoid scattering from the painted speckle pattern needed for DIC, an area down the centre of specimen where the X-ray measurements were taken was left unpainted. As a consequence of this, no deformation were measured at the exact points of the X-ray measurements. However, the mesoscopic deformation at that points can be calculated by interpolating the measured deformation data over the unpainted area. This was done when correcting the X-ray data by normalisation using the specimen thickness.

6 Conclusion

The method presented in this paper has combined well established methods of X-ray scattering, digital image correlation and uniaxial loading in one simultaneous experiment and with good spatial resolution. This approach can be extended to any kind of polymeric materials or polymer-based nanocomposites. The X-ray data provide information on the supramolecular and molecular level (nanometric scale). The deformation is measured *in-situ*; the macroscopic deformation is measured using sensors on the tensile machine and the full-field mesoscopic deformation is measured using 3D-surface DIC. Thus allowing investigation of the material behaviour on macro-, meso- and nano-scales simultaneously. The use of full-field DIC and X-ray mapping reveals inhomogeneous behaviour in the mesoscopic deformation as well as in the local behaviour of the microstructure on a nanometre scale. A direct correlation between the major principal strain direction and the maximum anisotropy direction of the SAXS data is indicated for amorphous polycarbonate. The inhomogeneous deformation behaviour of this type of material renders conventional measuring techniques, such as extensometers, virtually useless. The same applies for one and two dimensional video-based methods, such as video extensometry or DIC using a single camera, due to the large out-of-plane deformations during necking. This makes it a necessity to use a three-dimensional, full-field method when characterising the deformation. By deforming the specimens continuously *in-situ*, the X-ray scattering is measured on a loaded specimen. If intermittent loading is used the scattering will be measured on a relaxed specimen, as the polymer starts to relax as soon as the loading is stopped. The use of *in-situ* DIC enables correlation of the mesoscopic deformation to the local behaviour of the nanoscopic microstructure. It is shown that the X-ray scattering is dependent on the spatial location as well as the local deformation. The spatial mapping reveals unique characters in the scattering present at other locations than the centre point. This shows the importance of measuring the X-ray scattering at more points than merely the centre point, to fully characterise the behaviour of the microstructure. By combining SAXS and WAXS, information is gained about structures with sizes in the range from about 100 nm down to intermolecular distances of a few Ångström. A more detailed analysis of this information will be presented in a future paper. With these data the macroscopic and mesoscopic deformation can be correlated to the behaviour of the microstructure during deformation, and provide important information when developing micro-mechanical based constitutive models.

Acknowledgements

The financial support from the Crafoord foundation, grant no. 20110521 and 20120632, is greatly acknowledged. We are also grateful for the beamtime and support received from the MAX IV Laboratory and the I911-SAXS beamline, proposal 20120327. We gratefully acknowledge the work by Zivorad Zivkovic for building the tensile test machine and the assistance of Erika Tudisco during the experiments.

References

Arruda, E. M., Boyce, M. C., 1993. A three-dimensional constitutive model for the large stretch behavior of rubber elastic materials. Journal of the Mechanics and Physics of Solids 41 (2), 389–412.

Buisson, G., Ravi-Chandar, K., 1990. On the constitutive behaviour of polycarbonate under large deformation. Polymer 31 (11), 2071–2076.

Choi, T., Fragiadakis, D., Roland, C. M., Runt, J., 2012. Microstructure and segmental dynamics of polyurea under uniaxial deformation. Macromolecules 45 (8), 3581–3589.

Daiyan, H., Andreassen, E., Grytten, F., Osnes, H., Gaarder, R., 2012. Shear testing of polypropylene materials analysed by digital image correlation and numerical simulations. Experimental Mechanics 52 (9), 1355–1369.

David, O. B., Banks-Sills, L., Aboudi, J., Fourman, V., Eliasi, R., Simhi, T., Shlayer, A., Raz, O., 2013. Evaluation of the mechanical properties of pmma reinforced with carbon nanotubes-experiments and modeling. Experimental Mechanics.

Farge, L., André, S., Meneau, F., Dillet, J., Cunat, C., 2013. A common multiscale feature of the deformation mechanisms of a semicrystalline polymer. Macromolecules 46 (24), 9659–9668.

G'sell, C., Jonas, J., 1979. Determination of the plastic behaviour of solid polymers at constant true strain rate. Journal of Materials Science 14 (3), 583–591.

Harren, S., 1995. Toward a new phenomenological flow rule for orientationally hardening glassy polymers. Journal of the Mechanics and Physics of Solids 43 (7), 1151–1173.

Harrysson, M., Ristinmaa, M., Wallin, M., Menzel, A., 2010. Framework for deformation induced anisotropy in glassy polymers. Acta Mechanica 211 (3-4), 195–213.

Haynes, A., Coates, P., 1996. Semi-automated image analysis of the true tensile drawing behaviour of polymers to large strains. Journal of Materials Science 31 (7), 1843–1855.

Hubert, L., David, L., Seguela, R., Vigier, G., 2004. Small-angle x-ray scattering investigation of the deformation processes in the amorphous phase of high density polyethylene. Polymer International 53 (5), 582–585.

Humbert, S., Lame, O., Chenal, J., Rochas, C., Vigier, G., 2010. Small strain behavior of polyethylene: in situ saxs measurements. Journal of Polymer Science Part B: Polymer Physics 48 (13), 1535–1542.

Humbert, S., Lame, O., Vigier, G., 2009. Polyethylene yielding behaviour: What is behind the correlation between yield stress and crystallinity? Polymer 50 (15), 3755–3761.

Labrador, A., Cerenius, Y., Svensson, C., Theodor, K., Plivelic, T., 2013. The yellow mini-hutch for saxs experiments at max iv laboratory. In: Journal of Physics: Conference Series. Vol. 425. IOP Publishing, p. 072019.

Lin, W., Kramer, E. J., 1973. Small-angle x-ray scattering from amorphous polycarbonate. Journal of Applied Physics 44 (10), 4288–4292.

Lu, J., Ravi-Chandar, K., 1999. Inelastic deformation and localization in polycarbonate under tension. International journal of solids and structures 36 (3), 391–425.

Miehe, C., Göktepe, S., Lulei, F., 2004. A micro-macro approach to rubber-like materialspart i: the non-affine micro-sphere model of rubber elasticity. Journal of the Mechanics and Physics of Solids 52 (11), 2617–2660.

Miehe, C., Göktepe, S., Mendez Diez, J., 2009. Finite viscoplasticity of amorphous glassy polymers in the logarithmic strain space. International Journal of Solids and Structures 46 (1), 181–202.

Parsons, E., Boyce, M., Parks, D., 2004. An experimental investigation of the large-strain tensile behavior of neat and rubber-toughened polycarbonate. Polymer 45 (8), 2665–2684.

Parsons, E., Boyce, M., Parks, D., Weinberg, M., 2005. Three-dimensional large-strain tensile deformation of neat and calcium carbonate-filled high-density polyethylene. Polymer 46 (7), 2257–2265.

Poulain, X., Kohlman, L., Binienda, W., Roberts, G., Goldberg, R., Benzerga, A., 2013. Determination of the intrinsic behavior of polymers using digital image correlation combined with video-monitored testing. International Journal of Solids and Structures 50 (11), 1869–1878.

Rössle, W., Lindner, P., Dettenmaier, M., 1989. Deformation of glassy polycarbonate studied by neutron scattering. Physica B: Condensed Matter 156, 414–416.

Schubach, H. R., Heise, B., 1986. Structure and anisotropy in polycarbonate. i. short range order of amorphous polycarbonate revealed by waxs. Colloid and Polymer Science 264 (4), 335–342.

Solutions, C., 2010. Vic-3D Testing Guide. Correlated Solutions.

Sutton, M., Orteu, J., Schreier, H., 2009. Image correlation for shape, motion and deformation measurements: basic concepts, theory and applications. Springer.

Toki, S., Sics, I., Ran, S., Liu, L., Hsiao, B., 2003. Molecular orientation and structural development in vulcanized polyisoprene rubbers during uniaxial deformation by in situ synchrotron x-ray diffraction. Polymer 44 (19), 6003–6011.

Viggiani, G., Hall, S., 2008. Full-field measurements, a new tool for laboratory experimental geomechanics. In: Proceedings of the 4th International Symposium on Deformation Characteristics of Geomaterials (Burns SE, Mayne PW and Santamarina JC (Eds.)). pp. 3–26.

Vogt, V., Dettenmaier, M., Spiess, H., Pietralla, M., 1990. Orientation of the diphenylene propane unit in stretched polycarbonate from two-dimensional magic-angle-spinning nmr. Colloid and Polymer Science 268 (1), 22–27.

Wang, M. C., Guth, E., 1952. Statistical theory of networks of non-gaussian flexible chains. The Journal of Chemical Physics 20, 1144.

Wu, P. D., van der Giessen, E., 1993. On improved network models for rubber elasticity and their applications to orientation hardening in glassy polymers. Journal of the Mechanics and Physics of Solids 41 (3), 427–456.

Paper B

Jonas Engqvist, Mathias Wallin, Stephen A. Hall,
Matti Ristinmaa and Tomás S. Plivelic

Measurement of multi-scale deformation of polycarbonate using X-ray scattering with in-situ loading and digital image correlation

Polymer 82 (2016), 190-197

Measurement of multi-scale deformation of polycarbonate using X-ray scattering with *in-situ* loading and digital image correlation

Jonas Engqvist[a], Mathias Wallin[a], Stephen A. Hall[a,b], Matti Ristinmaa[a] and Tomás S. Plivelic[c]

[a]Division of Solid Mechanics Lund University, Box 118, S-221 00 Lund, Sweden

[b]European Spallation Source AB, P.O. Box 176, 221 00, Lund, Sweden

[c]MAX IV Laboratory, Lund University, P.O. Box 118, 221 00, Lund, Sweden

Abstract

Deformation of amorphous, glassy polycarbonate (PC) is characterised over a wide range of length-scales using spatially-resolved wide angle X-ray scattering (WAXS) with simultaneous digital image correlation and *in-situ* uni-axial loading. Novel observations are presented on the correlation of the evolution of the molecular structure linked to the relevant local macroscopic measures of strain as the sample deforms. This provides new insights into the mechanisms of deformation in amorphous, glassy polymers. Strains and evolving anisotropy are observed, and quantified, at different length scales identified from the WAXS measurements connected to inter- and intramolecular structures. The inter-molecular structures show permanent deformations in the form of unrecoverable stretches and reorientations, whilst intra-molecular structures show recoverable strains and unrecoverable reorientations. Such insights pave the way for development of enhanced constitutive models for amorphous glassy polymers with a correct micro-mechanical basis and calibrated evolution of anisotropy.

1 Introduction

Polycarbonate (PC) is a glassy polymer at room temperature with good mechanical properties, such as high impact strength, good optical properties and a comparatively high glass transition temperature, cf. Mark (2007). Due to these favourable properties it is widely used in industry and consumer products, e.g., as protective glass and equipment housing in the electronics industry. The design process for such applications requires accurate understanding of the material properties and, importantly, how the material responds and evolves under mechanical load. However, PC (as many other polymers) exhibits highly inhomogeneous deformation phenomena, e.g., necking and strain localisation, such that local deformation differs from the overall macroscopic response, e.g., Buisson and Ravi-Chandar (1990); Lu and Ravi-Chandar (1999); Engqvist et al. (2014). Such deformation responses are generally attributed to mechanisms occurring at the molecular-scale. As such, commonly used material models for the mechanical behaviour of PC invoke idealised representations of polymer chain networks (e.g., the "3-chain" model by Wang and Guth (1952), the "8-chain" model by Arruda and Boyce (1993), the full-network model by Wu and van der Giessen (1993) and the micro-sphere model by Miehe et al. (2009)). Common to these models is that the permanent deformation, i.e., the plasticity, is modelled to occur within the individual chains. In an extension to such approaches, Harrysson et al. (2010) presented a model in which plasticity originates from both stretching of polymer chains and their reorientation via an evolving chain orientation distribution function (CODF). The experimental support for the molecular-scale assumptions underlying all of these models is, however, limited. For example, it is not clear for PC if the polymer chains themselves show permanent stretching and there are very few data on the evolution of the orientation distribution function of the chains. Furthermore, due to the spatially heterogeneous nature of the deformation in PC described above, any measurement of the molecular structure and its evolution should be spatially resolved and linked to appropriate local macroscopic strain measurements.

The molecular structure in undeformed PC has been studied using neutron scattering together with numerical simulations, e.g., Červinka et al. (1987); Lamers et al. (1992, 1994); Eilhard et al. (1999). Changes in the microstructure of amorphous glassy polymers due to deformation and/or heat treatment on predeformed specimen have been studied using wide angle X-ray scattering (WAXS), e.g., Mitchell and Windle (1985); Schubach and Heise (1986); Del Val et al. (1995). Neutron or X-ray scattering techniques have also been used during *in-situ* deformation studies on semi-crystalline polymers, e.g., Butler and Donald (1998); Yeh et al. (2003); Brown et al. (2008); Stoclet et al. (2012); Farge et al. (2013); Wang et al. (2014); Guo et al. (2015), but not on amorphous glassy polymers. Also, in general such studies lack spatial resolution in the scattering data and use macroscopic or, at best, *ex-situ* local "full-field" deformation measurements.

Neutron and X-ray techniques, such as those described above, can provide details on the molecular-scale structures of PC and indicate the micro-/nano-scopic mechanisms of interest. However, to understand how these mechanisms are linked to overall material

behaviour requires coupling to measurements at larger scales. In particular, the molecular-scale observations should be linked to macroscopic strain measurements. Further to this, the heterogeneity of the strain response requires that local "full-field" measurements are made. Spatially-resolved (full-field) mesoscopic surface deformation can be measured using optical techniques, such as digital image correlation (DIC), cf. Grytten et al. (2009); Poulain et al. (2013).

If the molecular-scale mechanisms of deformation can be linked to the macroscopic scale material response by integration of X-ray/neutron scattering and strain-field measurements, then all of the necessary ingredients are in place for developing a physically-based model to describe the mechanical behaviour. This is the ultimate objective of this work.

This paper presents new results from simultaneous, spatially resolved WAXS and full-field 3D-surface DIC measurements of *in-situ* uni-axial loading of PC, following the approach developed by Engqvist et al. (2014). This approach permits the local deformation to be studied in terms of the evolution and strain in the molecular structure linked to local macroscopic measures of strain, as the sample deforms under uni-axial loading. The experiments are first described, followed by a presentation and discussion of the results and observations at the different scale lengths before concluding on the molecular-scale origins of the observed macroscopic response of the material.

2 Experiments

The experiment described in the following involved *in-situ* tensile loading with simultaneous WAXS and 3D-surface DIC. A detailed description of the experimental set-up used in this study is given in Engqvist et al. (2014). The PC material used in the study is Makroclear®, a commercial amorphous PC manufactured by Arla Plast.

Symmetrically notched specimens, with a notch radius of 5 mm and a rectangular cross section area of 8×5 mm^2 were machined from a sheet of 5 mm thickness, see Figure 1. Apart from the machining, no additional treatments of the material were made. The specimens were loaded under uni-axial tension *in-situ* during wide angle X-ray scattering (WAXS) measurements, using a custom built tensile testing device. Both loading and unloading was performed using a constant macroscopic displacement rate of 0.01 mm/min, measured on the machine grips. The experiments were performed at the I911-SAXS beamline at the synchrotron MAX IV Laboratory (Lund University, Lund, Sweden). WAXS measurements were made using a wavelength, λ, of 0.91 Å and a sample-to-detector distance of 0.36 m giving a q-range of around 0.5-22 nm^{-1} (where $q = (4\pi/\lambda)\sin\theta$ and 2θ is the scattering angle). Q-range calibration was made using lanthanum hexaboride (LaB_6). A bi-dimensional hybrid pixel X-ray detector (Pilatus 1M, Dectris) was used to record the scattering data, which were corrected for: the transmission of the X-rays, the current specimen thickness (calculated from the DIC analysis) and air scattering (by subtracting the background scattering). The transmission of X-rays through the specimen was estimated using the intensity of the direct beam, measured using a pin-diode detector placed on the

beamstop. The local scattering was mapped using line scans of 20 spatial points along the centreline of the specimen. The distance between the points in the line scan was 0.5 mm and the exposure time for each WAXS image was 10 s. During the experiment a total of 100 line scans were performed. The time between two consecutive WAXS measurements at the same spatial point was 300 or 510 s, where the longer time was because of a background measurement which was made after every third line scan. For clarity, only scattering data from two of the 20 spatial points of the line scans are presented: point 1 (centre point) and point 7 along the line. From here on the points are referred to as point A and B, respectively (see Figure 3).

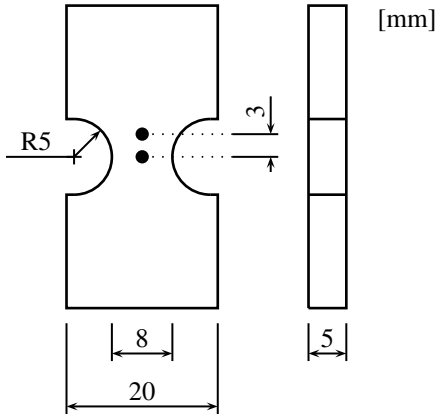

Figure 1: The geometry of the notched specimen. The dots indicates the positions from which measured X-ray scattering data is presented.

X-ray data are presented from the two points A and B. These points are selected to represent positions between the localisation bands (point A) and where the localisation front passes through (point B). Points far out from the localisation zone do not show any significant permanent changes in the microstructure.

3D-surface DIC was used to measure the deformation at the surface of the specimen *in-situ*, simultaneously with the scattering measurements. The synchronisation of the data from the different measurements (loading, DIC and WAXS) was achieved using a signal from the X-ray detector to the DIC-system that also was recorded in the loading system control software. A random speckle pattern was painted on the specimen using a water-based paint to facilitate the DIC. To avoid scattering by the paint, the area where the X-ray beam hit the specimen was left unpainted resulting in a blank area in the stretch fields, see Figure 3. Image correlation was made using the Vic-3D software (Correlated Solutions Inc.), using a correlation window size of 61×61 pixels and a step size of 7 pixels (distance between two adjacent windows). The pixel size of the photographs used in the DIC was approximately 13 μm on the specimen. Stretch calculations were made using the closest neighbouring windows on a regular, 7 pixel grid.

3 Results and discussion

3.1 Macroscopic deformation

Figure 2 shows the macroscopic force-displacement curve measured on the grips of the tensile test machine for the presented experiment on PC using a notched specimen. The curve exhibits a characteristic peak in the force after which the force suddenly drops, reaches a plateau and increases slightly with further grip displacement due to strain hardening of the material. After unloading to zero macroscopic force, the curve shows a large permanent deformation. When reloading (after unloading) the force reaches the same level as before the unloading. The highlighted points on the force-displacement curve show six sampling points for the line scans for which DIC stretch fields are presented in Figure 3.

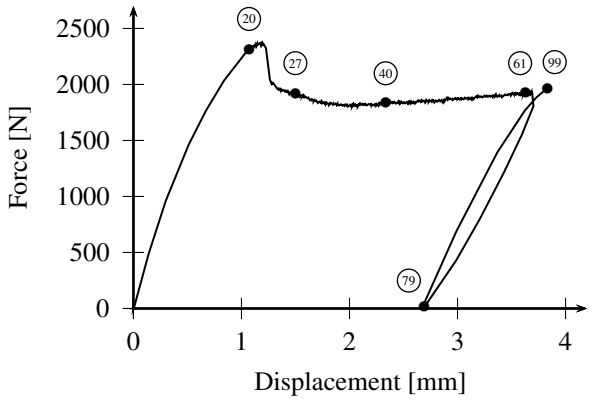

Figure 2: Macroscopic force-displacement curve. The symbols show six sampling points for the line scans at which DIC stretch fields are presented in Figure 3.

3.2 Mesoscopic deformation from 3D-surface DIC

To calculate the current thickness of the specimen as well as the mesoscopic stretch, 3D-surface DIC was used. Figure 3 shows the stretch fields at six sampling points. The presented DIC fields are measured simultaneously with the X-ray measurements at the centre point of the specimen (point A). Due to the low deformation rate, there are no qualitative differences between the different deformation fields during the same line scan. In the following, the principal stretches ($\Lambda_I^{meso} \geq \Lambda_{II}^{meso} \geq \Lambda_{III}^{meso}$), i.e., the square root of the eigenvalues to right Cauchy-Green deformation tensor, are used as a deformation measure. Due to the geometry of the specimen, Λ_I^{meso} is dominated by the longitudinal in-plane deformation, Λ_{II}^{meso} by the transverse in-plane deformation and Λ_{III}^{meso} by the out-of-plane deformation. The right Cauchy-Green deformation tensor, $\boldsymbol{C}$, is defined as

$$\boldsymbol{C} = \boldsymbol{F}^T \boldsymbol{F}, \tag{1}$$

where $\boldsymbol{F}$ is the deformation gradient. The deformation gradient is calculated using a symmetry assumption of the displacements of the front (photographed) and back surfaces of the specimen. This assumptions also implies an assumption of homogeneous deformation through the thickness of the specimen. Figure 3 shows the evolution of the major (tensile) principal stretch fields, Λ_I^{meso}. It can be concluded that the deformation is inhomogeneous even before the macroscopic force peak in Figure 2 is reached (line scan 20), with higher stretches between the notches, see Figure 3. Two bands of highly localised deformation are formed at the force peak (line scan 27). With increasing grip displacement, a cross-like pattern of large stretches is formed connecting the two localisation bands, which evolves into a broad zone of large deformations with further loading (line scans 40-61). The deformation fields just before and after unloading, as well as after reloading are, qualitatively, very alike although the magnitude changes (line scans 61, 79 and 99). Large permanent deformations are still present after unloading to zero macroscopic force (line scan 79).

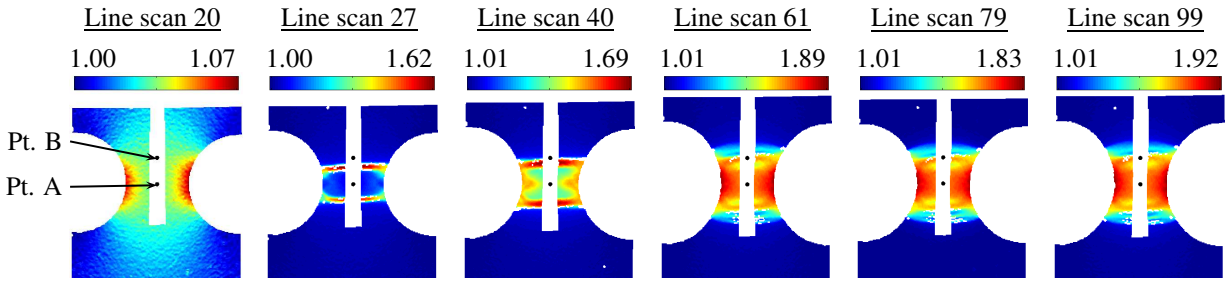

Figure 3: Deformation fields showing the major principal stretch, Λ_I^{meso}, measured using DIC at six line scans. The two black dots down the centreline of the specimen indicates the spatial points, point A and B, from which measured X-ray scattering data is presented. The loading direction is vertical.

Figure 4 presents the evolution of all the mesoscopic principal stretch components at the two spatial points from which measured X-ray scattering data are presented. These local values were calculated by linear interpolation of the measured displacements across the width of the unpainted area and averaged over an area of the same size as the X-ray beam, cf. Engqvist et al. (2014).

The mesoscopic stretch curves in Figure 4 follow the same trend; (1) the curves start off with a moderate change until the localisation zone is formed (and passes through the WAXS measurement points on the specimen, cf. Figure 3); (2) after the localisation is formed, the stretch rate increases significantly. The increase in stretch rate of Λ_{III}^{meso} at point A starts slightly earlier than for the other principal stretches. As for the macroscopic curve in Figure 2, the unloaded state shows large permanent deformations on the local level.

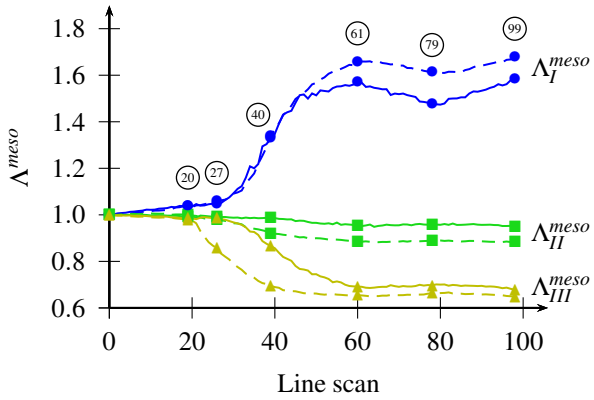

Figure 4: Principal stretches Λ_I^{meso} (—●—), Λ_{II}^{meso} (—■—) and Λ_{III}^{meso} (—▲—) calculated from the DIC fields at two spatial point on the specimen: point A (dashed line) and point B (solid line). The symbols on the curves indicate the line scans for which the stretch fields are presented in Figure 3.

3.3 Deformation of the microstructure analysed using WAXS

Figure 5 presents normalised 2D WAXS patterns at the centre point, point A, for seven different line scans. As reported in Mitchell and Windle (1985) and Schubach and Heise (1986), the undeformed state shows a uniform amorphous halo that looses its isotropy as the material is deformed. Data were extracted from 2D scattering patterns in two ways: (1) 1D radial profiles (I(q) vs q) and (2) 1D azimuthal profiles (I(φ) vs φ).

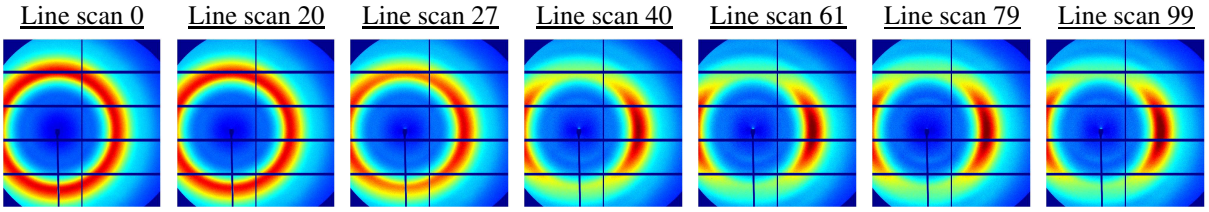

Figure 5: WAXS patterns from point A, the centre point of the specimen, at seven line scans. The main diffraction peak is visible as a red ring in line scan 0. Direction of load is vertical.

3.3.1 Radial plots

Radial plots (I(q) vs q) were extracted by averaging the data in small angular sectors ($\pm 5°$) around the loading direction and perpendicular to this direction. To fill in the gaps in the radial data due to the detector mesh (see Figure 5), the averaging was made over the two opposing angular sectors (e.g. over both the left and right directions perpendicular to the loading). Values extracted on the dark detector mesh were removed prior to the averaging. The radial data were smoothed across the load history using a robust discretised smoothing

spline, cf. Garcia (2010). Figure 6 shows 1D profiles extracted in the two directions for the undeformed state as well as the six line scans shown in Figure 3. Other authors, Mitchell and Windle (1985), Schubach and Heise (1986), Lamers et al. (1992) and Eilhard et al. (1999), have identified three peaks in the studied q-range and have related these to: the correlation between consecutive carbonate groups along the chain ($q = 6.2$ nm^{-1}, $d = 1.0$ nm); the distance between directly neighbouring chains ($q = 12$ nm^{-1}, $d = 0.52$ nm); a mixture of inter- and intramolecular correlations ($q = 18$ nm^{-1}, $d = 0.35$ nm). However, the current WAXS measurements performed during *in-situ* deformation show that the slightly asymmetric (in the undeformed state) amorphous halo consists of two distinct peaks, which become more apparent with the increasing deformation, see Figure 6.

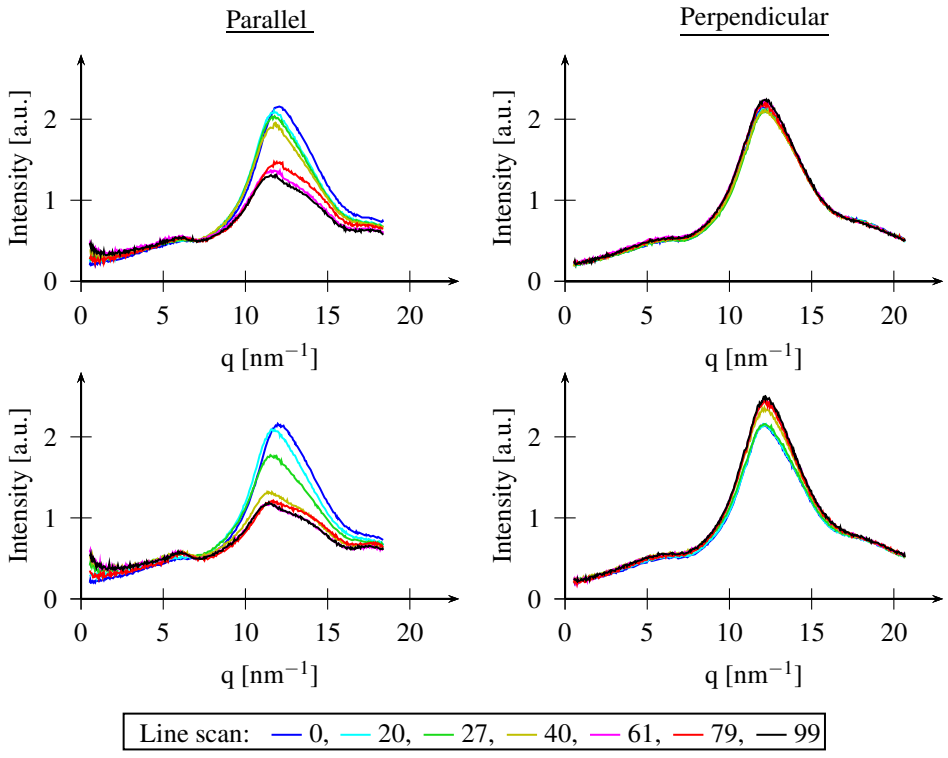

Figure 6: Radial plots from the two points on the specimen, parallel and perpendicular to the loading direction. The plots on top show data extracted from point B and the lower plots corresponds to point A on the specimen. Line scan 0 is the undeformed state.

During deformation the amplitude of the halo decreases strongly in the direction parallel to the loading while the intensity of the halo in the perpendicular direction increases slightly. This indicates a reorientation of the chains towards an alignment in the direction of load. The radial profiles in Figure 6 from the spatial point A show an earlier, and more pronounced decrease in intensity compared to point B.

The radial WAXS data, in a q-interval from 5.0 to 18 nm^{-1}, were fitted with a sum of five Gaussian functions, cf. Stoclet et al. (2011); Guo et al. (2015), where the fifth peak is

a broad background, i.e.,

$$I^{fit}(q) = \sum_{i}^{5} a_i \exp\left(-\frac{(q-b_i)^2}{2\sigma_i^2}\right), \tag{2}$$

where a_i are the amplitudes, b_i the positions and σ_i the standard deviations. An example of the result of the fitting procedure is shown in Figure 7. The fitting was made by minimising the function S using an interior point algorithm in the software Matlab®. S is defined as

$$S = \sum_{j=1}^{n} \left(\frac{I_j^{exp} - I_j^{fit}}{I_j^{exp}}\right)^2, \tag{3}$$

where n is the number of sampling points.

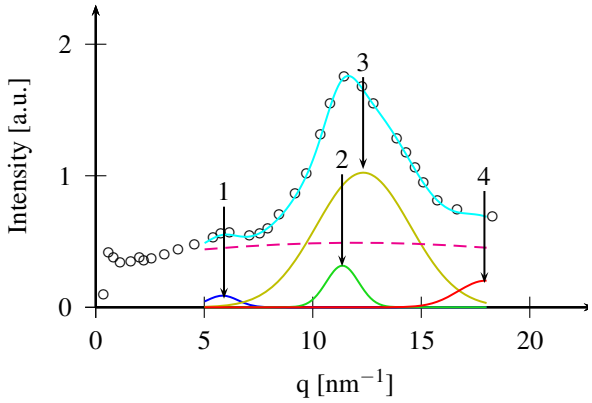

Figure 7: Profile analysis by fitting the sum (cyan line) of five Gaussian functions to the experimental data (open symbols). Dashed line is the background.

The position of the fitted peaks is used to calculate the deformation of the microstructure. The nanoscopic stretch related to peak number, i, is defined as

$$\lambda_i^{nano} = \frac{d_i}{d_{0_i}} = \frac{b_{0_i}}{b_i}, \tag{4}$$

where d_i is the microstructural spacing and b_i is the peak position obtained from the fitting and subscript 0 refers to the quantity in the undeformed state. Henceforth the nanoscopic stretch in the direction parallel and perpendicular to the direction of the macroscopic loading will be denoted $\lambda^{nano,\parallel}$ and $\lambda^{nano,\perp}$, respectively. The evolution of the nanoscopic stretch of the four fitted peaks as a function of loading (line scan) is presented in Figure 8.

The stretches from the first and third peaks in the direction parallel to the loading direction follow largely the same trend: an increase until line scan 20 (just before peak force), after which the stretches take a more or less constant value of about 4% and 2% for the first and third peak, respectively. After the macroscopic unloading, small stretches, in

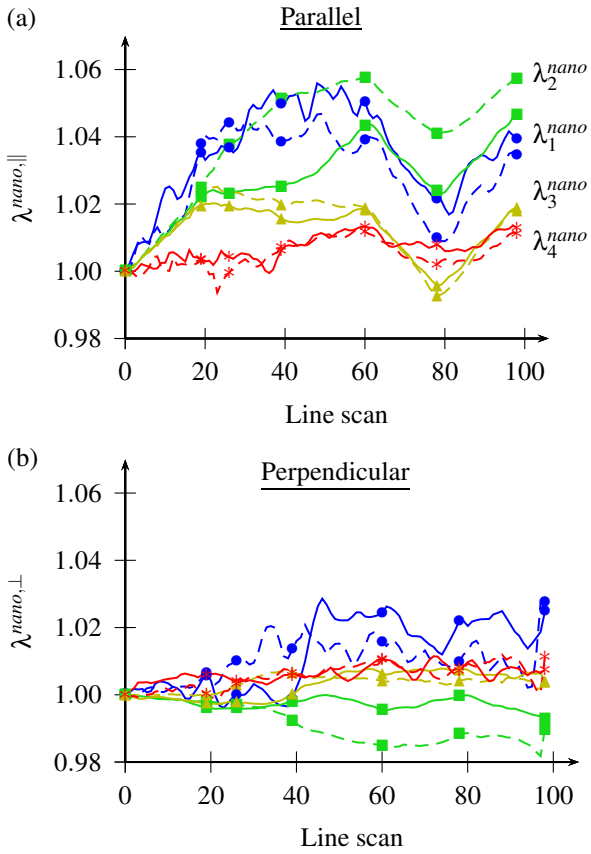

Figure 8: The nanoscopic stretch of the four fitted peaks: peak 1 (—●—), peak 2 (—■—), peak 3 (—▲—) and peak 4 (—✳—). The stretches are presented for two spatial points on the specimen, point A (dashed lines) and point B (solid lines).

tension for the first peak and in compression for the third peak, are present (see Figure 8a).

During the initial loading, until line scan 20, the stretch from the second peak, $\lambda_2^{nano,\parallel}$, follows the same trend as for the third peak. For point A (the centre point of the specimen), $\lambda_2^{nano,\parallel}$ continues to increase until line scan 40, after which the stretch rate is reduced. At point B, $\lambda_2^{nano,\parallel}$ reaches a plateau at line scan 20 before it increases monotonically until the macroscopic unloading after line scan 61. The stretch of the second peak decreases linearly during the macroscopic unload for both spatial points and after unload permanent stretches of 4% and 3% are observed for point A and B, respectively. For the fourth peak, the stretch increases slightly during loading and decreases during unloading. Even though the stretch of peak 4 is of some interest, the conclusions from this peak are restricted by the limited q-range during the WAXS measurements.

In the direction perpendicular to the macroscopic loading, the stretches seen in the fitted peaks are quite small, except for peak 1 (for both spatial positions); see Figure 8b. The oscillating stretch of peak 1 may be an artefact of the peak fitting, as this peak is not

well defined in the direction perpendicular to the loading (see the radial plots in Figure 6). However, there is a clear increase in $\lambda_1^{nano,\perp}$ as the localisation front passes through each of the two points. A more detailed analysis of this behaviour would however require better resolution in q of the X-ray data to be able to accurately trace the small changes in position of the peaks perpendicular to the loading.

The observation that the amorphous halo is formed from two peaks (peaks 2 and 3), indicates that the halo originates from two features with similar size in the undeformed state. During deformation, the size of these scatterers changes differently leading to two clearly visible peaks; see Figure 6. The nanoscopic stretch of peak 2 increases (with increasing macroscopic deformation) in the direction parallel to the macroscopic deformation while $\lambda_2^{nano,\perp}$ decreases; see Figure 8. This behaviour suggests that peak 2 is related to the distance between neighbouring chains, as the behaviour is consistent with chains oriented along the loading direction getting closer and chains oriented perpendicular becoming separated, when the specimen is stretched. The similar behaviour of the stretch of peaks 1 and 3 indicates that peak 3 is related to a correlation between closely positioned entities along a single chain, as peak 1 is related to correlation along the chain, cf. Eilhard et al. (1999); Mitchell and Windle (1985).

The similar behaviour of $\lambda_1^{nano,\parallel}$ and $\lambda_3^{nano,\parallel}$ can be observed clearly when plotting the nano-scopic stretch vs the major principal mesoscopic stretch from the DIC, Λ_I^{meso} (see Figure 9a). Besides showing the resemblance in behaviour of $\lambda_1^{nano,\parallel}$ and $\lambda_3^{nano,\parallel}$, Figure 9a also shows that the values of each of the two nanoscopic stretches are very much alike at the two spatial points on the specimen. The smaller values of $\lambda_3^{nano,\parallel}$ compared to $\lambda_1^{nano,\parallel}$ are expected since this is assumed to be related to the correlation between entities that are more closely positioned along the chain than the carbonate groups and hence has fewer atomic bonds in between.

The different behaviour of the $\lambda_2^{nano,\parallel}$ at the two points A and B, shown in Figures 8a and 9b, can be explained by an increase of this stretch when the thickness of the specimen is reduced, which occurs at different moments in the test for the two points. Macroscopically the passage of the localisation front includes a thickness reduction. As point A is located in between the two localisation bands, the specimen thickness is reduced at this point when the localisation is formed, explaining the larger value of $\lambda_2^{nano,\parallel}$. Returning to Figures 3 and 4 it is concluded that the localisation front passes through point B between line scan 40 and 60, or at Λ_I^{meso} value of between 1.4 and 1.5, which is consistent with the increase of $\lambda_2^{nano,\parallel}$ from point B (see Figure 9b).

Figure 9 clearly shows the non-affine relation between the deformation on the mesoscale and the deformation of the microstructure. $\lambda_1^{nano,\parallel}$ and $\lambda_3^{nano,\parallel}$ indicate that chain segments oriented along the loading direction stretch, due to the macroscopic load, until they reach maximum stretches of about 4% and 2%, respectively. This behaviour suggests that the chain segments start to slide past each other, after being stretched elastically to a limit stretch. The sliding of the chain segments is initiated simultaneously at the two points, point A and B, before the macroscopic force peak. As the sliding is initiated at a state of deformation with the same mesoscopic stretches at the two points (see Figure 3), before

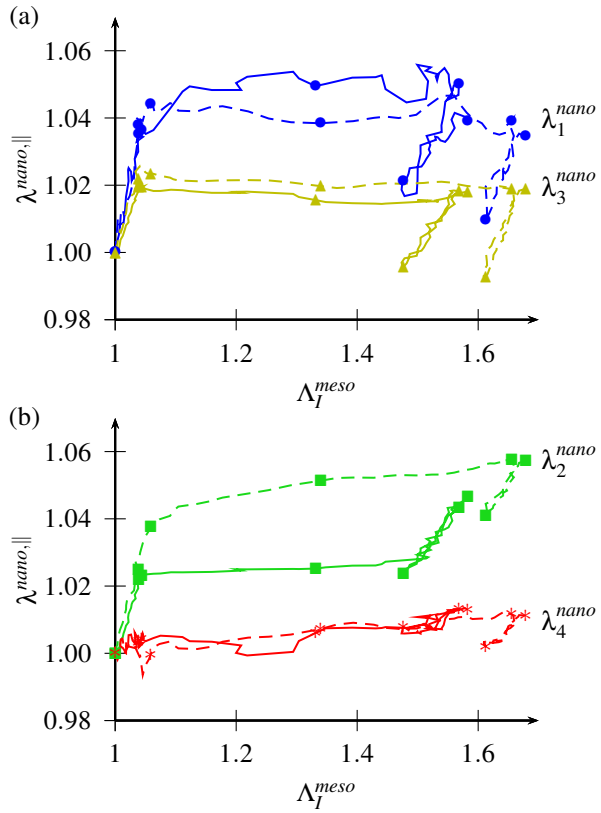

Figure 9: $\lambda^{nano,\parallel}$ vs Λ_I^{meso} for the two spatial point on the specimen (dashed lines point A and solid lines point B). (a) shows $\lambda_1^{nano,\parallel}$ (—●—) and $\lambda_3^{nano,\parallel}$ (—▲—). (b) shows $\lambda_2^{nano,\parallel}$ (—■—) and $\lambda_4^{nano,\parallel}$ (—✳—).

the localisation band is formed, the evolution of $\lambda_1^{nano,\parallel}$ and $\lambda_3^{nano,\parallel}$ from the two points is similar as the specimen is deformed further. When the macroscopic load is removed the chains appear to unload elastically, without any large permanent deformation. The stretches in Figure 9 also suggest that any observed permanent deformation at a molecular level is manly due to changes in the distance between neighbouring chains, i.e. in $\lambda_2^{nano,\parallel}$.

3.3.2 Azimuthal plots

To analyse the evolution of the anisotropy at the different microstructural distances, the fitting of the peaks identified in Figure 6 was made for radial profiles extracted in 72 different directions around the azimuth. This detailed procedure was performed due to the large overlapping area of the scattering peaks. The amplitude of the fitted peaks ($I(\varphi)$ vs φ, where φ is the azimuthal angle from 0 to 360° and $\varphi = 0$ is at the meridian) is shown in Figure 10 in polar coordinates for the same line scans presented earlier. To reduce noise from the peak fitting, the azimuthal profiles are filtered using a moving average filter before plotting. In the undeformed state all four peaks are isotropic. During deformation, peak

1 becomes strongly oriented parallel to the loading direction while peaks 2 and 3 become strongly oriented in the direction perpendicular to the loading. This is clearly seen in Figure 10. The anomaly in the polar plot for peak 4 at 45° is due to limited q-range of the detector in this direction.

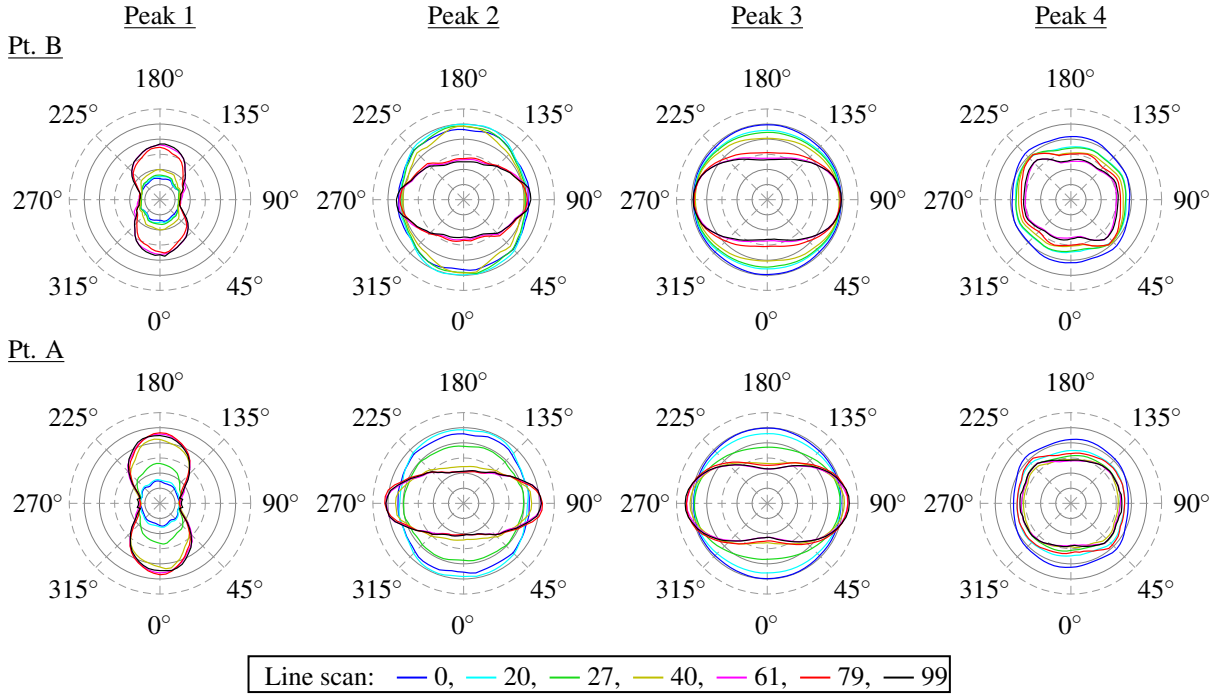

Figure 10: Azimuthal profiles of the fitted peaks from the points A and B on the specimen, plotted in polar coordinates. The plots on top show the amplitude of the peaks fitted to data extracted from point B on the specimen and the bottom plots show data from point A. The anomaly at 45° in peak 4 is due to the limited q-range of the detector in this direction. The loading direction is on the line 0-180 degrees. The intensity scale is arbitrary for the different peaks.

The degree of orientation, or anisotropy, for a specific peak i is quantified using the Hermans orientation parameter, cf. Roe (2000); Ran et al. (2002); Choi et al. (2012),

$$A_i^{nano} = \frac{3\left\langle \cos^2\phi \right\rangle_i - 1}{2}, \tag{5}$$

where

$$\left\langle \cos^2\phi \right\rangle_i = \frac{\int_0^{\pi/2} I_i(\phi)\cos^2\phi \sin\phi \mathrm{d}\phi}{\int_0^{\pi/2} I_i(\phi)\sin\phi \mathrm{d}\phi} \tag{6}$$

and ϕ is the azimuthal angle, being zero at the equator and $\pi/2$ at zenith (corresponding to $\varphi = 90$ and 180°). Hermans orientation parameter takes the values 0 for isotropy and

1, −0.5 for full orientation perpendicular and parallel to the loading direction, respectively. Figure 11 shows the evolution of the orientation parameter of the azimuthal trend corresponding to the four peaks identified in the radial plots.

The evolution of the anisotropy of peaks 1 and 3 (A_1^{nano} and A_3^{nano}) is similar, but with opposing sign, for each of the two considered spatial points. For point A, the evolution of the anisotropy of peaks 1 and 3 is as follows: (1) a small change until line scan 20; (2) a rapid decrease/increase (decrease for peak 1 and increase of peak 3) between line scan 20 and 40; (3) a slower decrease/increase until line scan 61; (4) a moderate change during unloading/reloading. The evolution of A_2^{nano} is similar to A_1^{nano}. Peak 4 becomes slightly oriented in the direction perpendicular to the loading. Significant permanent orientation of peaks 1, 2 and 3 is present after unloading; see Figure 11 line scan 79. Similar to the evolution of the third principal stretch, Λ_{III}^{meso}, the evolution of A^{nano} for peaks 1, 2 and 3 at point B is much like the evolution at the lower point, but slightly delayed. At point B the rapid change of A^{nano} of peaks 1, 2 and 3 begins at line scan 40 and continues until the unloading after line scan 61.

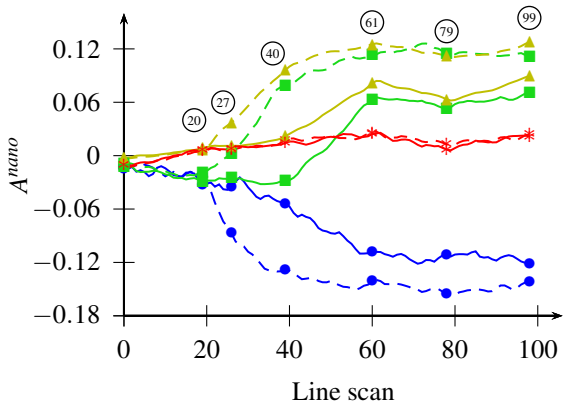

Figure 11: Hermans orientation parameter, A^{nano}, for the four fitted peaks seen in the radial plots in Figure 6: peak 1 (—●—), peak 2 (—■—), peak 3 (—▲—) and peak 4 (—✳—) at point A (dashed lines) and point B (solid lines).

It should be noted that the decrease of the orientation parameter of peak 1 is due to an increase of the intensity parallel to the loading direction while for peaks 2 and 3 the increase is due to a decrease of intensity parallel and a slight increase perpendicular to the loading; see Figure 10. For peak 4 the increase of the orientation parameter is due to a decrease of the intensity along the loading direction and not due to an increase of intensity perpendicular to the loading direction. This indicates: (1) a loss of order in the microstructure perpendicular to the loading related to peaks 2, 3 and 4 and increase of order for peak 1; (2) an increase of order parallel to the loading for peaks 2 and 3.

4 Conclusions

Using WAXS and DIC with *in-situ* uni-axial loading, the deformation of amorphous glassy polycarbonate has been measured simultaneously over a range of length-scales. This has revealed a non-affine relation between the observed deformation on the macro- and meso-scale and the deformation of the microstructure.

A first result from this work is that the WAXS measurements of *in-situ* loading, have revealed that the amorphous halo at $q = 12$ nm^{-1} (in the undeformed state) consists of two peaks (Figure 6). Previously, this halo has been seen as a single peak. In total four peaks have been identified in the studied q-range, which are attributed to: correlations between consecutive carbonate groups along the chain ($q = 6.2$ nm^{-1}, $d = 1.0$ nm); correlations between neighbouring chains ($q = 11.8$ nm^{-1}, $d = 0.53$ nm); correlations between closely positioned entities along the chain ($q = 12.7$ nm^{-1}, $d = 0.49$ nm); a mixture of inter- and intramolecular correlations ($q = 18$ nm^{-1}, $d = 0.35$ nm), cf. Lamers et al. (1992).

The characteristic force peak, seen in the macroscopic force-displacement curve (Figure 2), is preceded by the change in slope of the mesoscopic stretch (Λ_{III}^{meso}) from the DIC, at the centre point of the specimen (point A) (see Figure 4). At approximately the same line scan (line scan 20), the Hermans orientation parameters for WAXS peaks 1, 2 and 3 (from the same spatial point) show an increasing orientation of the microstructure, due to an increase of order of the chains in the direction of the loading and a loss of order between chains oriented perpendicular to the loading. The increase of Hermans orientation parameter of peak 2 (seen in Figure 11) suggests that the orientation of neighbouring chains is dominated by an alignment parallel to the loading direction, due to a loss of order of chains oriented perpendicular to the loading. The decrease of the orientation parameter of peak 1 indicates an alignment of the polymer chains parallel to the loading. Due to the deformation, peak 3 becomes aligned towards the direction perpendicular to the loading. This behaviour may be explained by conformational changes due to the deformation and the non-linear structure of the polycarbonate molecule; cf. Figure 12.

The local yield, identified as a rapid increase of Λ_I^{meso} in Figure 4, is preceded by the nanoscopic stretches $\lambda_1^{nano,\parallel}$ and $\lambda_3^{nano,\parallel}$ attaining a more or less constant value, see Figure 9. This indicates that the chains stretch until they reach a maximum elongation after which they start to slide past each other, leading to a non-recoverable reorganisation of the chains. The evolution of the anisotropy (A_1^{nano} and A_3^{nano}) shows that the reorganisation of the microstructure continues after $\lambda_1^{nano,\parallel}$ and $\lambda_3^{nano,\parallel}$ reach maximum values. This further supports that the yield at the studied length-scale is caused by activation of a permanent reorganisation of the microstructure.

After macroscopic unloading, the nanoscopic stretch curves determined from the WAXS peak shifts (Figure 9) show small permanent stretching within the polymer chains whilst there is significant permanent deformation between neighbouring chains. This suggests that the plastic deformation, at the considered microscopic level, is due to reorganisation of the chain network and not due to permanent deformation of the individual chains. The permanent deformation at the considered molecular level is however not of the order of the

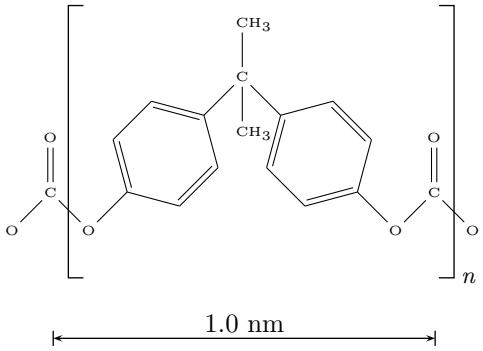

Figure 12: Sketch of a repeating unit of the polymer chain indicating the bent structure of the polycarbonate molecule. The distance between consecutive carbonate groups along the chain is indicated in the figure. A more detailed discussion of the molecule structure of PC is found in Červinka et al. (1991).

permanent deformation at the macro- or mesoscopic level.

In summary, novel observations on the deformation and reorientation of the microstructure and their relation to the meso- and macroscopic deformation have been presented herein. These observations provide new insights into the mechanisms of deformation in amorphous, glassy polymers and pave the way for development of enhanced constitutive models with a correct micro-mechanical basis and calibrated evolution of anisotropy.

Acknowledgement

The financial support from the Crafoord foundation, grant no. 20110521 and 20120632, is greatly acknowledged. We are also grateful for the beamtime and support received from the MAX IV Laboratory and the I911-SAXS beamline, proposal 20120327. The fruitful discussions with Johan Hektor during this work is gratefully acknowledged.

References

Arruda, E. M., Boyce, M. C., 1993. A three-dimensional constitutive model for the large stretch behavior of rubber elastic materials. Journal of the Mechanics and Physics of Solids 41 (2), 389–412.

Brown, E. N., Rae, P. J., Dattelbaum, D. M., Clausen, B., Brown, D. W., 2008. In-situ measurement of crystalline lattice strains in polytetrafluoroethylene. Experimental Mechanics 48 (1), 119–131.

Buisson, G., Ravi-Chandar, K., 1990. On the constitutive behaviour of polycarbonate under large deformation. Polymer 31 (11), 2071–2076.

Butler, M. F., Donald, A. M., 1998. A real-time simultaneous small-and wide-angle x-ray scattering study of in situ polyethylene deformation at elevated temperatures. Macromolecules 31 (18), 6234–6249.

Červinka, L., Fischer, E. W., Dettenmaier, M., 1991. On the linearization problem of the bent chain in amorphous polycarbonate. Polymer 32 (1), 12–18.

Červinka, L., Fischer, E. W., Hahn, K., Jiang, B. Z., Hellmann, G. P., Kuhn, K. J., 1987. On the intermolecular order in amorphous polycarbonate. neutron scattering results and model calculations. Polymer 28 (8), 1287–1292.

Choi, T., Fragiadakis, D., Roland, C. M., Runt, J., 2012. Microstructure and segmental dynamics of polyurea under uniaxial deformation. Macromolecules 45 (8), 3581–3589.

Del Val, J. J., Colmenero, J., Rosi, B., Mitchell, G. R., 1995. X-ray diffraction study of the influence of temperature on the structural correlations of poly (2-hydroxypropyl ether of bisphenol a). Polymer 36 (19), 3625–3631.

Eilhard, J., Zirkel, A., Tschöp, W., Hahn, O., Kremer, K., Schärpf, O., Richter, D., Buchenau, U., 1999. Spatial correlations in polycarbonates: Neutron scattering and simulation. The Journal of chemical physics 110 (3), 1819–1830.

Engqvist, J., Hall, S. A., Wallin, M., Ristinmaa, M., Plivelic, T. S., 2014. Multi-scale measurement of (amorphous) polymer deformation: Simultaneous x-ray scattering, digital image correlation and in-situ loading. Experimental Mechanics 54 (8), 1373–1383.

Farge, L., André, S., Meneau, F., Dillet, J., Cunat, C., 2013. A common multiscale feature of the deformation mechanisms of a semicrystalline polymer. Macromolecules 46 (24), 9659–9668.

Garcia, D., 2010. Robust smoothing of gridded data in one and higher dimensions with missing values. Computational statistics & data analysis 54 (4), 1167–1178.

Grytten, F., Daiyan, H., Polanco-Loria, M., Dumoulin, S., 2009. Use of digital image correlation to measure large-strain tensile properties of ductile thermoplastics. Polymer Testing 28 (6), 653–660.

Guo, H., Wang, J., Zhou, C., Zhang, W., Wang, Z., Xu, B., Li, J., Shang, Y., de Claville Christiansen, J., Yu, D., et al., 2015. Direct investigations of deformation and yield induced structure transitions in polyamide 6 below glass transition temperature with waxs and saxs. Polymer.

Harrysson, M., Ristinmaa, M., Wallin, M., Menzel, A., 2010. Framework for deformation induced anisotropy in glassy polymers. Acta Mechanica 211 (3-4), 195–213.

Lamers, C., Schärpf, O., Schweika, W., Batoulis, J., Sommer, K., Richter, D., 1992. Short range order in amorphous polycarbonates. Physica B: Condensed Matter 180, 515–518.

Lamers, C., Schönfeld, C., Shapiro, S. M., Batoulis, J., Timmermann, R., Cable, J. W., Richter, D., 1994. Short-range order effects in amorphous polycondensates as studied by spin polarized diffuse neutron scattering and simulation. Colloid and Polymer Science 272 (11), 1403–1419.

Lu, J., Ravi-Chandar, K., 1999. Inelastic deformation and localization in polycarbonate under tension. International journal of solids and structures 36 (3), 391–425.

Mark, J. E., 2007. Physical Properties of Polymers Handbook. Springer-Verlag New York.

Miehe, C., Göktepe, S., Mendez Diez, J., 2009. Finite viscoplasticity of amorphous glassy polymers in the logarithmic strain space. International Journal of Solids and Structures 46 (1), 181–202.

Mitchell, G. R., Windle, A. H., 1985. The effect of annealing on the local structure of glassy polycarbonate. Colloid and Polymer Science 263 (4), 280–285.

Poulain, X., Kohlman, L., Binienda, W., Roberts, G., Goldberg, R., Benzerga, A., 2013. Determination of the intrinsic behavior of polymers using digital image correlation combined with video-monitored testing. International Journal of Solids and Structures 50 (11), 1869–1878.

Ran, S., Wang, Z., Burger, C., Chu, B., Hsiao, B. S., 2002. Mesophase as the precursor for strain-induced crystallization in amorphous poly (ethylene terephthalate) film. Macromolecules 35 (27), 10102–10107.

Roe, R. J., 2000. Methods of X-ray and neutron scattering in polymer science. Vol. 739. Oxford University Press New York.

Schubach, H. R., Heise, B., 1986. Structure and anisotropy in polycarbonate. i. short range order of amorphous polycarbonate revealed by waxs. Colloid and Polymer Science 264 (4), 335–342.

Stoclet, G., Seguela, R., Lefebvre, J., Li, S., Vert, M., 2011. Thermal and strain-induced chain ordering in lactic acid stereocopolymers: influence of the composition in stereomers. Macromolecules 44 (12), 4961–4969.

Stoclet, G., Seguela, R., Vanmansart, C., Rochas, C., Lefebvre, J.-M., 2012. Waxs study of the structural reorganization of semi-crystalline polylactide under tensile drawing. Polymer 53 (2), 519–528.

Wang, M. C., Guth, E., 1952. Statistical theory of networks of non-gaussian flexible chains. The Journal of Chemical Physics 20, 1144.

Wang, Y., Jiang, Z., Fu, L., Lu, Y., Men, Y., 2014. Lamellar thickness and stretching temperature dependency of cavitation in semicrystalline polymers. Plos one 9 (5), 1–14.

Wu, P. D., van der Giessen, E., 1993. On improved network models for rubber elasticity and their applications to orientation hardening in glassy polymers. Journal of the Mechanics and Physics of Solids 41 (3), 427–456.

Yeh, F., Hsiao, B. S., Sauer, B. B., Michel, S., Siesler, H. W., 2003. In-situ studies of structure development during deformation of a segmented poly (urethane-urea) elastomer. Macromolecules 36 (6), 1940–1954.

Paper C

Jonas Engqvist, Mathias Wallin, Matti Ristinmaa,
Stephen A. Hall and Tomás S. Plivelic

Modelling multi-scale deformation of amorphous glassy polymers with experimentally motivated evolution of the microstructure

Submitted for international publication

Modelling multi-scale deformation of amorphous glassy polymers with experimentally motivated evolution of the microstructure

Jonas Engqvist[a], Mathias Wallin[a], Matti Ristinmaa[a], Stephen A. Hall[a,b] and Tomás S. Plivelic[c]

[a]Division of Solid Mechanics Lund University, Box 118, S-221 00 Lund, Sweden

[b]European Spallation Source AB, P.O. Box 176, 221 00, Lund, Sweden

[c]MAX IV Laboratory, Lund University, P.O. Box 118, 221 00, Lund, Sweden

Abstract

Recent multi-scale experiments have been used to develop a micro-mechanically motivated constitutive model for amorphous glassy polymers. Taking advantage of the experiments, the model makes use of a microstructural deformation gradient to incorporate the experimentally obtained deformation of the microstructure, as well as its evolving orientation. It is shown that this approach is able to predict accurately glassy polymer deformation over a wide range of length-scales, from the macroscopic response (mm range) down to the deformation of the microstructure (nm range). The proposed model is evaluated by comparing the numerical response to experimental results on multiple scales from an inhomogeneous cold drawing experiment of glassy polycarbonate. Besides the macroscopic force-displacement response, a qualitative comparison of the deformation field at the surface of the specimen is performed. Furthermore, the predicted evolution of the fabric orientation is compared to experimental results obtained from X-ray scattering experiments. The model shows very good agreement with the experimental data over a wide range of length scales.

1 Introduction

Due to favourable mechanical and manufacturing properties, glassy polymers are commonly used for containers or substitute for glass in the electronics and automotive industry. In such applications, glassy polymers are load carrying which implies that they risk being subjected to complex deformation phenomena, such as necking, deformation hardening and evolving anisotropy. The ability to accurately predict these phenomena is evidently of great importance when simulating the mechanical response of polymer structures. Many existing models are capable of capturing the global, macroscopic response of polymer structures in a satisfactory manner. However, the ability to predict the local, inhomogeneous deformation and the evolution of the microstructure in an experimentally motivated manner, which is of great importance, e.g., under multi-axial deformation, is lacking in these models.

Boyce et al. (1988) modelled polymer networks using a 3-chain network model with the chains aligned along the principal stretch axes. This approach is, however, unable to accurately distinguish between different modes of deformation. To this end, Arruda and Boyce (1991, 1993) reformulated the model using an eight-chain representation of the network, which better captures the macroscopic mechanical behaviour found experimentally. The eight-chain model is based on the assumption that a representative volume element consists of eight polymer chains oriented along the diagonals of a cubic unit cell. With this approach, the stretch will be the same in each of the eight chains and the chain stretch can be expressed in terms of the principal stretches. Wu and van der Giessen (1993) applied the so-called full-network model, that Treloar and Riding (1979) previously applied to rubber-like material under bi-axial deformation, to glassy polymers under general three-dimensional loading. The full-network model considers a large number of chains to mimic the polymer network using an orientation averaging involving a chain orientation distribution function (CODF). The approach of using a CODF was later used by Harrysson et al. (2010) in a model for non-affine deformation of polymer microstructure with evolving anisotropy. Anand and Gurtin (2003) developed a thermodynamically consistent model for amorphous polymers introducing an internal state variable representing the local free volume. Using this approach, Anand and Gurtin were able to improve the non-linear pre-peak behaviour displayed by many amorphous solids. The non-linear pre-peak behaviour have also been addressed by Benzerga an co-workers, e.g. Chowdhury et al. (2008); Kweon and Benzerga (2013). The approach of Anand and Gurtin (2003) was used to develop a thermo-mechanically coupled theory in Anand et al. (2009) and Ames et al. (2009). Miehe et al. (2009) formulated constitutive models in the logarithmic strain space using both the eight-chain network model and a non-affine micro-sphere model. By formulating the model using an additive split of the strain instead of the multiplicative split of the deformation gradient, Miehe et al. could avoid the problem of determining the plastic rotation. Common to these models is that they combine isotropic elasticity, viscous plastic flow, to model the segment motion in the polymer chains, and a strain hardening due to locking of the polymer chains. The experimental observations, motivating the assumptions regarding the deformation of the microstructure in these models are, however, limited.

Traditionally, the characterisation of the mechanical response of polymers has been addressed mainly by the macroscopic force-displacement (or equivalently stress-strain) curves from uni-axial or biaxial tensile and compression tests, e.g., G'sell and Jonas (1979); Boyce and Arruda (1990); Boyce et al. (1994); Dreistadt et al. (2009), or from multi-axial deformation tests, e.g., Ravi-Chandar and Ma (2000); Qvale and Ravi-Chandar (2004); Chakkarapani et al. (2006). The mechanical response can also be characterised using indentation tests from witch the macroscopic force-indentation depth response and/or the hardness is retrieved, e.g., van Melick et al. (2003); VanLandingham et al. (2005). The influence of the geometry of the indenter, the indentation rate and model parameters has been studied numerically by e.g. Tvergaard and Needleman (2011, 2012). As these approaches gives the macroscopic force-displacement response, they evidently lack the ability to take inhomogeneous deformation phenomena, such as necking in tension and barreling in compression, into account, as the local response differs from the macroscopic in the presence of inhomogeneous behaviour. To include inhomogeneous deformation in the characterisation, full-field measurement techniques must be used, e.g., Parsons et al. (2004); Poulain et al. (2013). With micro-mechanically based models, the need for more advanced experimental techniques that can probe the molecular structure of the material is crucial. Available techniques for studying the evolution of the microstructure of polymers include X-ray and neutron scattering, e.g. Schubach and Heise (1986); Rössle et al. (1989); Stoclet et al. (2010); Engqvist et al. (2014). Recent X-ray scattering experiments (cf. Engqvist et al. (2016)) have shown that plastic deformation of amorphous glassy polycarbonate (PC) is, at least partially, a result of reorganisation and reorientation of the polymer chain segments. In the experiments by Engqvist et al., PC specimen were loaded *in-situ* during wide angle X-ray scattering (WAXS) measurements with simultaneous full-field 3D-surface digital image correlation (DIC) measurements of the mesoscopic deformation of the specimen. Using this approach the deformation was measured simultaneously and locally over a wide range of length-scales from the macroscopic down to the deformation of the molecular structure, i.e. from the macro-scale to the nano-scale.

In this work, the evolution of the polymer network, revealed in the multi-scale experiments by Engqvist et al. (2016), is incorporated in a constitutive model for the mechanical behaviour of glassy polymers with finite elasto-viscoplastic deformation. The reorientation of the microstructure is modelled using a separate, microstructural deformation gradient. This approach was introduced by Wallin et al. (2003) and Wallin and Ristinmaa (2005) to describe the deformation of the microstructure of metals, i.e., the crystal lattice. In the present work, the polymer network is modelled using a large number of chains with evolving directions as proposed by Harrysson et al. (2010). Using the proposed approach, the local behaviour of the microstructure and the overall response are predicted accurately.

The paper is organised as follows. The experimental procedure is presented in Section 2 followed by the kinematic description of the continuum and the microstructure in Section 3. The steps that are taken for the model to fulfil the second law of thermodynamics is presented in Section 4. The specific model is presented in Section 5 followed by an evaluation of the model against experimental data in Section 6. The paper ends with concluding remarks in Section 7.

2 Experimental procedure

Cold drawing experiments with multi-scale deformation measurements were performed at the I911-SAXS beamline at the synchrotron MAX IV Laboratory (Lund University, Lund, Sweden), Labrador et al. (2013). The experiments involved continuous tensile loading of notched specimens of glassy polycarbonate (PC) at room temperature. During the experiments, deformation measurements were simultaneously performed at the surface of the specimen, using DIC, and at the bulk of the material on the molecular scale, using WAXS. The samples were loaded *in-situ* using a custom built tensile test machine with a constant macroscopic displacement rate of 0.01 mm/min. Figure 1 shows the experimental set-up inside the hutch of the beamline.

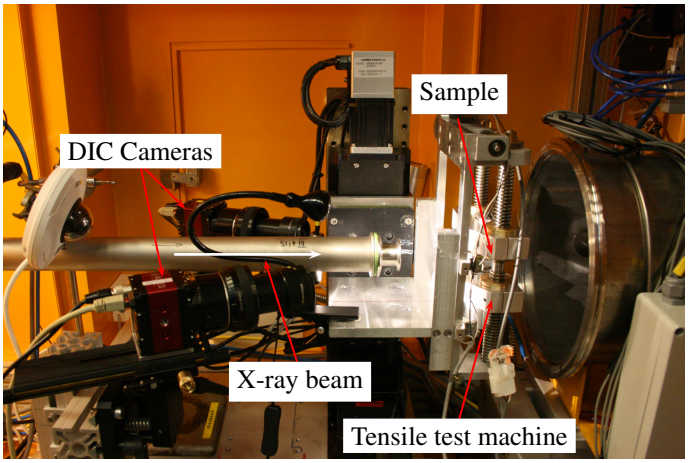

Figure 1: Experimental set-up inside the hutch of the beamline showing the X-ray beam path, the tensile test machine and the two DIC-cameras. The detector is placed downstream at 0.36 m from the sample position.

WAXS measurements, performed to investigate the evolution of the molecular structure of the specimen during deformation, were made using a wavelength, λ, of 0.91 Å and a sample-to-detector distance of 0.36 m resulting in a q-range of about 0.5 to 22 nm^{-1} (where $q = (4\pi/\lambda)\sin\theta$ and 2θ is the scattering angle). The scattering data were corrected for: the transmission of the X-rays (estimated using the direct beam intensity measured on the beamstop); the current specimen thickness (calculated from the DIC analysis); air scattering (by subtracting the background scattering). The scattering was mapped using line scans of 20 points, separated by 0.5 mm, along the centreline of the specimen with a beam of 500×500 $\mu\mathrm{m}^2$ to give local measurements.

Full-field 3D-surface DIC was used to measure the deformation at the surface of the specimen *in-situ*, simultaneously with WAXS. By using two digital cameras, calibrated for stereo-vision, the out-of-plane displacements as well as the in-plane displacements were measured. When calculating the current thickness of the specimens using the out-of-plane deformation (used to normalise the X-ray data), care was taken to remove rigid body

motion from the DIC data. The image correlation, from which the displacement fields were obtained, and the stereo-calibration were made using the commercial software Vic-3D (Correlated Solutions Inc.). A random speckle pattern was applied on the specimen to enable the correlation. The area where the X-ray beam hit the specimen was left unpainted to avoid scattering by the paint. This resulted in a blank area in the deformation fields, see Figure 7.

Using the method described above, the deformation was measured simultaneously over a wide range of length-scales during the deformation of the specimen. The experimental results indicate that the deformation on the molecular level is not of the same order of magnitude and do not follow the same evolution, as the macroscopic deformation. A permanent reorientation of the polymer chains is seen as the major source of permanent deformation on the molecular scale. The experimental results indicate that the reorientation of the chains is a result of the polymer chain segments being stretched to a limit stretch, after which they start to slide past each other. Furthermore, the results show that the polymer chain segments unload elastically with only a small residual deformation, when the macroscopic force is removed, i.e., the intra-chain deformation is predominately elastic. The result does, however, not exclude permanent deformation of the polymer chains due to change of conformation, e.g. by unravelling of the chains. Full details on the experimental procedure and results are found in Engqvist et al. (2014, 2016).

3 Kinematic description

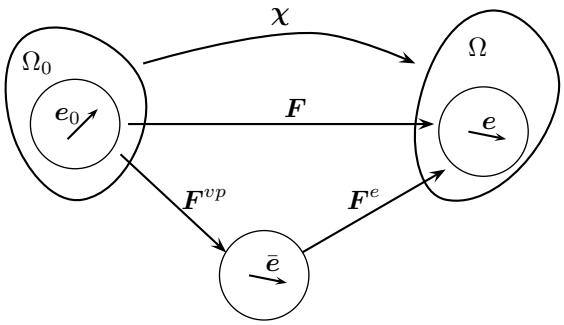

Figure 2: Illustration of the kinematic description of the microstructure and the continuum.

3.1 Kinematic description of the continuum

The motion of a body is described by the non-linear mapping $\boldsymbol{\chi}(\boldsymbol{X}, t)$ from the reference configuration $\Omega_0 \in \mathbb{R}^3$ at the time t_0 to the current configuration $\Omega \in \mathbb{R}^3$ at the time $t > t_0$, where $\boldsymbol{X}$ denotes the position of a material particle in the reference configuration, see Figure 2. The position of a material particle in the current configuration is $\boldsymbol{x} = \boldsymbol{\chi}(\boldsymbol{X}, t)$

and the deformation of the body is provided by the deformation gradient $\boldsymbol{F}$, mapping line segments from Ω_0 to Ω with $J = \det(\boldsymbol{F}) > 0$. To model elasto-viscoplasticity a multiplicative split of the deformation gradient into an elastic and a viscoplastic part is assumed, i.e.,

$$\boldsymbol{F} = \boldsymbol{F}^e \boldsymbol{F}^{vp}, \tag{1}$$

where $\boldsymbol{F}^e$ and $\boldsymbol{F}^{vp}$ defines the elastic and the viscoplastic deformation, respectively. The multiplicative split (1) introduces a stress free intermediate configuration, cf. Figure 2. Using the polar decomposition, the elastic and viscoplastic deformation gradients in (1) can be decomposed into

$$\boldsymbol{F}^e = \boldsymbol{V}^e \boldsymbol{R}^e \quad \text{and} \quad \boldsymbol{F}^{vp} = \boldsymbol{V}^{vp} \boldsymbol{R}^{vp}, \tag{2}$$

where $\boldsymbol{R}^e$ and $\boldsymbol{R}^{vp}$ are the orthogonal elastic and viscoplastic rotation tensors and $\boldsymbol{V}^e$ and $\boldsymbol{V}^{vp}$ are the symmetric, positive definite, left elastic and viscoplastic stretch tensors. Later, the elastic rotation tensor will be assumed to be equal to unity, i.e. $\boldsymbol{R}^e = \boldsymbol{1}$ following Boyce et al. (1988), which leads to a symmetric elastic deformation gradient, $\boldsymbol{F}^e = \boldsymbol{F}^{eT}$. The spatial velocity gradient is defined as

$$\boldsymbol{l} = \dot{\boldsymbol{F}} \boldsymbol{F}^{-1}, \tag{3}$$

where a superposed dot denotes the material time derivative. The spatial velocity gradient can be additively split into symmetric and skew-symmetric parts as

$$\boldsymbol{l} = \boldsymbol{d} + \boldsymbol{w}, \tag{4}$$

where $\boldsymbol{d}$ is the symmetric spatial rate of deformation tensor and $\boldsymbol{w}$ is the skew-symmetric spatial spin tensor. Making use of (1), the spatial velocity gradient can be decomposed as

$$\boldsymbol{l} = \boldsymbol{l}^e + \boldsymbol{l}^{vp} = \boldsymbol{l}^e + \boldsymbol{F}^e \boldsymbol{L}^{vp} \boldsymbol{F}^{e-1}, \tag{5}$$

where the elastic and viscoplastic velocity gradients are defined as

$$\boldsymbol{l}^e = \dot{\boldsymbol{F}}^e \boldsymbol{F}^{e-1} \quad \text{and} \quad \boldsymbol{L}^{vp} = \dot{\boldsymbol{F}}^{vp} \boldsymbol{F}^{vp-1}, \tag{6}$$

respectively. For later purposes the viscoplastic velocity gradient is additively decomposed as

$$\boldsymbol{L}^{vp} = \boldsymbol{D}^{vp} + \boldsymbol{W}^{vp}, \tag{7}$$

where $\boldsymbol{D}^{vp}$ is the symmetric viscoplastic rate of deformation tensor and $\boldsymbol{W}^{vp}$ is the skew-symmetric viscoplastic spin tensor. In the same manner as (7), the spatial form of the viscoplastic velocity gradient, $\boldsymbol{l}^{vp} = \boldsymbol{F}^e \boldsymbol{L}^{vp} \boldsymbol{F}^{e-1}$, can be additively split as $\boldsymbol{l}^{vp} = \boldsymbol{d}^{vp} + \boldsymbol{w}^{vp}$. The symmetric part of the spatial velocity gradient, $\boldsymbol{d}^{vp}$, is obtained by performing a push-forward of $\boldsymbol{D}^{vp}$ to the current configuration using $\boldsymbol{F}^e$, i.e.

$$\boldsymbol{d}^{vp} = \boldsymbol{F}^e \boldsymbol{D}^{vp} \boldsymbol{F}^{e-1}. \tag{8}$$

Moreover, the right Cauchy-Green and the elastic right Cauchy-Green deformation tensors are defined as

$$\boldsymbol{C} = \boldsymbol{F}^T\boldsymbol{F} \quad \text{and} \quad \boldsymbol{C}^e = \boldsymbol{F}^{eT}\boldsymbol{F}^e, \tag{9}$$

respectively. Taking the material time derivative of $\boldsymbol{C}$ and making use of (3) and (5) leads to

$$\boldsymbol{F}^{vp-T}\dot{\boldsymbol{C}}\boldsymbol{F}^{vp-1} = \dot{\boldsymbol{C}}^e + \dot{\hat{\boldsymbol{C}}}^{vp}, \tag{10}$$

where

$$\dot{\hat{\boldsymbol{C}}}^{vp} = 2\text{sym}[\boldsymbol{C}^e\boldsymbol{L}^{vp}], \tag{11}$$

where $\text{sym}[\cdot] = \frac{1}{2}([\cdot] + [\cdot]^T)$ denotes the symmetric part of the tensor.

3.2 Kinematic description of the microstructure

Based on the results from the X-ray scattering experiments by Engqvist et al. (2016), which indicate that the deformation of the molecular network differs from the macroscopic deformation, it is assumed that the viscoplastic part of the deformation of the microstructure can be described by a microstructural deformation gradient, denoted here as $\bar{\boldsymbol{F}}$. $\bar{\boldsymbol{F}}$ maps vectors related to the microstructure from the undeformed to the intermediate configuration following Wallin et al. (2003) and Wallin and Ristinmaa (2005). The evolution of $\bar{\boldsymbol{F}}$ is assumed to be governed by

$$\dot{\bar{\boldsymbol{F}}} = \bar{\boldsymbol{l}}\bar{\boldsymbol{F}}, \tag{12}$$

where $\bar{\boldsymbol{l}}$ is the microstructural velocity gradient. Similar to (7), the microstructural velocity gradient is split into a symmetric and a skew-symmetric part, i.e. $\bar{\boldsymbol{l}} = \bar{\boldsymbol{d}} + \bar{\boldsymbol{w}}$. Subsequently $\bar{\boldsymbol{d}}$ and $\bar{\boldsymbol{w}}$ will be chosen as $\bar{\boldsymbol{d}} = \eta\boldsymbol{D}^{vp}$ and the spin tensor $\bar{\boldsymbol{w}} = \boldsymbol{W}^{vp}$, cf. Dafalias (2001). Thus, the microstructural velocity gradient is postulated as

$$\bar{\boldsymbol{l}} = \dot{\bar{\boldsymbol{F}}}\bar{\boldsymbol{F}}^{-1} = \eta\boldsymbol{D}^{vp} + \boldsymbol{W}^{vp}. \tag{13}$$

The coefficient η in (13) is a constitutive parameter, associated with the deformation of the microstructure. η is introduced to be able to include the difference in the deformation levels on the macroscopic and microscopic scale, as motivated by the experimental data of Engqvist et al. (2016). As a special case, if $\eta = 1.0$ the microstructural deformation follows the viscoplastic part of the macroscopic deformation, other values of η results in a deformation of the microstructure that differs from the macroscopic since $\bar{\boldsymbol{l}}$ will differ from $\boldsymbol{L}^{vp}$. In the same manner as for the continuum, the right Cauchy-Green tensor $\bar{\boldsymbol{C}}$ and the Finger tensor $\bar{\boldsymbol{b}}$ associated with the deformation of the microstructure are defined as

$$\bar{\boldsymbol{C}} = \bar{\boldsymbol{F}}^T\bar{\boldsymbol{F}} \quad \text{and} \quad \bar{\boldsymbol{b}} = \bar{\boldsymbol{F}}\bar{\boldsymbol{F}}^T, \tag{14}$$

respectively. Time differentiation of the Cauchy-Green deformation tensor associated with the microstructural deformation provides

$$\dot{\bar{\boldsymbol{C}}} = 2\bar{\boldsymbol{F}}^T\text{sym}[\bar{\boldsymbol{l}}]\bar{\boldsymbol{F}}, \tag{15}$$

which will be useful later on. To include the rotation of the microstructure observed in the experiment, a set of unit vectors, $\bar{\boldsymbol{e}}$, describing the microstructural orientation is introduced and obtained by mapping the vector $\boldsymbol{e}_0$ from the reference configuration using the microstructural deformation gradient, $\bar{\boldsymbol{F}}$, i.e.,

$$\bar{\boldsymbol{e}} = \frac{\bar{\boldsymbol{F}}\boldsymbol{e}_0}{\|\bar{\boldsymbol{F}}\boldsymbol{e}_0\|}. \tag{16}$$

Evidently, $\bar{\boldsymbol{e}}$ is a unit vector in the intermediate configuration, see Figure 2. The permanent reorientation of the microstructure achieved through (16) is motivated by the experiment of Engqvist et al. (2016), in which a clear permanent reorientation of the chain segments, due to macroscopic deformation, is observed.

4 Thermodynamical basis

The second law of thermodynamics, which should be fulfilled for a physically sound model, can be reformulated as the dissipation inequality. For simplicity, isothermal conditions will be assumed throughout this paper. Expressed in terms of the Kirchhoff stress tensor, $\boldsymbol{\tau}$, and the rate of deformation tensor, $\boldsymbol{d}$, the dissipation inequality takes the following form

$$\mathcal{D} = \boldsymbol{\tau} : \boldsymbol{d} - \dot{\psi} \geq 0, \tag{17}$$

where ψ is the Helmholtz free energy per unit volume in the reference configuration. It is assumed that the Helmholtz free energy can be divided into an elastic part, ψ^e, described through $\boldsymbol{C}^e$ and an inelastic part, ψ^{ie}, described through $\bar{\boldsymbol{C}}$, i.e.,

$$\psi(\boldsymbol{C}^e, \bar{\boldsymbol{C}}) = \psi^e(\boldsymbol{C}^e) + \psi^{ie}(\bar{\boldsymbol{C}}). \tag{18}$$

Inserting (18) into the dissipation inequality (17) and utilising the arguments of Coleman and Gurtin (1967) together with (10) and $\dot{\boldsymbol{C}} = 2\boldsymbol{F}^T\boldsymbol{d}\boldsymbol{F}$, the dissipation inequality can be rewritten as

$$\mathcal{D} = \frac{\partial \psi^e}{\partial \boldsymbol{C}^e} : \dot{\bar{\boldsymbol{C}}}^{vp} - \frac{\partial \psi^{ie}}{\partial \bar{\boldsymbol{C}}} : \dot{\bar{\boldsymbol{C}}} \geq 0 \tag{19}$$

and the Kirchhoff stress tensor, $\boldsymbol{\tau}$, can be expressed as

$$\boldsymbol{\tau} = 2\boldsymbol{F}^e \frac{\partial \psi^e}{\partial \boldsymbol{C}^e} \boldsymbol{F}^{eT}. \tag{20}$$

Using (20) together with (8), (11), the evolution law (13) and (15), the dissipation inequality (19) is reduced to

$$\mathcal{D} = (\boldsymbol{\Sigma} - \boldsymbol{B}) : \boldsymbol{D}^{vp} \geq 0, \tag{21}$$

where $\boldsymbol{\Sigma}$ is the Mandel stress defined as $\boldsymbol{\Sigma} = \boldsymbol{F}^{eT}\boldsymbol{\tau}\boldsymbol{F}^{e-T}$ and $\boldsymbol{B}$ is referred to as the back-stress defined as

$$\boldsymbol{B} = 2\eta \bar{\boldsymbol{F}} \frac{\partial \psi^{ie}}{\partial \bar{\boldsymbol{C}}} \bar{\boldsymbol{F}}^T. \tag{22}$$

Since ψ^e is an isotropic function in $\boldsymbol{C}^e$, it can be shown that the Mandel stress tensor is symmetric and corresponds to a rotation of the Kirchhoff stress, i.e. $\boldsymbol{\Sigma} = \boldsymbol{R}^{eT}\boldsymbol{\tau}\boldsymbol{R}^e$. Finally, it is noted that since, $\boldsymbol{R}^e = \boldsymbol{1}$, the dissipation inequality (21) can be written as

$$\mathcal{D} = (\boldsymbol{\tau} - \boldsymbol{B}) : \boldsymbol{D}^{vp} \geq 0. \tag{23}$$

Next, the specific model will be discussed.

5 Specific model

5.1 The elastic free energy

In the present model, elastic anisotropy is neglected and the elastic part of the free energy, ψ^e, is chosen as

$$\psi^e = \frac{1}{2}K(I_1^e)^2 + 2GJ_2^e, \tag{24}$$

where K and G are the bulk and shear modulus, respectively. The invariants in (24) are defined as

$$I_1^e = \mathrm{tr}[\ln \boldsymbol{V}^e] \;\text{ and }\; J_2^e = \frac{1}{2}(\ln \boldsymbol{V}^e)^{\mathrm{dev}} : (\ln \boldsymbol{V}^e)^{\mathrm{dev}}. \tag{25}$$

These invariants are related to the volumetric and isochoric part of the deformation, respectively. The superscript *dev* denotes the deviatoric tensor defined as $[\cdot]^{\mathrm{dev}} = [\cdot] - \frac{1}{3}\mathrm{tr}[\cdot]\boldsymbol{I}$ where $\mathrm{tr}[\cdot]$ is the trace of the tensor. Using (20) and (24) the Kirchhoff stress, $\boldsymbol{\tau}$, is given as

$$\boldsymbol{\tau} = KI_1^e\boldsymbol{1} + 2G(\ln \boldsymbol{V}^e)^{\mathrm{dev}}. \tag{26}$$

5.2 The plastic free energy

The polymer network is assumed to consist of n number of ideal chains per unit volume, each of which is built up by N rigid segments of equal length l. Using non-Gaussian chain statistics, the Helmholtz free energy for a single ideal polymer chain at a constant absolute temperature, θ, is described by

$$\psi_{chain} = kN\theta\left(\lambda_r\mathcal{L}^{-1}(\lambda_r) + \ln\frac{\mathcal{L}^{-1}(\lambda_r)}{\sinh\mathcal{L}^{-1}(\lambda_r)}\right) - \psi_0, \tag{27}$$

cf. Treloar (1975); Wu and van der Giessen (1993); Miehe et al. (2009), where

$$\lambda_r = \frac{\lambda^{NW}}{\sqrt{N}} \tag{28}$$

is the relative network stretch, λ^{NW} is the network stretch, $\sqrt{N}$ is the limit stretch of a chain, k is Boltzmann's constant, ψ_0 is an arbitrary constant and $\mathcal{L}^{-1}$ is the inverse of

the Langevin function defined by $\mathcal{L}[\cdot] = \coth[\cdot] - 1/[\cdot]$. The total inelastic free energy is assumed to be given as

$$\psi^{ie} = n\psi_{chain}. \tag{29}$$

Using (27), (28), (29) and making use of the chain rule, the backstress (22) can be calculated as

$$\boldsymbol{B} = 2\eta\bar{\boldsymbol{F}}\frac{\partial(n\psi_{chain})}{\partial\lambda^{NW}}\frac{\partial\lambda^{NW}}{\partial\bar{\boldsymbol{C}}}\bar{\boldsymbol{F}}^T = 2\eta C_R\sqrt{N}\mathcal{L}^{-1}(\lambda_r)\bar{\boldsymbol{F}}\frac{\partial\lambda^{NW}}{\partial\bar{\boldsymbol{C}}}\bar{\boldsymbol{F}}^T, \tag{30}$$

where $C_R = nk\theta$ is a constitutive parameter known as the rubber modulus. In the microsphere model by Miehe et al. (2004), a stretch fluctuation field acting on the chain stretch, was introduced to multiplicatively links the chain stretch to the network stretch. The fluctuation field is assumed to be constrained by the condition that the average chain stretch is equal to the average network stretch in terms of the m-root average. This yields a closed form for the network stretch, λ^{NW}, calculated as an average of the chain stretches, $\bar{\lambda}$, using the m-root average operator, i.e.,

$$\lambda^{NW} = \sqrt[m]{\left\langle(\bar{\lambda})^m\right\rangle}, \tag{31}$$

cf. Miehe et al. (2004). Choosing the parameter m to be equal to $m = 2$, which will be the case in this study, leads to an affine relation between $\bar{\lambda}$ and λ^{NW}. The orientation average, or homogenisation, of any quantity $[\cdot]$ is given by

$$\langle[\cdot]\rangle = \frac{1}{4\pi}\int_{\mathbb{U}^2}[\cdot]\mathrm{d}A, \tag{32}$$

where $\mathbb{U}^2$ represents the unit sphere. The stretch $\bar{\lambda}$, in the direction of the microstructural unit vector $\bar{\boldsymbol{e}}$, is denoted as the chain stretch which is related to the change of the end-to-end distance of a polymer chain. The chain stretch is chosen as

$$\bar{\lambda} = \sqrt{\bar{\boldsymbol{e}}\cdot\bar{\boldsymbol{b}}\bar{\boldsymbol{e}}}. \tag{33}$$

Using the stretch expressions (31) and (33) together with (30) leads to the following expression for the backstress (30),

$$\boldsymbol{B} = \eta C_R\sqrt{N}\mathcal{L}^{-1}(\lambda_r)\left(\lambda^{NW}\right)^{1-m}\bar{\boldsymbol{F}}\left\langle\left(\bar{\lambda}\right)^{m-2}\left[\frac{2\mathrm{sym}[\boldsymbol{m}_0\bar{\boldsymbol{C}}]}{\|\bar{\boldsymbol{F}}\boldsymbol{e}_0\|} - (\bar{\lambda})^2\boldsymbol{m}_0\right]\right\rangle\bar{\boldsymbol{F}}^T, \tag{34}$$

with $\boldsymbol{m}_0 = \boldsymbol{e}_0\otimes\boldsymbol{e}_0$ where $\otimes$ denote the dyadic product.

5.3 Viscoplastic flow and strain hardening

The macroscopic viscoplastic part of the rate of deformation is given by

$$\boldsymbol{D}^{vp} = \dot{\gamma}^{vp}\boldsymbol{N}, \tag{35}$$

where $\dot{\gamma}^{vp}$ is the plastic shear strain rate and the flow direction $\boldsymbol{N}$ is assumed to be aligned with the driving stress $\tilde{\boldsymbol{\tau}}$, i.e.,

$$\boldsymbol{N} = \frac{1}{\sqrt{2}\tau}\tilde{\boldsymbol{\tau}}^{\mathrm{dev}}, \quad \tau = \sqrt{\frac{1}{2}\tilde{\boldsymbol{\tau}}^{\mathrm{dev}} : \tilde{\boldsymbol{\tau}}^{\mathrm{dev}}}. \tag{36}$$

The driving stress, $\tilde{\boldsymbol{\tau}}$, is defined as

$$\tilde{\boldsymbol{\tau}}^{\mathrm{dev}} = \boldsymbol{\tau}^{\mathrm{dev}} - \boldsymbol{B}^{\mathrm{dev}}. \tag{37}$$

The plastic shear strain rate $\dot{\gamma}^{vp}$ is taken as

$$\dot{\gamma}^{vp} = \dot{\gamma}_0 \exp\left[-\frac{A s_s}{\theta}\left(1 - \left(\frac{\tau}{s_s}\right)^{5/6}\right)\right], \quad s_s = s + \alpha p, \tag{38}$$

as proposed by Argon (1973), where $\dot{\gamma}_0$ and A are model parameters, τ is the equivalent stress defined in (36), $p = -\frac{1}{3}\mathrm{tr}(\boldsymbol{\sigma})$ is the pressure, $\boldsymbol{\sigma} = \frac{1}{J}\boldsymbol{\tau}$ is the Cauchy stress, $J = \det(\boldsymbol{F})$ and α is the pressure dependence factor. Boyce et al. (1988) proposed an evolution of the athermal shear stress, $\dot{s}$, to incorporate the stress softening behaviour of glassy polymers. The expression for the athermal shear stress is $s = s_1 + s_2$ and the evolution laws of the hardening parameters are

$$\begin{aligned} \dot{s}_1 &= h_1\left(1 - \frac{s_1}{s_{ss}}\right)\dot{\gamma}^{vp}, \quad s_1(0) = s_0, \\ \dot{s}_2 &= h_2\dot{\gamma}^{vp}, \quad s_2(0) = 0, \end{aligned} \tag{39}$$

where h_1, h_2, s_0 and s_{ss} are model parameters. In (39), s_1 is the athermal shear stress from the original model while s_2 was introduced by Holopainen and Wallin (2013) to overcome the problem of over-predicting the Bauchinger effect on unloading as shown by Dreistadt et al. (2009).

6 Model evaluation

In this section, the capacity of the developed model is investigated by simulating the mechanical response of glassy polycarbonate (PC). The model is calibrated to uni-axial and plane strain compression experiments with assumed homogeneous deformation. After this, the calibrated model is compared to a full-scale inhomogeneous deformation experiment. For this purpose, the model was implemented as a user-defined material model (UMAT) in the commercial software Abaqus®/Standard.

Details about the numerical treatment of the orientation average in (32) is presented in A. In the numerical implementation, the inverse Langevin function in (34) is evaluated using the Padé approximation proposed by Cohen (1991), i.e. $\mathcal{L}^{-1}(x) \approx x(3-x^2)/(1-x^2)$. The algorithmic treatment of the model is discussed in B.

6.1 Homogeneous deformation

For the calibration, a fixed Cartesian coordinate system was introduced by the orthonormal basis vectors $\boldsymbol{E}_x$, $\boldsymbol{E}_y$ and $\boldsymbol{E}_z$. For uni-axial and plane strain conditions the deformation can be characterised by the deformation gradient

$$\boldsymbol{F} = \lambda_x \boldsymbol{E}_x \otimes \boldsymbol{E}_x + \lambda_y \boldsymbol{E}_y \otimes \boldsymbol{E}_y + \lambda_z \boldsymbol{E}_z \otimes \boldsymbol{E}_z. \tag{40}$$

The uni-axial deformation was achieved by deformation controlled loading in the $\boldsymbol{E}_z$ direction, while the unknown stretches, $\lambda_x = \lambda_y$, ensure that the constraint on the Cauchy stress components, $\sigma_x = \sigma_y = 0$, was satisfied. Plane strain compression was achieved by loading in the $\boldsymbol{E}_z$ direction and simultaneously preventing deformation in the $\boldsymbol{E}_y$ direction, i.e., $\lambda_y = 1$. As for the uni-axial deformation, the extra unknown, λ_x, was solved to satisfy $\sigma_x = 0$.

Uni-axial and plane strain compression data of PC were taken from Ames et al. (2009) and Boyce et al. (1994), respectively. Both sets of tests were performed at room temperature using a constant strain rate of $|\overline{\ln \dot{\lambda}_z}| = 10^{-2}$ s^{-1}. During the calibration, the elastic parameters, Young's modulus and Poisson's ratio were kept fixed as $E = 2300$ MPa and $\nu = 0.3$, respectively. The values of the elastic parameters were taken to coincide with those found in Boyce et al. (1994). Furthermore, the parameter m in (31) was kept fixed at $m = 2$. To investigate the influence of the coefficient η, the calibration was performed using different values of this parameter. The constitutive parameters, obtained using a least-squares fitting, are shown in Table 1.

Table 1: Constitutive parameters obtained by calibrating the model to data for uni-axial compression by Ames et al. (2009) and plane strain compression by Boyce et al. (1994).

η	s_0	s_{ss}	h_1	h_2	$\dot{\gamma}_0$	A	C_R	N	α
-	MPa	MPa	MPa	MPa	s^{-1}	MPa^{-1}K	MPa	-	-
0.25	70.2	35.8	156	26.1	$4.51{\cdot}10^{10}$	342	42.1	1.30	0.08
0.50	70.2	36.5	155	27.0	$4.51{\cdot}10^{10}$	342	16.1	1.80	0.08
0.75	70.2	37.2	156	29.0	$4.51{\cdot}10^{10}$	342	7.50	2.41	0.08
1.0	70.2	36.3	154	39.3	$4.51{\cdot}10^{10}$	342	2.87	3.18	0.08

The macroscopic stress-strain curves from the calibration are presented in Figure 3. From these curves it is clear that the proposed model is able to capture the macroscopic response, regardless the value of η, within the studied range. To fully characterise the material it is, however, insufficient to only study macroscopic curves and more advanced experimental techniques must be employed. Next, the proposed model will be evaluated by comparison to experimental data from WAXS and full-field deformation measurements from DIC.

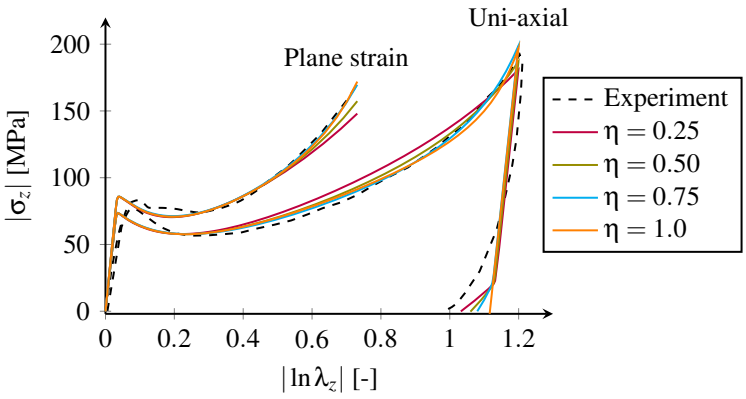

Figure 3: Stess-strain response for uni-axial and plane strain compression. The solid lines represent the simulated response, fitted to the experimental data using four values of η. The dashed lines show experimental data for uni-axial compression by Ames et al. (2009) and plane strain compression by Boyce et al. (1994).

6.2 Inhomogeneous deformation

To further evaluate the predictive capacity of the developed model, a three-dimensional cold drawing experiment of a notched polycarbonate (PC) tensile specimen, as discussed in Section 2, was simulated. The geometry of the tensile specimen is shown in Figure 4. The specimen was subjected to a displacement controlled elongation by a displacement, u, of the top and bottom surfaces whereas the other surfaces were traction free; see Figure 4. A constant displacement rate of $\dot{u} = 5 \cdot 10^{-3}$ mm/min was used during loading and unloading. The final displacement before unload was $2u = 3.35$ mm. Due to symmetry, only an eighth of the geometry was taken into consideration during the simulation. The analysed part of the geometry was discretised using a finite element mesh consisting of 27 062 eight node C3D8 brick elements, see Figure 4.

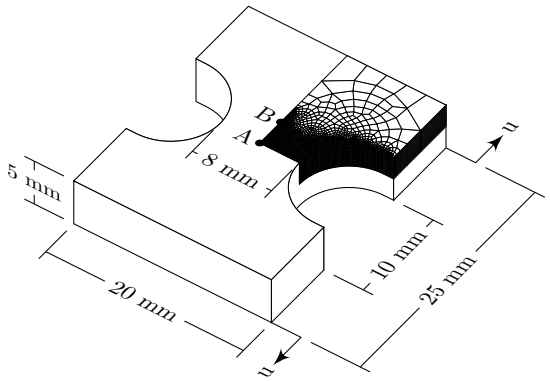

Figure 4: Undeformed geometry and finite element mesh of the analysed structure.

The ability of the proposed model to capture local inhomogeneous deformation phe-

nomena is investigated by comparing contour plots of the major principal stretch, λ_1, from the model with those measured using DIC, λ_1^{DIC}. Since the DIC measures the deformation at the surface of the specimen, an assumption on the gradient of the out-of-plane displacement is needed. Engqvist et al. (2016) assumed that the deformation is homogeneous through the thickness of the specimen. Using this assumption, the deformation gradient can be written as

$$\boldsymbol{F}^{DIC} = \begin{bmatrix} 1+\frac{\partial u}{\partial X} & \frac{\partial u}{\partial Y} & 0 \\ \frac{\partial v}{\partial X} & 1+\frac{\partial v}{\partial Y} & 0 \\ \frac{\partial w}{\partial X} & \frac{\partial w}{\partial Y} & 1+\frac{2w}{t_0} \end{bmatrix} \tag{41}$$

in a fixed Cartesian coordinate system, where u, v and w are the displacements measured by DIC at the surface and t_0 is the thickness of the undeformed specimen in the $\boldsymbol{E}_z$, out-of-plane, direction. The principal stretches are calculated using the spectral decomposition of the Cauchy-Green deformation tensor evaluated using $\boldsymbol{F}^{DIC}$, i.e.,

$$\boldsymbol{C}^{DIC} = \boldsymbol{F}^{DIC,T}\boldsymbol{F}^{DIC} = \sum_{i=1}^{3} (\lambda_i^{DIC})^2 \boldsymbol{N}_i \otimes \boldsymbol{N}_i, \tag{42}$$

where $\lambda_1^{DIC} \geq \lambda_2^{DIC} \geq \lambda_3^{DIC}$ are the principal stretches and $\boldsymbol{N}_i$, $i = 1, 2, 3$, are the corresponding principal directions.

It was shown previously, in Figure 3, that for each value of η it was possible to obtain a set of material parameters such that the macroscopic force response could be matched. As η controls the evolution of the microstructure, i.e., the re-orientation of the polymer chain network, advantage will be taken of the experimental data obtained by Engqvist et al. (2016) to determine the value of this parameter. In these experiments, the evolution of the orientation distribution of carbonate groups along the polymer chain were measured during loading by WAXS. The experimental findings will be compared to the model predictions to obtain a micro-mechanically justified value of η.

The evolution of the anisotropy from the simulation is visualised using a chain orientation distribution function (CODF) defined as

$$F = F_0 \frac{\lambda_{ODF}^3}{\det(\hat{\boldsymbol{F}})}, \quad \text{where} \quad \lambda_{ODF} = \|\hat{\boldsymbol{F}}\boldsymbol{e}_0\|, \tag{43}$$

and $\hat{\boldsymbol{F}} = \boldsymbol{F}^e\bar{\boldsymbol{F}}$ is the mapping of the microstructure to the current configuration. It is assumed that the elastic part of the microstructural deformation follows the macroscopic elastic deformation. F_0 in (43) is the value of the CODF in the reference configuration, cf. Harrysson et al. (2010); Dafalias (2001). Since the initial state is assumed to be constant and isotropic, the factor F_0 becomes $F_0 = \frac{1}{4\pi}$. Figure 5 shows the CODFs before unload, at the end of the loading, for different values of η compared to experimental data from WAXS by Engqvist et al. (2016). The CODFs in Figure 5 are visualisations of data extracted from two spatial points, A and B, shown in Figure 4; Point A is the centre point of the specimen and point B is located 3 mm from the centre point along the centreline. The experimental data in Figure 5 shows the orientation distribution of carbonate groups along the polymer

chain, i.e. the orientation of the chain segments, obtained in Engqvist et al. (2016). To be comparable to the experimental results, the CODFs are computed using the through thickness average of $\hat{\boldsymbol{F}}$. As seen in Figure 5, $\eta = 1.0$ (the microstructural deformation follows the viscoplastic part of macroscopic deformation) overestimates the reorientation of the microstructure to a large extent whereas an η close to 0.75 predicts the reorientation accurately.

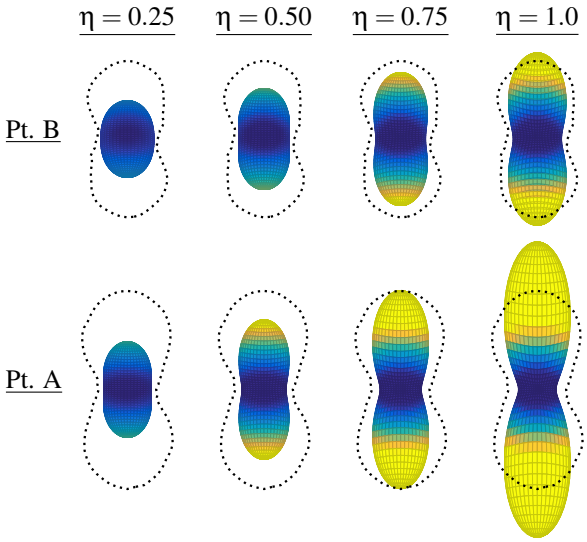

Figure 5: Visualisation of the microstructural orientation at two points on the specimen, point A and B, defined in Figure 4, using different values of the parameter η. The results are taken before unload, load step (d) shown in Figure 7. The dotted lines show the outer contour of the orientation distributions obtained experimentally from WAXS. The colors of the CODFs from the simulations are to emphasis the amount of orientation.

To further analyse the reorientation of the microstructure obtained in the simulation to the experiments, the degree of orientation is calculated using the Hermans orientation parameter (cf. Roe (2000); Ran et al. (2002)),

$$A^{nano} = \frac{3\left\langle \cos^2\phi \right\rangle - 1}{2}, \tag{44}$$

where

$$\left\langle \cos^2\phi \right\rangle = \frac{\int_0^{\pi/2} I(\phi)\cos^2\phi \sin\phi \mathrm{d}\phi}{\int_0^{\pi/2} I(\phi)\sin\phi \mathrm{d}\phi} \tag{45}$$

(not to be confused with the orientation average in (32)), I is the intensity related to consecutive carbonate groups along the polymer chain (or the value of the CODF, F) and ϕ is the azimuthal angle, being zero perpendicular to the macroscopic loading and $\pi/2$ parallel to the loading. The Hermans orientation parameter takes the values 0 for

isotropy and 1 or -0.5 for full orientation perpendicular or parallel to the loading direction, respectively.

A comparison of the orientation parameters from the experiments and from the simulation for different values of η is shown in Figure 6. The overall trend of the orientation parameter is captured well by the model. Again, it is shown that if the microstructural deformation is assumed to follow the viscoplastic macroscopic part, i.e., $\eta = 1.0$, the reorientation of the microstructure is largely overestimated. To capture the level of orientation shown in the experiments, η should have a value between 0.5 and 0.75. Based on these observations, $\eta = 0.75$ will be used in the remaining discussion.

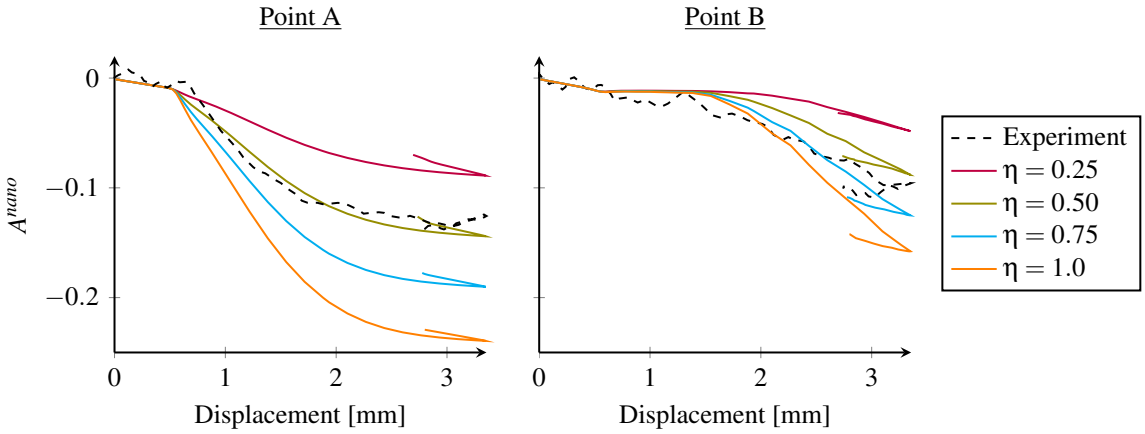

Figure 6: Hermans orientation parameter of the CODF (solid lines) and the experimental data (dashed lines) for the two spatial points shown in Figure 4.

Contour plots of λ_1^{DIC} are presented in Figure 7 at five load steps, from DIC and from the proposed model using $\eta = 0.75$. To be comparable to the experiments, the stretch from the simulation is calculated using the same approximation of the deformation gradient as for the experiments, i.e., using (41). The presented steps represents the macroscopic deformation stages shown in the load curves in Figure 7: (a) just before the peak force; (b) post-peak (0.5 mm after the peak force); (c) plateau (midway between the peak force and unload); (d) before unload; (e) fully unloaded. To avoid influence of the compliance of the loading system, the displacement was extracted from the displacement fields measured with digital image correlation. Even though the maximum stretch level is in general slightly underestimated, especially in the localisation band just after the macroscopic force peak (step (b)), the stretch fields from the proposed model show very good agreement with the experiment. The proposed model is able to capture local features of the stretch field such as: the thin localisation bands just after the force peak at load step (b); the hourglass shape between the notches at load step (c); the evolution of the localised zone between the notches with further loading and unloading (steps (c)-(e)).

The evolution of the principal stretches, for $\eta = 0.75$, is shown in Figure 8, extracted from the two spatial points, A and B. Figure 8 shows that the proposed model is able to capture the local evolution of the stretch well.

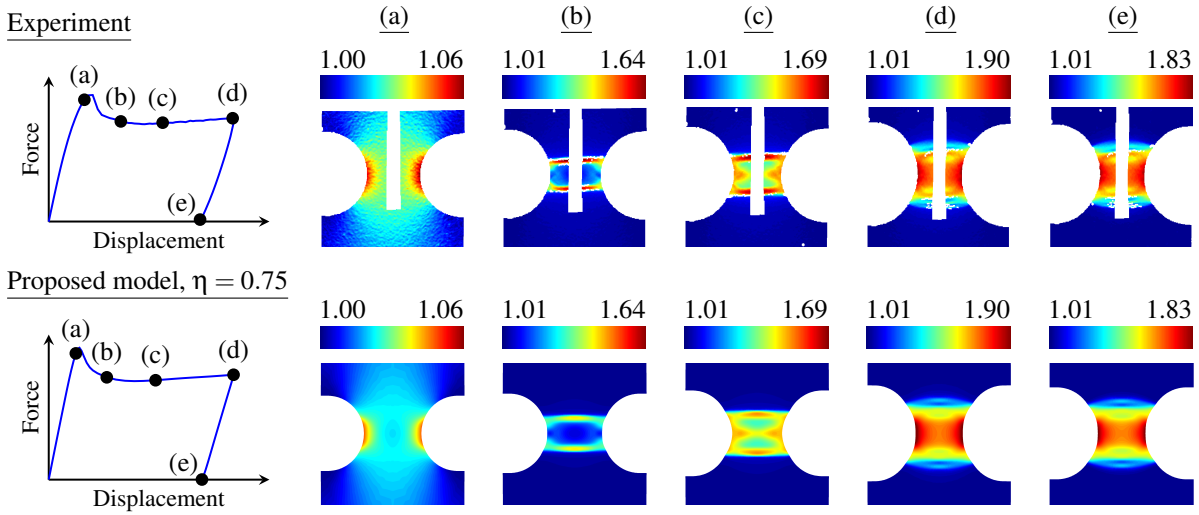

Figure 7: Contour plots of the major principal stretch, λ_1^{DIC}, from experiment (top row), the proposed model using $\eta = 0.75$ (bottom row). The stretch fields are presented at the load steps (a)-(e) shown in the macroscopic force-displacement curves on the far left.

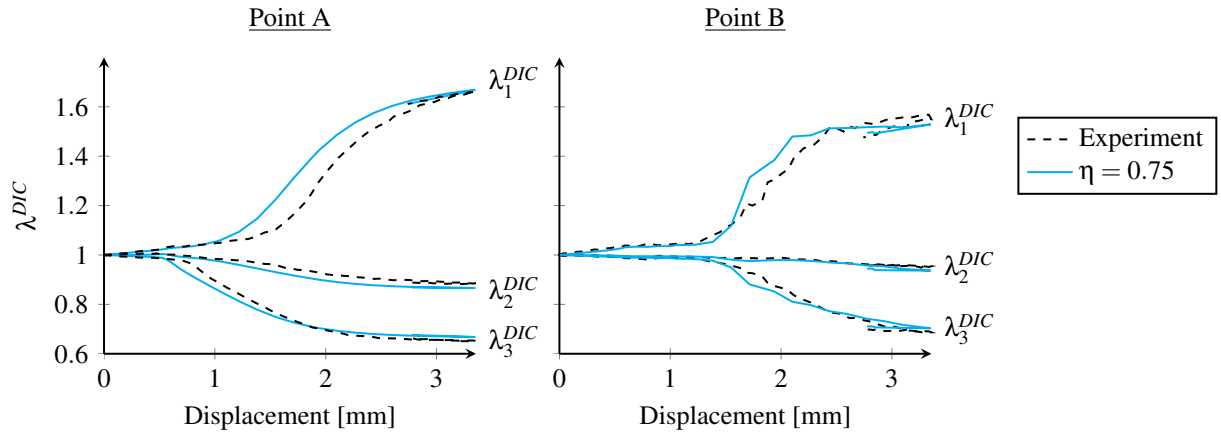

Figure 8: Principal stretches from the simulations (solid lines) and experiments for the two spatial points shown in Figure 9.

Figure 9 shows the evolution of the microstructural anisotropy, from the simulation and measured using WAXS by Engqvist et al. (2016), at the spatial points A and B. The CODFs in Figure 9 show the evolution of the microstructure from an isotropic state to a strong alignment towards the longitudinal direction as the specimen necks and the localisation front propagates along the specimen (steps (b)-(d)). After the macroscopic unload (step (e)), the CODFs show significant permanent alignment. The predicted evolution of the anisotropy shows good qualitative agreement with the experimental data.

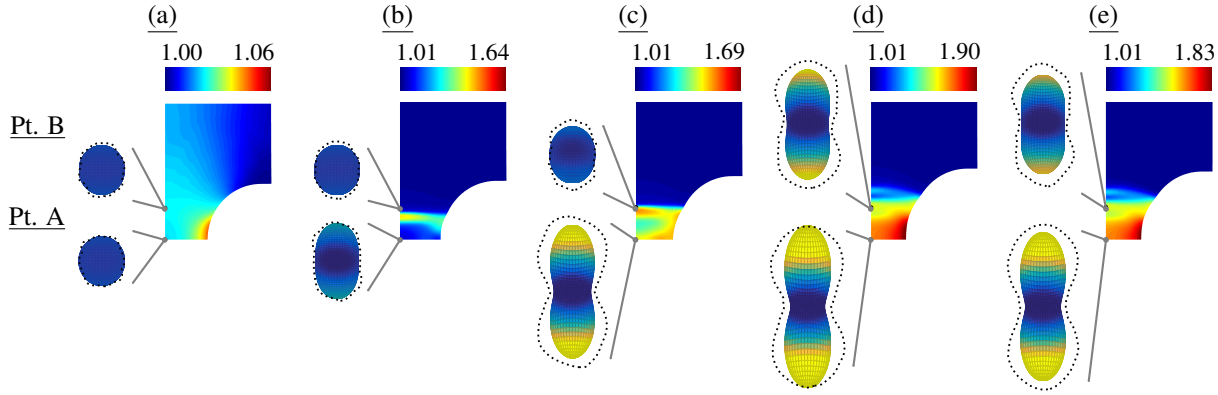

Figure 9: Visualisation of the microstructural orientation at two points on the specimen, point A and B, at the load steps shown in Figure 7. The results are from simulations using $\eta = 0.75$. The experimental results from WAXS (dotted lines), show the outer contour of the orientation distributions. The colorbars are related to the strain fields, not the CODFs whose colors are to emphasis the amount of orientation.

7 Concluding remarks

A new a physically-motivated, microstructural deformation gradient based model has been proposed to describe the mechanical behaviour of amorphous glassy polymers at finite elasto-viscoplastic deformation. The evolution of the microstructural deformation gradient is motivated by recent advanced multi-scale measurements of the deformation of PC made simultaneously over a wide range of length-scales. It is shown that to fully evaluate the predictive capacity of micro-mechanically based models, data from multi-scale experiments probing the microstructure of the material is needed. Furthermore, the polymer network is modelled using a large number of chains with evolving directions resulting in permanent reorientation of the microstructure, as indicated by the experiments.

The predicted evolution of the microstructural orientation from the model, visualised using a chain orientation distribution function, shows good qualitative agreement with wide angle X-ray scattering data. Furthermore, the predicted degree of orientation of the microstructure, quantified using Hermans orientation parameter, also agrees well with the experimental results. The comparison shows that the evolution of the anisotropy is captured by the proposed model in a physically sound manner, when choosing the microstructural parameter η based on relevant experimental data. By accurately predicting the behaviour of the underlying microstructure, the proposed model is able to capture inhomogeneous deformation phenomena, such as strain localisation, as well as the overall evolution of the deformation, measured using digital image correlation.

The good agreement between the numerical results and the experimental data, over a wide range of length-scales, indicates the great potential of accurately predicting the mechanical behaviour of glassy polymers using the proposed model. Furthermore, models that are able to a accurately predict the evolution of the anisotropy are of great impor-

tance when predicting the mechanical behaviour under multi-axial deformation as well as predicting inhomogeneities such as strain localisation, damage and fracture.

Acknowledgement

The financial support from the Crafoord foundation, grant no. 20110521, 20120632 and 20151017, as well as the beamtime and support received from the MAX IV Laboratory and the I911-SAXS beamline, proposal 20120327, is greatly acknowledged.

A Orientation average

The orientation average in (32) is evaluated by discretising the unit sphere into M orientation vectors $\{\boldsymbol{e}_0^i\}_{i=1,\dots,M}$, i.e.,

$$\langle[\cdot]\rangle = \frac{1}{4\pi}\int_{\mathbb{U}^2}[\cdot]\mathrm{d}A \approx \sum_{i=1}^{M}[\cdot]^i w^i, \tag{46}$$

where $\{w^i\}_{i=1,\dots,M}$ are the corresponding weight factors. The accuracy of the integration will increase with the number of directions, at the expense of increasing computational work. Miehe et al. (2004) concluded that for an isotropic setting, i.e. constant influence in all directions, a 42-point integration scheme was sufficient. With evolving anisotropy, the situation is more delicate since the chains will become aligned and concentrated in certain directions. To reduce the numerical error, the number of integration points needs to be increased. In this work, 368 integration points, as suggested by Heo and Xu (2001), is used for integration over the unit sphere.

B Algorithmic treatment

The algorithmic treatment of the constitutive relations used in this work is described in detail in Holopainen and Wallin (2013) and is therefore, only briefly be summarised below. An implicit Euler scheme combined with the exponential update is used to update the unknown variables, which results in the residual functions:

$$\begin{aligned}
\boldsymbol{R}_1 &= \boldsymbol{F}^e - \boldsymbol{F}\boldsymbol{F}_n^{vp-1}\exp\left(-\Delta t(\boldsymbol{D}^{vp}+\boldsymbol{W}^{vp})\right),\\
\boldsymbol{R}_2 &= \bar{\boldsymbol{F}} - \exp\left(\Delta t(\eta\boldsymbol{D}^{vp}+\boldsymbol{W}^{vp})\right)\bar{\boldsymbol{F}}_n,\\
\boldsymbol{R}_3 &= \boldsymbol{F}^{eT} - \boldsymbol{F}^e,\\
\boldsymbol{R}_4 &= \boldsymbol{W}^{vpT} + \boldsymbol{W}^{vp},\\
R_5 &= (s_1 - s_{1_n} - h_1\left(1-\frac{s_1}{s_{ss}}\right)\dot{\gamma}^{vp}\Delta t)/s_0,\\
R_6 &= (s_2 - s_{2_n} - h_2\dot{\gamma}^{vp}\Delta t)/s_0.
\end{aligned} \tag{47}$$

An exponential approximation is used to update the plastic and microstructural deformation gradients. The tensor exponent in (47) is calculated using the Padé approximation (cf. Steinmann and Stein (1996)). In (47), $[\cdot]_n$ refers to the quantity from the last state of equilibrium and $\Delta t > 0$ is the time increment. The antisymmetric plastic spin tensor, $\boldsymbol{W}^p$, is introduced to satisfy the constraint, $\boldsymbol{R}^e = \boldsymbol{1}$. The non-linear system in (47) is solved using a Newton-Raphson iteration scheme. To this end, the residual functions are collected in the vector, $\boldsymbol{R} = [\boldsymbol{R}_1\ \boldsymbol{R}_2\ \boldsymbol{R}_3\ \boldsymbol{R}_4\ R_5\ R_6]^T$ and the unknown variables are collected in the vector, $\boldsymbol{Y} = [\boldsymbol{F}^e\ \boldsymbol{W}^{vp}\ \bar{\boldsymbol{F}}\ s_1\ s_2]^T$. The updated variables are calculated as $\boldsymbol{Y}_{n+1} = \boldsymbol{Y}_n + \Delta\boldsymbol{Y}$ where

$$\Delta\boldsymbol{Y} = -\boldsymbol{J}^{-1}\boldsymbol{R} \quad \text{and} \quad \boldsymbol{J} = \frac{\partial \boldsymbol{R}}{\partial \boldsymbol{Y}} \tag{48}$$

is the Jacobian, obtained through automatic differentiation using the tool OpenAD Utke et al. (2008).

References

Ames, N. M., Srivastava, V., Chester, S. A., Anand, L., 2009. A thermo-mechanically coupled theory for large deformations of amorphous polymers. Part II: Applications. International Journal of Plasticity 25 (8), 1495–1539.

Anand, L., Ames, N. M., Srivastava, V., Chester, S. A., 2009. A thermo-mechanically coupled theory for large deformations of amorphous polymers. Part I: Formulation. International Journal of Plasticity 25 (8), 1474–1494.

Anand, L., Gurtin, M. E., 2003. A theory of amorphous solids undergoing large deformations, with application to polymeric glasses. International Journal of Solids and Structures 40 (6), 1465–1487.

Argon, A., 1973. A theory for the low-temperature plastic deformation of glassy polymers. Philosophical Magazine 28 (4), 839–865.

Arruda, E. M., Boyce, M. C., 1991. Evolution of plastic anisotropy in amorphous polymers during finite straining. In: Boehler, J.-P., Khan, A. S. (Eds.), Anisotropy and Localization of Plastic Deformation. Elsevier Applied Science, London, pp. 483–488.

Arruda, E. M., Boyce, M. C., 1993. A three-dimensional constitutive model for the large stretch behavior of rubber elastic materials. Journal of the Mechanics and Physics of Solids 41 (2), 389–412.

Boyce, M., Arruda, E., 1990. An experimental and anaiytical investigation of the large strain compressive and tensile response of glassy polymers. Polymer Engineering & Science 30 (20), 1288–1298.

Boyce, M. C., Arruda, E. M., Jayachandran, R., 1994. The large strain compression, tension, and simple shear of polycarbonate. Polymer Engineering & Science 34 (9), 716–725.

Boyce, M. C., Parks, D. M., Argon, A. S., 1988. Large inelastic deformation of glassy polymers. Part I: rate dependent constitutive model. Mechanics of Materials 7 (1), 15–33.

Chakkarapani, V., Ravi-Chandar, K., Liechti, K., 2006. Characterization of multiaxial constitutive properties of rubbery polymers. Journal of engineering materials and technology 128 (4), 489–494.

Chowdhury, K., Talreja, R., Benzerga, A. A., 2008. Effects of manufacturing-induced voids on local failure in polymer-based composites. Journal of Engineering Materials and Technology 130 (2), 021010.

Cohen, A., 1991. A Padé approximant to the inverse Langevin function. Rheologica Acta 30 (3), 270–273.

Coleman, B. D., Gurtin, M. E., 1967. Thermodynamics with internal state variables. The Journal of Chemical Physics 47 (2), 597–613.

Dafalias, Y. F., 2001. Orientation distribution function in non-affine rotations. Journal of the Mechanics and Physics of Solids 49 (11), 2493–2516.

Dreistadt, C., Bonnet, A.-S., Chevrier, P., Lipinski, P., 2009. Experimental study of the polycarbonate behaviour during complex loadings and comparison with the Boyce, Parks and Argon model predictions. Materials & Design 30 (8), 3126–3140.

Engqvist, J., Hall, S., Wallin, M., Ristinmaa, M., Plivelic, T., 2014. Multi-scale Measurement of (Amorphous) Polymer Deformation: Simultaneous X-ray Scattering, Digital Image Correlation and In-situ Loading. Experimental Mechanics 54 (8), 1373–1383.

Engqvist, J., Wallin, M., Hall, S. A., Ristinmaa, M., Plivelic, T. S., 2016. Measurement of multi-scale deformation of polycarbonate using x-ray scattering with in-situ loading and digital image correlation. Polymer 82, 190–197.

G'sell, C., Jonas, J., 1979. Determination of the plastic behaviour of solid polymers at constant true strain rate. Journal of Materials Science 14 (3), 583–591.

Harrysson, M., Ristinmaa, M., Wallin, M., Menzel, A., 2010. Framework for deformation induced anisotropy in glassy polymers. Acta Mechanica 211 (3-4), 195–213.

Heo, S., Xu, Y., 2001. Constructing fully symmetric cubature formulae for the sphere. Mathematics of Computation 70 (233), 269–279.

Holopainen, S., Wallin, M., 2013. Modeling of the Long-Term Behavior of Glassy Polymers. Journal of Engineering Materials and Technology 135 (1), 011001.

Kweon, S., Benzerga, A., 2013. On the localization of plastic flow in glassy polymers. European Journal of Mechanics-A/Solids 39, 251–267.

Labrador, A., Cerenius, Y., Svensson, C., Theodor, K., Plivelic, T., 2013. The yellow mini-hutch for saxs experiments at max iv laboratory. In: Journal of Physics: Conference Series. Vol. 425. IOP Publishing, p. 072019.

Miehe, C., Göktepe, S., Lulei, F., 2004. A micro-macro approach to rubber-like materials – Part I: the non-affine micro-sphere model of rubber elasticity. Journal of the Mechanics and Physics of Solids 52 (11), 2617–2660.

Miehe, C., Göktepe, S., Mendez Diez, J., 2009. Finite viscoplasticity of amorphous glassy polymers in the logarithmic strain space. International Journal of Solids and Structures 46 (1), 181–202.

Parsons, E., Boyce, M., Parks, D., 2004. An experimental investigation of the large-strain tensile behavior of neat and rubber-toughened polycarbonate. Polymer 45 (8), 2665–2684.

Poulain, X., Kohlman, L., Binienda, W., Roberts, G., Goldberg, R., Benzerga, A., 2013. Determination of the intrinsic behavior of polymers using digital image correlation combined with video-monitored testing. International Journal of Solids and Structures 50 (11), 1869–1878.

Qvale, D., Ravi-Chandar, K., 2004. Viscoelastic characterization of polymers under multiaxial compression. Mechanics of time-dependent materials 8 (3), 193–214.

Ran, S., Wang, Z., Burger, C., Chu, B., Hsiao, B. S., 2002. Mesophase as the precursor for strain-induced crystallization in amorphous poly (ethylene terephthalate) film. Macromolecules 35 (27), 10102–10107.

Ravi-Chandar, K., Ma, Z., 2000. Inelastic deformation in polymers under multiaxial compression. Mechanics of Time-Dependent Materials 4 (4), 333–357.

Roe, R. J., 2000. Methods of X-ray and neutron scattering in polymer science. Oxford University Press New York.

Rössle, W., Lindner, P., Dettenmaier, M., 1989. Deformation of glassy polycarbonate studied by neutron scattering. Physica B: Condensed Matter 156, 414–416.

Schubach, H., Heise, B., 1986. Structure and anisotropy in polycarbonate. I. Short range order of amorphous polycarbonate revealed by WAXS. Colloid and Polymer Science 264 (4), 335–342.

Steinmann, P., Stein, E., 1996. On the numerical treatment and analysis of finite deformation ductile single crystal plasticity. Computer Methods in Applied Mechanics and Engineering 129 (3), 235–254.

Stoclet, G., Seguela, R., Lefebvre, J., Elkoun, S., Vanmansart, C., 2010. Strain-induced molecular ordering in polylactide upon uniaxial stretching. Macromolecules 43 (3), 1488–1498.

Treloar, L., Riding, G., 1979. A non-Gaussian theory for rubber in biaxial strain. I. Mechanical properties. In: Proceedings of the Royal Society of London A: Mathematical, Physical and Engineering Sciences. Vol. 369. The Royal Society, pp. 261–280.

Treloar, L. R. G., 1975. The physics of rubber elasticity. Oxford University Press, USA.

Tvergaard, V., Needleman, A., 2011. Polymer indentation: numerical analysis and comparison with a spherical cavity model. Journal of the Mechanics and Physics of Solids 59 (9), 1669–1684.

Tvergaard, V., Needleman, A., 2012. Effect of viscoplastic material parameters on polymer indentation. Modelling and Simulation in Materials Science and Engineering 20 (6), 065002.

Utke, J., Naumann, U., Fagan, M., Tallent, N., Strout, M., Heimbach, P., Hill, C., Wunsch, C., 2008. OpenAD/F: A modular open-source tool for automatic differentiation of Fortran codes. ACM Transactions on Mathematical Software (TOMS) 34 (4), 18.

van Melick, H., Bressers, O., Den Toonder, J., Govaert, L., Meijer, H., 2003. A microindentation method for probing the craze-initiation stress in glassy polymers. Polymer 44 (8), 2481–2491.

VanLandingham, M. R., Chang, N.-K., Drzal, P., White, C., Chang, S.-H., 2005. Viscoelastic characterization of polymers using instrumented indentation. i. quasi-static testing. Journal of Polymer Science Part B: Polymer Physics 43 (14), 1794–1811.

Wallin, M., Ristinmaa, M., 2005. Deformation gradient based kinematic hardening model. International Journal of Plasticity 21 (10), 2025–2050.

Wallin, M., Ristinmaa, M., Ottosen, N. S., 2003. Kinematic hardening in large strain plasticity. European Journal of Mechanics-A/Solids 22 (3), 341–356.

Wu, P., van der Giessen, E., 1993. On improved network models for rubber elasticity and their applications to orientation hardening in glassy polymers. Journal of the Mechanics and Physics of Solids 41 (3), 427–456.

Paper D

Jonas Engqvist, Mathias Wallin,
Matti Ristinmaa and Stephen A. Hall

Modelling and experiments of glassy polymers using biaxial loading and digital image correlation

To be submitted for publication

Modelling and experiments of glassy polymers using biaxial loading and digital image correlation

Jonas Engqvist[a], Mathias Wallin[a],
Matti Ristinmaa[a] and Stephen A. Hall[a,b]

[a]Division of Solid Mechanics Lund University, Box 118, S-221 00 Lund, Sweden

[b]European Spallation Source AB, P.O. Box 176, 221 00, Lund, Sweden

Abstract

Experimental data are needed to evaluate constitutive models. The richer the experimental data, in terms of different deformation modes for example, the better the constraints on the model. To this end, the mechanical response of glassy polycarbonate (PC) is studied using biaxial tension experiments. Deformation fields, measured using full-field digital image correlation (DIC), reveal a large difference in the strain localisation behaviour of the material, depending on the amount of lateral deformation. The difference in the localisation behaviour is also reflected in the macroscopic force-displacement response. The experimental data acquired in experiments are used to examine the ability of a physically-motivated constitutive model to predict the mechanical response of glassy PC during biaxial deformation. To improve the numerical predictions, the elastic part of the constitutive model is modified such that the initial non-linear response due to volumetric deformation is accurately captured. This new elastic model is motivated by the experimental results that show that the commonly used quadratic form of the elastic free energy results in a too stiff response during biaxial tension.

1 Introduction

Polycarbonate (PC) is an amorphous polymer with a relatively high glass transition temperature, a high impact strength and good optical properties. Due to theses favourable features, PC is often used in industry and consumer products such as safety glass, machine guards and containers. Glassy amorphous polymers, such as PC at room temperature, are commonly used as load carrying components in which the material will likely be subjected to multi-axial loading conditions and complex deformation history. The understanding of, and the ability to predict, the mechanical properties and the evolution of the material under mechanical load is, therefore, of great importance during the design process of such components.

Over the years, a considerable amount of work has gone into refining the constitutive models for predicting the mechanical behaviour of glassy polymers. Many models make use of non-Gaussian chain statistics to represent the macromolecular network. Boyce et al. (1988) proposed a 3-chain model to represent the polymer network using the non-Gaussian statistical model by Wang and Guth (1952). As the 3-chain model was unable to accurately distinguish between different states of deformation, Arruda and Boyce (1991, 1993) proposed a model using eight chains to represent the polymer network that better captures the mechanical behaviour found experimentally. In the 8-chain model, the chains extend from the centre to the corners of a unit cube. Wu and van der Giessen (1993) showed that the three- and eight-chain models can represent an upper and lower bound for the network stiffness, respectively. Motivated by this, Wu and van der Giessen (1993) proposed a linear combination of the two models. In the same paper, they also used the full-network model by Treloar and Riding (1979) to model the response of glassy PC under three-dimensional loading. The full-network model uses a chain orientation distribution function (CODF) to distribute a large number of chains during deformation. Later, Harrysson et al. (2010) proposed a model capable of having a non-affine evolution of the microstructure using a CODF.

Many amorphous solids exhibit a non-linear response at small strains prior to a stress peak. Different approaches have been suggested to predict the smooth, pre-peak transition.Hasan and Boyce (1995) developed a one-dimensional framework for the viscoplastic flow of glassy polymers, using a set of internal state variables to describe the evolution of the microstructure. The flow theory by Hasan and Boyce, which is based on evolution of free volume, is able to predict a smooth pre-peak transition. This flow theory was later implemented in a three-dimensional setting by Miehe et al. (2011). Anand and Gurtin (2003) used a single internal state variable related to the local free volume to capture the non-linear pre-peak behaviour. Chowdhury et al. (2008) used a different approach to improve the small strain behaviour by splitting the variable related to the strain softening, introduced by Boyce et al. (1988), into two parts, which results in a smooth transition from elastic to plastic response compared with the original model.

When characterising the mechanical response of polymers, the focus has often been on the macroscopic stress-strain response from uni-axial or multiaxial compression tests

where the deformation is measured at the boundaries of the specimen, or using an extensometer, cf. e.g. Arruda et al. (1995); Dreistadt et al. (2009); Ames et al. (2009). For such macroscopic response to be representative, the deformation must be homogeneous within the gauge length, i.e. necking, barreling or buckling are not allowed. When the deformation is inhomogeneous the need for full-field measurement techniques that provide displacement measurement at a large number of measurement points is evident. One available full-field technique is digital image correlation (DIC) where the deformation is measured by tracking the motion of pixel subsets in images taken of a specimen during different stage of deformation, cf. Parsons et al. (2004, 2005); Grytten et al. (2009); Poulain et al. (2013). As full-field measurements can be applied to experiments performed under inhomogeneous condition, the outcome of such experiments can provide richer information about the material behaviour. By performing experiments under multiaxial and/or inhomogeneous deformation conditions, a few tests can be used to identify large sets of constitutive parameters, cf. Hild and Roux (2006); Avril et al. (2008). Multiaxial loading can be achieved in several ways, such as: multiaxial compression (e.g. Ravi-Chandar and Ma (2000)); using tube specimen and combining pressure with axial and/or torsional loads (e.g. Hu et al. (2003)) or biaxial tension loading (e.g. Chevalier et al. (2001); Johlitz and Diebels (2011)).

Various approaches, many of which use relatively pure deformation modes, have been used to evaluate the performance of constitutive models. Tests performed under uni-axial, simple shear or plane strain conditions where the experimental data consists of the macroscopic response has been used by, e.g., Boyce and Arruda (1990); Tomita (2000); Harrysson et al. (2010); Holopainen and Wallin (2013) to validate the performance of the models developed within each work. As has been discussed above, to capture inhomogeneous deformation experimentally, full-field methods should be utilised. In the works by, e.g., Miehe et al. (2009) and Engqvist et al. (2016b) DIC has been used in combination with uni-axial tension tests of dog-bone shaped or notched specimens to evaluate constitutive models. By comparing the simulated response to measured deformation fields, a more comprehensive evaluation of the model is possible, as not only the macroscopic response of the structure is available for comparison but also local variations of the deformation can be studied. While a comparison to uni-axial tensile experiments tests the ability to capture inhomogeneous deformation in terms of necking and neck propagation, it does not, in general, include much information about the influence of shear or volumetric deformation. To this end, more general deformations have been studied by e.g., combined tensile and shear deformation of glassy PC by Holopainen and Wallin (2013), biaxial tensile loading of silicone rubber by Johlitz and Diebels (2011) and creasing of paperboard by Borgqvist et al. (2015).

An aggravating factor when studying more complex deformation is the general lack of experimental data, since this often requires non-standard test equipment. To this end, biaxial tensile experiments of glassy PC have been conducted within this work. The deformation of the specimen is measured using full-field 3D-surface DIC. The experimental data are used to explore, and improve, the ability of the physically-motivated constitutive model by Engqvist et al. (2016b) to predict the mechanical response of glassy PC.

2 Preliminaries

Referring to the coordinate system defined in Figure 1, the x, y and z directions are denoted *lateral*, *axial* and *out-of-plane* or *thickness* direction, respectively. Second order tensors and vectors are denoted by bold-face Roman letters and the second order unit tensor is denoted by $\mathbf{1}$. The transpose and the inverse of a second order tensor are denoted as $[\cdot]^T$ and $[\cdot]^{-1}$, respectively. The superscript $[\cdot]^{\text{dev}}$ denotes the deviatoric part of a second order tensor, defined as $[\cdot]^{\text{dev}} = [\cdot] - \frac{1}{3}\text{tr}[\cdot]\mathbf{1}$ where tr$[\cdot]$ denotes the trace of the tensor. The symmetric part of a second order tensor is denoted as $\text{sym}[\cdot] = \frac{1}{2}([\cdot] + [\cdot]^T)$. A superposed dot denotes the material time derivative, i.e., $\dot{[\cdot]}$. The dyadic product is denoted as $\otimes$.

3 Experimental procedure

The experiments involved biaxial cold drawing of amorphous glassy PC to study the behaviour during multi-axial deformation. During the experiments, the mesoscopic deformations, at the surface of the specimens, were measured using DIC. Asymmetrically notched specimen, designed to focus the deformation into a well defined area, were machined from 2 mm thick sheets of commercial PC, see Figure 1a. By having an offset of the notches, the geometry promotes shear deformation between the notches when stretched uni-axially. All experiments have been performed at room temperature.

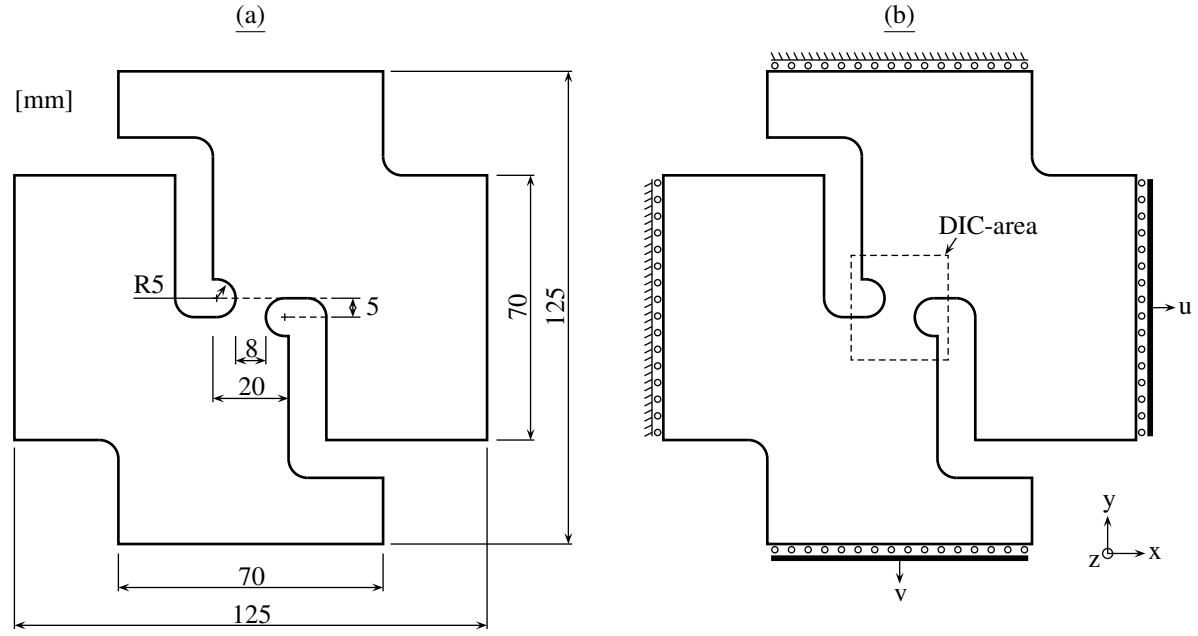

Figure 1: (a) The dimensions of the specimen used in the biaxial deformation experiments and (b) the boundary conditions during loading and simulation. The area where the deformation is measured using DIC is indicated in (b).

3.1 Biaxial tensile testing

Biaxial loading was performed using a custom built tensile test device equipped with two motors, arranged in a cruciform manner, see Figure 2. Harrysson and Ristinmaa (2008) used the same device previously to study the biaxial response of paperboard. The device allows for independent control of the motors, making it possible to apply non-proportional loading along the two loading axes. All four grips are fitted with ball bearings to allow them to move freely sideways, see Figure 1b. As the loading device is designed to let the grips move sideways without resistance, and to not constrain the specimen, the compliance of the machine is larger than when using fixed grips. To compensate for this compliance, the loading system was equipped with a camera system to track the displacements close to the grips. This system consisted of a 5-Megapixel camera and a Raspberry Pi computer which acquired images with an approximate frame rate of 3 frames per second and an inhouse developed point-tracking code. During the experiments, the displacements of the moving grips and the axial forces were recorded using linear displacement sensors and load cells, respectively. The deformation at the surface of the specimen was measured using 3D-surface DIC, zoomed in on the area surrounding the notches to gain spatial resolution, see Figure 1b.

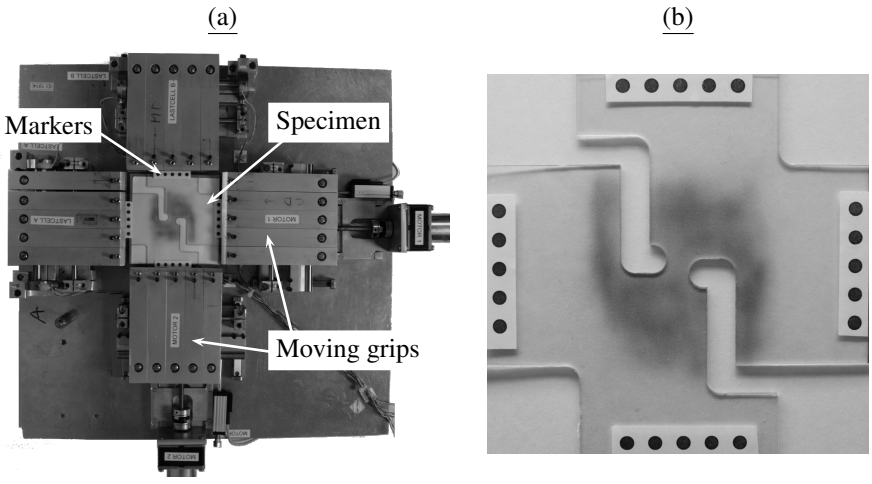

Figure 2: (a) The experimental set-up showing the biaxial tensile test device and a specimen. (b) Zoomed in at the specimen with applied speckle pattern and markers for the point-tracking.

To study the influence of lateral deformation, experiments were performed with a fixed macroscopic deformation rate of $|\dot{v}| = 1$ mm/min in the axial direction while the deformation in the lateral direction was varied; see Figure 1. Three different load cases were used with the following deformations in the lateral direction: (1) traction free; (2) half the displacement rate as in the axial direction; (3) same displacement rate as in the axial direction. The different load cases are summarised in Table 1. Due to the compliance of the tensile device, the resulting displacement rates in the lateral direction differed slightly

from the intended ones. It is, however, assumed that the overall results of the experiments is unaffected by the deviation from the intended displacement rates. Note that the true displacements were measured by tracking the markers on the specimens.

Table 1: The different load cases used in the experiments.

Load case	u_{max} mm	$\lvert\dot{u}\rvert$ mm/min	v_{max} mm	$\lvert\dot{v}\rvert$ mm/min
1	Free		3	1
2	1.5	0.5	3	1
3	3	1	3	1

3.2 Digital image correlation

Full-field 3D-surface DIC was used to measure the deformation at the surface of the specimen during loading. Two Prosilica GT6600 (Allied Vision Technologies) 29-Megapixel digital cameras, calibrated for stereo-vision, where used for the DIC system. The stereo-vision enabled measurement of both the in-plane and the out-of-plane deformation. As PC exhibits large out-of-plane deformations when the specimen necks in tension, the out-of-plane measurement is needed. The commercial software Vic-3D (Correlated Solutions) was used for the stereo calibration and the image correlation. A correlation window size of 61×61 and a step size of 7 pixels were used during the image correlation. Due to the lack of texture of the specimen surface, a random speckle pattern was applied on the surface to enable the correlation, see Figure 2b.

The displacement field acquired from DIC was used to approximate the deformation gradient using the closest neighbouring windows on a regular, 7 pixel, grid. When calculating the deformation gradient, the out-of-plane displacement must be approximated since the DIC only measures the deformation at the surface of the specimen. By assuming that the deformation is homogeneous through the thickness of the specimen, the deformation gradient can be expressed as

$$\boldsymbol{F}^{DIC} = \begin{bmatrix} 1 + \frac{\partial u}{\partial X} & \frac{\partial u}{\partial Y} & 0 \\ \frac{\partial v}{\partial X} & 1 + \frac{\partial v}{\partial Y} & 0 \\ \frac{\partial w}{\partial X} & \frac{\partial w}{\partial Y} & 1 + \frac{2w}{T_0} \end{bmatrix} \tag{1}$$

in a fixed Cartesian coordinate system, where u, v and w are the displacements in the x, y and z direction (see Figure 1b), measured at the surface using DIC. The thickness of the undeformed specimen in the z-direction (out-of-plane direction) is denoted T_0. In the following, the major principle stretch, λ_1^{DIC}, will be used as a deformation measure. The principal stretch is calculated using the spectral decomposition of the right Cauchy-Green deformation tensor calculated using $\boldsymbol{F}^{DIC}$, i.e.,

$$\boldsymbol{C}^{DIC} = \boldsymbol{F}^{DIC,T}\boldsymbol{F}^{DIC} = \sum_{i=1}^{3} (\lambda_i^{DIC})^2 \boldsymbol{N}_i \otimes \boldsymbol{N}_i, \tag{2}$$

where $\lambda_1^{DIC} \geq \lambda_2^{DIC} \geq \lambda_3^{DIC}$ are the principal stretches and $\boldsymbol{N}_i$, $i = 1, 2, 3$, are the corresponding principal directions.

4 Experimental results

Figure 3 shows the macroscopic response from three tests, where the displacements are measured using the point tracking system discussed in Section 3.1. The macroscopic force-displacement curves in the axial direction show a significant dependence on the deformation in the lateral direction. Load cases 1 and 3 show a broad, s-shaped macroscopic force peak whereas only one peak with a rapid decrease of the force is visible in load case 2. The initial stiffness in the axial direction increases as the amount of lateral deformation increases. As will be shown later, the stiffness does not increase as much as predicted by the commonly used quadratic form of the elastic free energy.

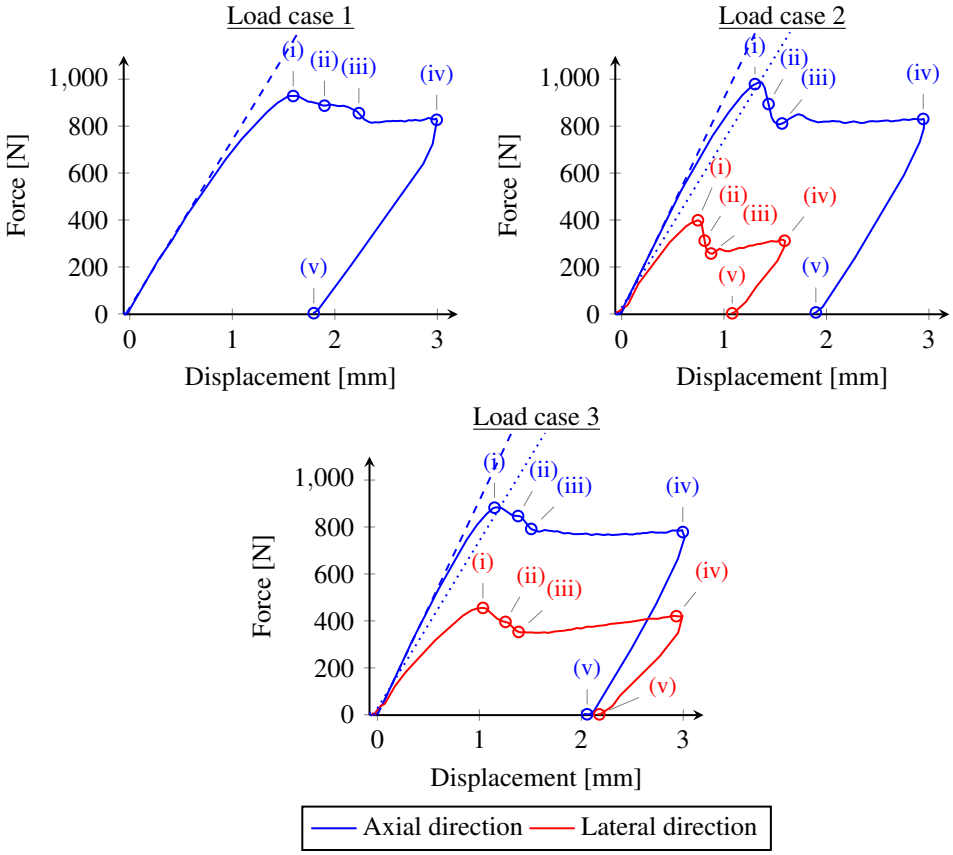

Figure 3: Characteristic macroscopic force-displacement curves from the three different load cases. The markers indicate the load steps from which contour plots of the major principle stretch from DIC, λ_1^{DIC}, are presented in Figure 4. The straight, dashed lines show the initial stiffness in the axial direction for each load case. As a comparison, the initial stiffness in load case 1 is shown as dotted lines in load cases 2 and 3.

Figure 4 presents contour plots of the major principle stretch from DIC, λ_1^{DIC}, in which an explanation for the different macroscopic responses can be found. The contour plots from load cases 1 and 3 show that the first drop in the macroscopic force (load steps (i)-(ii) shown in Figure 3) is associated with the formation of pairs of localisation bands close to the notches while the second force drop (load steps (ii)-(iii)) is associated with the formation of a localisation band connecting the two previous localisations. The double localisation bands associated with the first force drop in load cases 1 and 3 are not as pronounced in load case 2, but the sharp force peak is rather associated with the formation of a single localisation band between the notches at the force peak (load steps (i)-(ii)). Another significant difference, shown by the DIC, is the inclination angle of the localisation band that eventually is formed between the notches. For load case 1, the inclination angle is about 30° while the angle for the two other load cases is about 10° going the other direction, see load step (iii) in Figure 4.

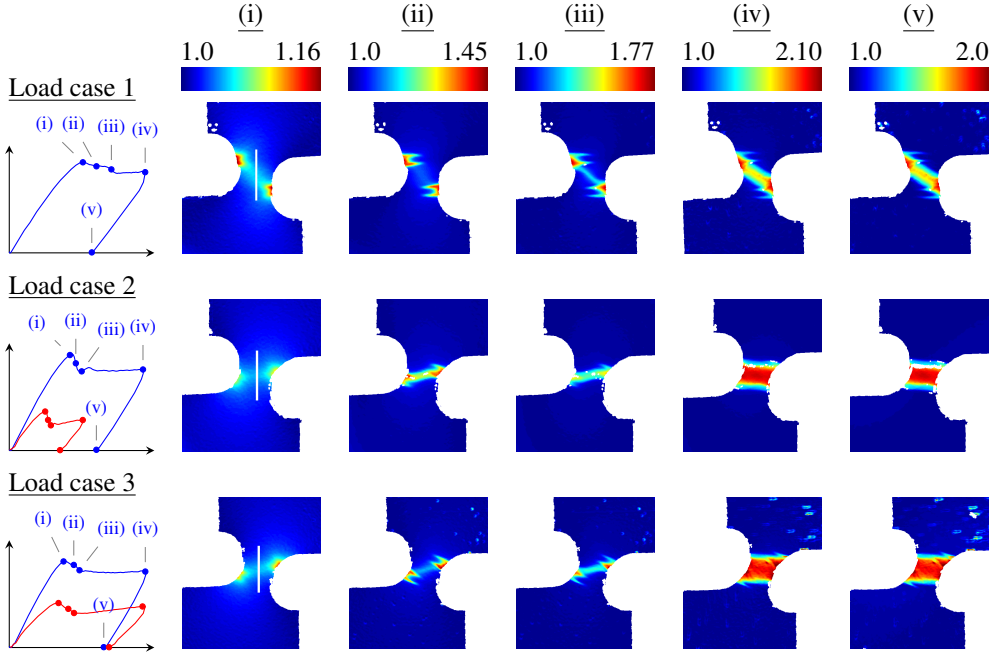

Figure 4: Contour plots of the major principle stretch measured using DIC, λ_1^{DIC}, from the different load cases. The load steps, for which the contour plots are presented, are shown in Figure 3. The white lines at load step (i) show from where the section line plots in Figure 5 are extracted.

To study the progress of the strain localisation cross the specimen, line section plots of λ_1^{DIC} are presented in Figure 5. The stretch in Figure 5 is plotted along the vertical lines indicated in Figure 4. At load step (i), the deformation along the line section shows small variations for all three load cases. The line plots for load case 1 show the formation of the two pairs of localisation bands at load step (ii) which is followed by the central localisation band going across the specimen at load step (iii). After the formation of the

central localisation, the progress of the smaller localisation pairs decreases significantly and further deformation occurs mainly in the central localisation. For the two other load cases, the section line plots show a single localisation formed in the centre of the notches at load step (ii) and (iii) for load case 2 and 3, respectively. As the macroscopic deformation progress, the width of the localisation zone increases along with increasing stretch levels.

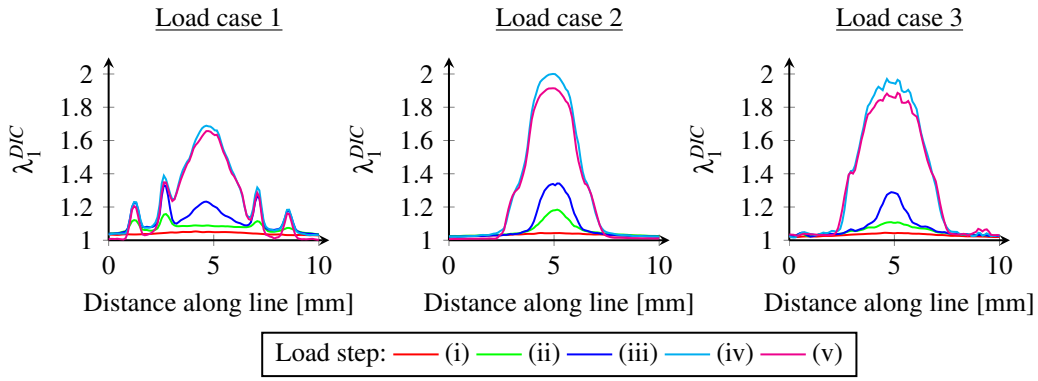

Figure 5: Section line plots of the major principle stretch, λ_1^{DIC}, at the load steps shown in Figure 3. The stretch is extracted along the line indicated in Figure 4 midway between the notches.

5 Model description

In the following, the model developed by Engqvist et al. (2016b) is used. For completeness the model is summarised below. However, the elastic response of the model is modified based on the experimental results presented in the preceding section.

5.1 Kinematic

The different configurations used to describe the motion of a body are shown in Figure 6 where the regions that are occupied by the body at time t_0 and time $t > t_0$ are denoted as the reference configuration Ω_0 and current configuration Ω, respectively. The kinematic quantities are summarised Table 2.

Motivated by the X-ray scattering experiments of Engqvist et al. (2016a), Engqvist et al. (2016b) introduced separate deformation gradients to describe the deformations of the macro- and microstructures. The microstructural deformation gradient, denoted $\bar{\boldsymbol{F}}$, maps vectors related to the microstructure from the undeformed reference configuration to the intermediate configuration. The microstructural velocity gradient, $\bar{\boldsymbol{l}} = \dot{\bar{\boldsymbol{F}}}\bar{\boldsymbol{F}}^{-1}$, is split into a symmetric and a skew-symmetric part as $\bar{\boldsymbol{l}} = \bar{\boldsymbol{d}} + \bar{\boldsymbol{w}}$ where $\bar{\boldsymbol{d}}$ is the symmetric part and $\bar{\boldsymbol{w}}$ is the skew-symmetric part. Following Dafalias (2001), $\bar{\boldsymbol{d}}$ and $\bar{\boldsymbol{w}}$ is chosen as $\bar{\boldsymbol{d}} = \eta \boldsymbol{D}^{vp}$ and $\bar{\boldsymbol{w}} = \boldsymbol{W}^{vp}$, i.e.,

$$\bar{\boldsymbol{l}} = \eta \boldsymbol{D}^{vp} + \boldsymbol{W}^{vp}, \tag{3}$$

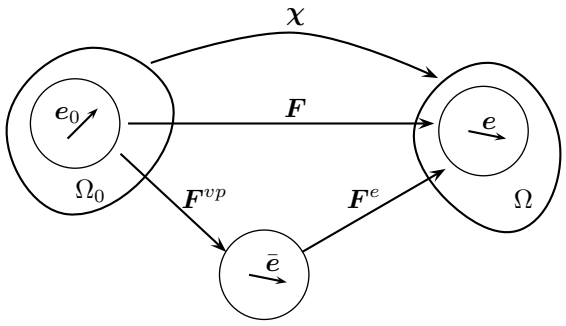

Figure 6: Illustration of the kinematic description of the continuum and the microstructure.

where $\boldsymbol{D}^{vp}$ is the macroscopic viscoplastic rate of deformation, $\boldsymbol{W}^{vp}$ is the macroscopic viscoplastic spin tensor and η is a constitutive parameter associated with the deformation of the microstructure. If $\eta \neq 1$, the deformation of the microstructure will differ from the macroscopic deformation since $\bar{\boldsymbol{l}}$ will differ from $\boldsymbol{L}^{vp}$. The right Cauchy-Green tensor $\bar{\boldsymbol{C}}$ and the Finger tensor $\bar{\boldsymbol{b}}$ associated with the deformation of the microstructure are defined as

$$\bar{\boldsymbol{C}} = \bar{\boldsymbol{F}}^T \bar{\boldsymbol{F}} \quad \text{and} \quad \bar{\boldsymbol{b}} = \bar{\boldsymbol{F}} \bar{\boldsymbol{F}}^T, \tag{4}$$

respectively.

The experiments by Engqvist et al. (2016a) showed a permanent reorientation of the chain segments due to macroscopic deformation. This reorientation is included in the model by a set of unit vectors, $\bar{\boldsymbol{e}}$, describing the orientation of the microstructure. The vector $\bar{\boldsymbol{e}}$ is obtained by mapping $\boldsymbol{e}_0$ in the reference configuration using the microstructural deformation gradient, i.e.,

$$\bar{\boldsymbol{e}} = \frac{\bar{\boldsymbol{F}} \boldsymbol{e}_0}{\|\bar{\boldsymbol{F}} \boldsymbol{e}_0\|}, \tag{5}$$

as obtained by a mapping of $\boldsymbol{e}_0$ using $\bar{\boldsymbol{F}}$, where $\bar{\boldsymbol{e}}$ is a unit vector in the intermediate configuration, cf. Figure 6.

5.2 Specific model

The evolution of the macroscopic viscoplastic deformation is given by

$$\boldsymbol{D}^{vp} = \dot{\gamma}^{vp} \boldsymbol{N}, \tag{6}$$

where $\dot{\gamma}^{vp}$ is the plastic shear strain rate. The direction of the viscoplastic flow, $\boldsymbol{N}$, is assumed to be aligned with the deviatoric part of driving stress $\tilde{\boldsymbol{\tau}}^{\text{dev}}$, i.e.,

$$\boldsymbol{N} = \frac{1}{\sqrt{2}\tau} \tilde{\boldsymbol{\tau}}^{\text{dev}}, \quad \tau = \sqrt{\frac{1}{2} \tilde{\boldsymbol{\tau}}^{\text{dev}} : \tilde{\boldsymbol{\tau}}^{\text{dev}}}, \tag{7}$$

Table 2: Kinematic quantities

$\boldsymbol{\chi}(\boldsymbol{X}, t)$	Motion
$\boldsymbol{F} = \nabla_{\boldsymbol{x}} \boldsymbol{\chi}$, $J = \det(\boldsymbol{F}) > 0$	Deformation gradient
$\boldsymbol{F} = \boldsymbol{F}^e \boldsymbol{F}^{vp}$	Elasto-viscoplastic split of $\boldsymbol{F}$
$\boldsymbol{F}^e = \boldsymbol{V}^e \boldsymbol{R}^e$, $\boldsymbol{R}^e = \boldsymbol{1}$	Polar decomposition of $\boldsymbol{F}^e$
$\boldsymbol{F}^{vp} = \boldsymbol{V}^{vp} \boldsymbol{R}^{vp}$	Polar decomposition of $\boldsymbol{F}^{vp}$
$\boldsymbol{l} = \dot{\boldsymbol{F}} \boldsymbol{F}^{-1} = \boldsymbol{l}^e + \boldsymbol{F}^e \boldsymbol{L}^{vp} \boldsymbol{F}^{e-1}$	Spatial velocity gradient
$\boldsymbol{L}^{vp} = \dot{\boldsymbol{F}^{vp}} \boldsymbol{F}^{vp-1} = \boldsymbol{D}^{vp} + \boldsymbol{W}^{vp}$	Additive split of the viscoplastic velocity gradient
$\boldsymbol{C} = \boldsymbol{F}^T \boldsymbol{F}$	Right Cauchy-Green deformation tensor
$\boldsymbol{C}^e = \boldsymbol{F}^{eT} \boldsymbol{F}^e$	Elastic right Cauchy-Green deformation tensor
$\bar{\boldsymbol{F}}$	Microstructural deformation gradient
$\bar{\boldsymbol{l}} = \dot{\bar{\boldsymbol{F}}} \bar{\boldsymbol{F}}^{-1} = \bar{\boldsymbol{d}} + \bar{\boldsymbol{w}} = \eta \boldsymbol{D}^{vp} + \boldsymbol{W}^{vp}$	Microstructural velocity gradient
$\bar{\boldsymbol{C}} = \bar{\boldsymbol{F}}^T \bar{\boldsymbol{F}}$	Microstructural right Cauchy-Green deformation tensor
$\bar{\boldsymbol{b}} = \bar{\boldsymbol{F}} \bar{\boldsymbol{F}}^T$	Microstructural Finger tensor
$\bar{\boldsymbol{e}} = \dfrac{\bar{\boldsymbol{F}} \boldsymbol{e}_0}{\lVert \bar{\boldsymbol{F}} \boldsymbol{e}_0 \rVert}$	Orientation vector

with the driving stress, $\tilde{\boldsymbol{\tau}}^{\mathrm{dev}}$, defined as

$$\tilde{\boldsymbol{\tau}}^{\mathrm{dev}} = \boldsymbol{\tau}^{\mathrm{dev}} - \boldsymbol{B}^{\mathrm{dev}}, \tag{8}$$

where $\boldsymbol{\tau}$ is the Kirchhoff stress and $\boldsymbol{B}$ is the backstress.

The elastic response of the model is assumed to be isotropic and described by the isotropic strain energy ψ^e that is split into a volumetric part and an isochoric part, i.e. $\psi^e = \psi^{e,vol} + \psi^{e,iso}$. The two parts of the elastic free energy are chosen as

$$\psi^{e,vol} = \frac{K_1}{2} (\ln J^e)^2 + K_2 \arctan(\beta(J^e - 1))(J^e - 1) - \frac{K_2}{2\beta} \ln\left((\beta(J^e - 1))^2 + 1\right) \tag{9}$$

and

$$\psi^{e,iso} = 2G J_2^e, \tag{10}$$

where the invariant J_2^e is defined as

$$J_2^e = \frac{1}{2} (\ln \boldsymbol{V}^e)^{\mathrm{dev}} : (\ln \boldsymbol{V}^e)^{\mathrm{dev}}. \tag{11}$$

In the special case of $K_2 = 0$, (9) is reduced to the commonly used quadratic form of the elastic free energy. Comparison of the modelled macroscopic response and those from the experiments presented in Section 4, shows that the quadratic formulation is able to capture the initial macroscopic response during uni-axial deformation, but it predicts a

too stiff biaxial response (see Figure 10). Motivated by this experimental observation, the volumetric free energy is augmented with the term related to K_2, which results in a softer initial response with biaxial deformation. Furthermore, using the proposed form of the elastic free energy it is possible to capture the non-linear, pre-peak behaviour of the material in a more satisfactory manner. In (9) and (10) β, K_1, K_2 and G are model parameters where G represents the initial shear modulus. To get the correct initial stiffness, K_2 is chosen as $K_2 = \frac{K-K_1}{\beta}$ where K is the initial bulk modulus.

Based on the strain energies (9) and (10), the Kirchhoff stress, $\boldsymbol{\tau}$, is given as

$$\boldsymbol{\tau} = 2\boldsymbol{F}^e \frac{\partial \psi^e}{\partial \boldsymbol{C}^e} \boldsymbol{F}^{eT} = \left(K_1 \ln J^e + K_2 J^e \arctan(\beta(J^e - 1))\right) \mathbf{1} + 2G(\ln \boldsymbol{V}^e)^{\text{dev}}. \tag{12}$$

The viscoplastic response is described by the inelastic free energy assumed to be given as

$$\psi^{ie} = n\psi_{chain}, \tag{13}$$

where n is the number of polymer chains per unit volume and ψ_{chain} is the Helmholtz free energy for a single polymer chain taken as

$$\psi_{chain} = kN\theta \left(\lambda_r \mathcal{L}^{-1}(\lambda_r) + \ln \frac{\mathcal{L}^{-1}(\lambda_r)}{\sinh \mathcal{L}^{-1}(\lambda_r)} \right) - \psi_0, \tag{14}$$

cf. Treloar (1975), where k is Boltzmann's constant, $\sqrt{N}$, is the limit stretch of the chain, θ is the absolute temperature, ψ_0 is an arbitrary constant and $\mathcal{L}^{-1}$ is the inverse of the Langevin function defined by $\mathcal{L}[\cdot] = \coth[\cdot] - 1/[\cdot]$. The inverse Langevin function in (14) is evaluated numerically using the Padé approximation proposed by Cohen (1991), i.e. $\mathcal{L}^{-1}(x) \approx x(3 - x^2)/(1 - x^2)$. Similar to the Kirchhoff stress, the backstress is given by (14) as

$$\boldsymbol{B} = 2\eta \bar{\boldsymbol{F}} \frac{\partial \psi^{ie}}{\partial \bar{\boldsymbol{C}}} \bar{\boldsymbol{F}}^T = \eta C_R \sqrt{N} \mathcal{L}^{-1}(\lambda_r) \left(\lambda^{NW}\right)^{1-m} \bar{\boldsymbol{F}} \hat{\boldsymbol{B}} \bar{\boldsymbol{F}}^T, \tag{15}$$

where $C_R = nk\theta$ is the rubber modulus and $\hat{\boldsymbol{B}}$ is

$$\hat{\boldsymbol{B}} = \left\langle \left(\bar{\lambda}\right)^{m-2} \left[\frac{2\text{sym}[\boldsymbol{m}_0 \bar{\boldsymbol{C}}]}{\|\bar{\boldsymbol{F}} \boldsymbol{e}_0\|} - (\bar{\lambda})^2 \boldsymbol{m}_0 \right] \right\rangle, \tag{16}$$

where $\boldsymbol{m}_0 = \boldsymbol{e}_0 \otimes \boldsymbol{e}_0$. The relative network stretch, λ_r, is given as

$$\lambda_r = \frac{\lambda^{NW}}{\sqrt{N}}, \tag{17}$$

where λ^{NW} is the network stretch calculated as the m-root average of the chain stretches, $\bar{\lambda}$, given as

$$\lambda^{NW} = \sqrt[m]{\left\langle (\bar{\lambda})^m \right\rangle}, \tag{18}$$

cf. Miehe et al. (2004). The orientation average of a quantity $[\cdot]$ is given by integration over the surface of the unit sphere $\mathbb{U}^2$. Numerically, the integration is approximated as

$$\langle[\cdot]\rangle = \frac{1}{4\pi}\int_{\mathbb{U}^2}[\cdot]\mathrm{d}A \approx \sum_{i=1}^{M}[\cdot]^i w^i, \tag{19}$$

where the unit sphere is discretised into M points and $w^i_{i=1,\dots,M}$ are the corresponding weight factors. By increasing the number of discretisation points, the accuracy of the numerical integration will increase. This will, however, come at the cost of increasing computational time. Since the evolving anisotropy will result in an alignment of the microstructure into certain directions, 368 integration points will be used to reduce the numerical error, cf. Alastrué et al. (2009).

The chain stretch, $\bar{\lambda}$, related to the change in the end-to-end distance of a polymer chain is chosen as

$$\bar{\lambda} = \sqrt{\bar{\boldsymbol{e}}\cdot\bar{\boldsymbol{b}}\bar{\boldsymbol{e}}}\,. \tag{20}$$

The plastic shear strain rate, $\dot{\gamma}^{vp}$, is given by the double-kink model proposed by Argon (1973) as

$$\dot{\gamma}^{vp} = \dot{\gamma}_0 \exp\left[-\frac{A s_s}{\theta}\left(1-\left(\frac{\tau}{s_s}\right)^{5/6}\right)\right], \quad s_s = s + \alpha p, \tag{21}$$

where $\dot{\gamma}_0$ and A are model parameters, s is the athermal shear stress, the equivalent stress τ is defined in (7), $p = -\frac{1}{3}\mathrm{tr}(\boldsymbol{\sigma})$ is the pressure calculated using the Cauchy stress, $\boldsymbol{\sigma} = \frac{1}{J}\boldsymbol{\tau}$, and α is the pressure dependence factor. The athermal shear stress $s = s_1 + s_2$ is governed by the evolution laws

$$\begin{aligned} \dot{s}_1 &= h_1\left(1-\frac{s_1}{s_{ss}}\right)\dot{\gamma}^{vp}, \quad s_1(0) = s_0, \\ \dot{s}_2 &= h_2\dot{\gamma}^{vp}, \quad s_2(0) = 0, \end{aligned} \tag{22}$$

where h_1, h_2, s_0 and s_{ss} are constitutive parameters. The first part of the athermal shear stress, s_1, is the shear stress from the original model by Boyce et al. (1988) while s_2 was introduced by Holopainen and Wallin (2013) to overcome the problem of over-prediction of the Bauchinger effect on unloading.

6 Numerical evaluation of the model

The capability of the proposed model is demonstrated in this section by simulating the mechanical response of glassy PC during homogeneous and inhomogeneous deformation. First, the model is calibrated to uni-axial and plane strain compression experiments, in which the deformation is assumed to be homogeneous. After this, the model is used to simulate full-scale biaxial deformation experiments with inhomogeneous deformation using the commercial software Abaqus®/Standard. Details on the algorithmic treatment of the model is given by Engqvist et al. (2016b).

6.1 Model calibration

The model was calibrated by fitting the macroscopic stress-strain response to uni-axial compression data from Ames et al. (2009) and plane strain compression data from Boyce et al. (1994). A detailed description of the calibration procedure is given in Engqvist et al. (2016b). By comparing the model response to wide angle X-ray scattering data, Engqvist et al. (2016b) showed that by choosing the microstructural parameter to be $\eta = 0.75$, the orientation of the microstructure was captured accurately by the model. The constitutive parameters, found using a least-square fitting of the model to the experimental data, are found in Table 3. The elastic parameters E, Young's modulus, and ν, Poisson's ratio, were taken from Boyce et al. (1994) whereas K_1 and β were calibrated to fit the experimental biaxial response presented in this study. For the biaxial calibration, a full three dimensional simulation was performed of load case 3, as described in Section 6.2. In addition, the parameter m in (18) was kept fixed at $m = 2$.

Table 3: Constitutive parameters obtained by fitting the model to data for uni-axial compression by Ames et al. (2009) and plane strain compression by Boyce et al. (1994).

E	ν	K_1	β	η	s_0	s_{ss}	h_1	h_2	$\dot{\gamma}_0$	A	C_R	N	α
MPa	-	MPa	-	-	MPa	MPa	MPa	MPa	s^{-1}	$\frac{K}{MPa}$	MPa	-	-
2300	0.3	480	1000	0.75	70.2	34.7	152	26.4	$4.51 \cdot 10^{10}$	342	10.5	2.53	0.10

The macroscopic stress-strain curves from the calibration are shown in Figure 7, presented together with the experimental data. Both sets of tests were performed using a constant strain rate of $|\overline{\ln \lambda}| = 10^{-2}$ s^{-1}. As seen in Figure 7, the calibrated model is able to capture the macroscopic response in a satisfactory manner. Next, the model will be evaluated by comparing the predicted response to the deformation fields measured using DIC.

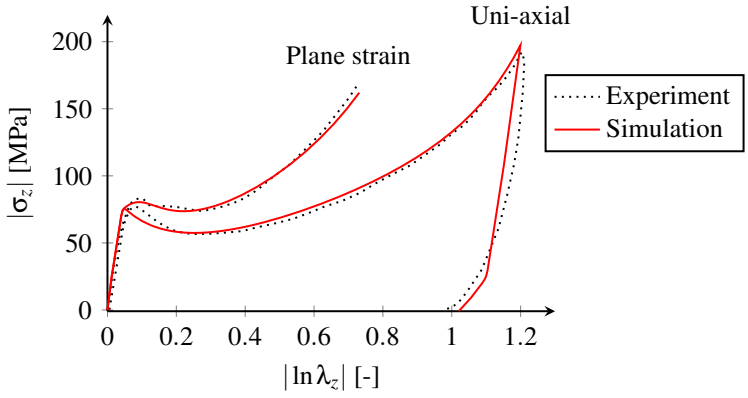

Figure 7: Stress-strain response for uni-axial and plane strain compression from the model (solid lines) and experiment (dotted lines).

6.2 Simulations of biaxial deformation

To demonstrate the predictive ability of the model, the response of glassy PC during biaxial loading has been simulated and compared to results from the experiments discussed in Section 3. The geometry, shown in Figure 1, was discretised using a finite element mesh consisting of 10 404 eight node C3D8 brick elements, see Figure 8. Four elements were used through the thickness of the geometry and a vast majority of the elements were placed around the notches. Due to assumed symmetry in the thickness direction, only one half of the geometry was simulated. The boundary conditions in the simulation are shown in Figure 1.

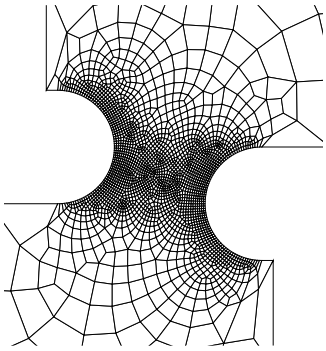

Figure 8: Finite element mesh, zoomed in at the area surrounding the notches.

A comparison of the macroscopic response from the model to that from the experiments is shown in Figure 9 and the model is shown to be able to capture the macroscopic force-displacement response well for all three load cases. The initial stiffness, the pre-peak non-linearity and the overall peak behaviour are captured well by the model. The deviation during unloading is due to a slow response of the test machine when changing from loading to unloading, resulting in some relaxation of the material.

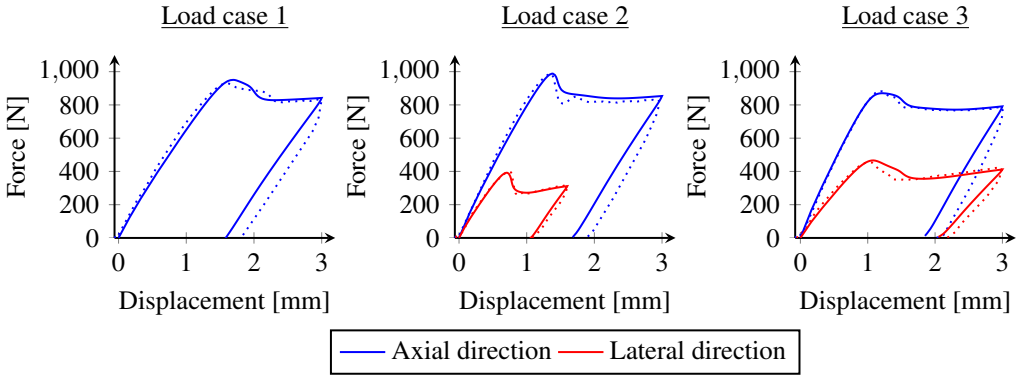

Figure 9: Comparison of the macroscopic response from the proposed model (solid lines) and the experiment (dotted lines).

Figure 10 shows the initial response using the proposed format for the elastic free energy, cf. (9) and (10), and a quadratic format (using the same Young's modulus and Poisson's ratio). The remaining material parameters for the model using the quadratic format of the elastic free energy are taken from Engqvist et al. (2016b). As seen in Figure 10, the conventional quadratic format results in a significantly stiffer initial response, compared to the proposed format and the experimental data. It is also shown that the proposed format (9) is able to capture the non-linear, pre-peak behaviour in a more satisfactory manner than the quadratic format.

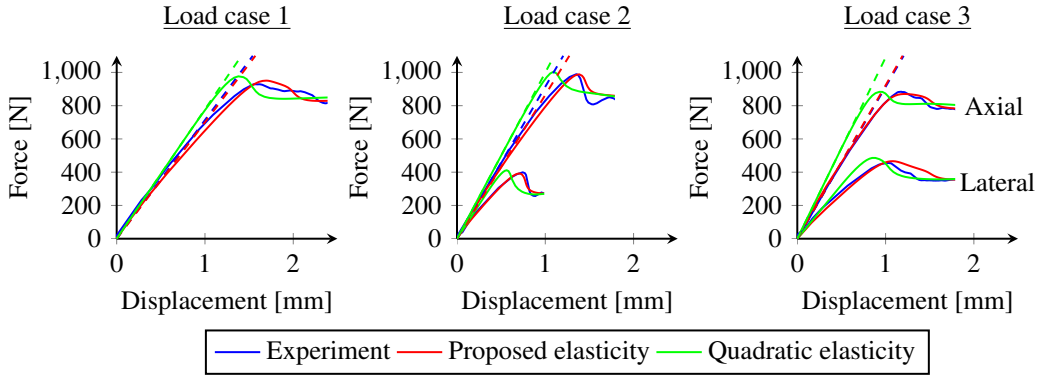

Figure 10: Comparison of the macroscopic initial response from the experiments, the model using the proposed elasticity and the model using the quadratic format of the elastic free energy.

Contour plots of the major principle stretch, λ_1^{DIC}, from the experiments and the simulations are compared qualitatively in Figures 11 to 13. As shown by the contour plots, the model is, to a large extent, able to reproduce the measured deformation fields well. The predicted stretch levels in load steps (iv) and (v) are, however, slightly lower than shown by the experiments and the width of the localisation bands are, in general, somewhat over predicted.

The microstructural deformation gradient, $\bar{\boldsymbol{F}}$, contains information about the anisotropy of the material. To visualise the evolution of the anisotropy, a chain orientation distribution function (CODF), is used. Figure 14 shows the reorientation of the microstructure at the centre point of the specimen for the three load cases. The CODF, used to visualise the microstructure, is defined as

$$F = F_0 \frac{\lambda_{ODF}^3}{\det(\hat{\boldsymbol{F}})} \tag{23}$$

where $\lambda_{ODF} = \|\hat{\boldsymbol{F}}\boldsymbol{e}_0\|$, $\hat{\boldsymbol{F}} = \boldsymbol{F}^e\bar{\boldsymbol{F}}$ is the mapping of the microstructure to the current configuration and F_0 is the value of the CODF in the reference configuration. It is assumed that the initial state of the material is isotropic and homogeneous, i.e. $F_0 = \frac{1}{4\pi}$ (cf. Harrysson et al. (2010); Dafalias (2001)).

The CODFs in Figure 14 show a significant evolution of the anisotropy of the material at the centre point between the notches. As seen in Figure 14, the reorientation of the

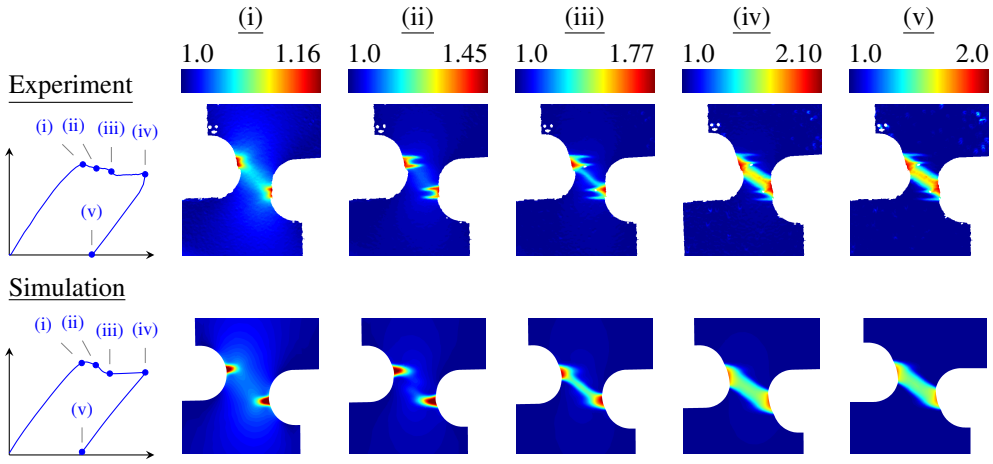

Figure 11: A comparison of the contour plots of the major principle stretch, λ_1^{DIC}, from the experiments and the simulation for load case 1.

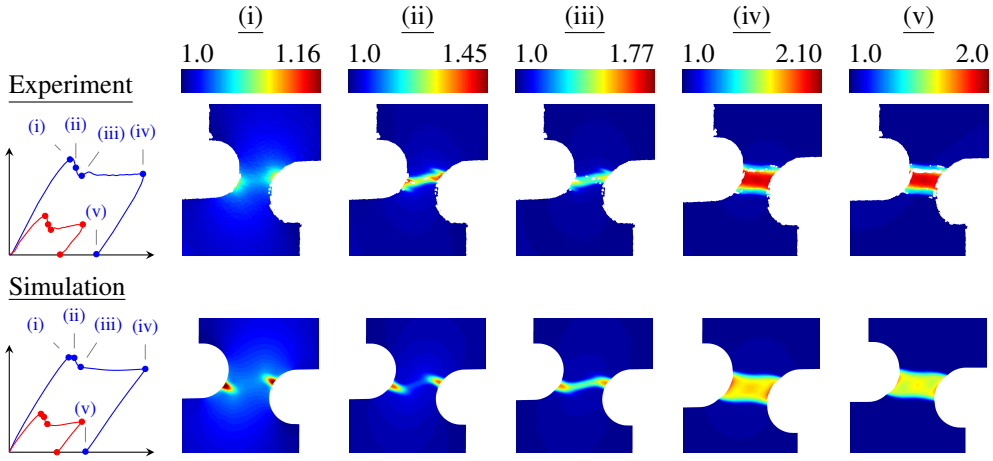

Figure 12: A comparison of the contour plots of the major principle stretch, λ_1^{DIC}, from the experiments and the simulation for load case 2.

microstructure at the centre point is modest before passing the macroscopic force peak at load step (iii). The considerably reorientation taking place between load steps (ii) and (iii) is, as seen in Figures 11 to 13, related to the formation of the localisation band connecting the two notches. As the macroscopic loading continuous, the alignment gets more pronounced.

The degree of anisotropy and the orientation can be quantified using the anisotropy factor, AF, and the orientation angle, χ (proposed by Cinader and Burghardt (1998) to characterise the anisotropy of 2D azimuthal profiles of small angle X-ray scattering data). AF takes the value 0 for isotropy and 1 for perfect orientation. Details about AF and χ are given in Appendix A.

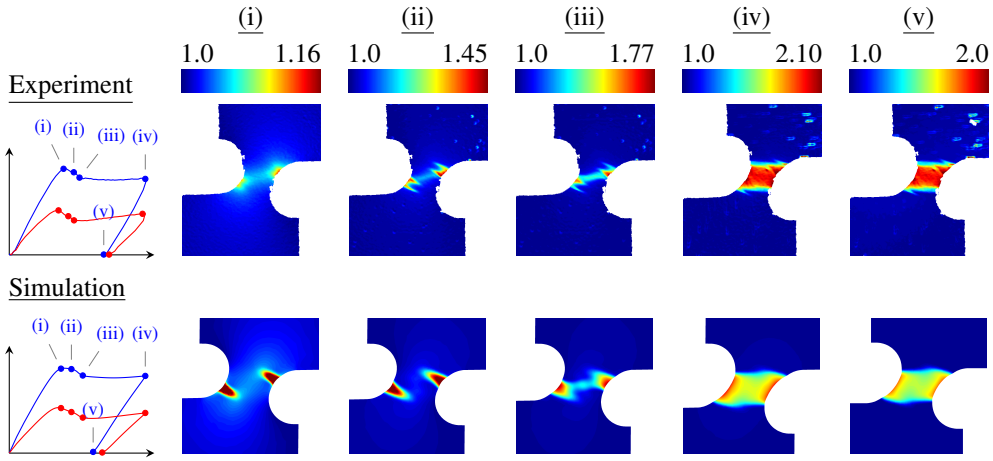

Figure 13: A comparison of the contour plots of the major principle stretch, λ_1^{DIC}, from the experiments and the simulation for load case 3.

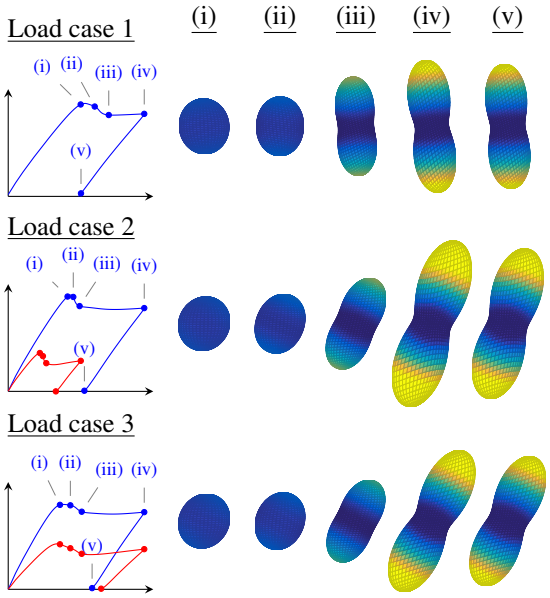

Figure 14: Visualisation of the evolving orientation of the microstructure at the centre point of the specimen for the three load cases using the CODF defined in (23). The colors of the CODFs are to emphasis the amount of orientation.

Figure 15 shows AF and χ of the CODFs from the centre point of the specimen, for the three load cases. Both quantities in Figure 15 are shown as functions of the local value of the major principle stretch, λ_1^{DIC}, extracted from the model at the centre point of the specimens. In Figure 15b, 0° corresponds to the direction parallel to the axial direction.

The evolution of the anisotropy for the three load cases is shown in Figure 15a. As the

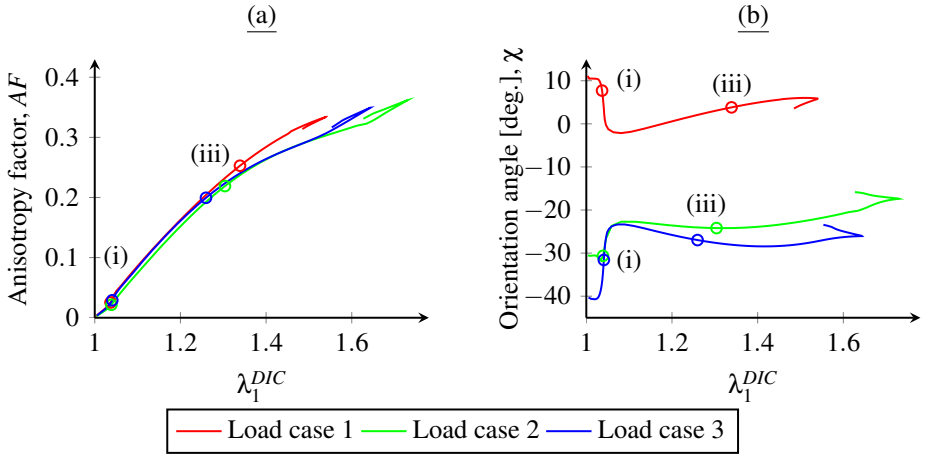

Figure 15: Evolution of the anisotropy factor, AF, of the CODF and the average orientation angle,χ, of the CODF at the centre point of the specimen for the three load cases. Both quantities are plotted as functions of the local value of the major principle stretch, λ_1^{DIC}. As reference points, load steps (i) and (iii) (shown in Figure 14) are marked on the curves.

local stretch increases, the degree of anisotropy increases, from an initial isotropic state, in a similar fashion for all load cases, even though load case 1 shows a slightly higher degree of anisotropy in the later stage of the loading. During unload, all load cases show an decreasing degree of anisotropy.

While the evolution of AF is similar, the average orientation angle shown in Figure 15b differs significantly between the three load cases. This can also been seen in Figure 14, which shows a different rotation angle of the CODFs for the three load cases. The curves in Figure 15b show a rapid change of the orientation angle when approaching the macroscopic force peak at $\lambda_1^{DIC} \approx 1.05$ (at load step (i)). As the local stretch increases further, the orientation angles for both load cases 1 and 3 deviate more from an alignment towards the axial direction (0°). For load case 2, the orientation angle is almost constant until load step (iii), after which the angle increases towards 0°.

7 Concluding remarks

The biaxial tension experiments performed in this work show that the mechanical response of glassy PC is significantly influenced, both on the macroscopic and mesoscopic scale, by the amount of lateral deformation. The deformation fields, measured using DIC, reveal a large difference in the localisation behaviour depending on the loading. In two of the load cases, the strain localisation is initiated as two pair of smaller localisation bands, which evolve into a single localisation going across the specimen. For the third load case, a single localisation band going across the specimen is formed directly and the smaller bands is not as pronounced as for the other load cases.

The experimental results have been used to evaluate and refine the physically-motivated

constitutive model developed by Engqvist et al. (2016b). By deforming PC specimens biaxially, it is found that, even though the model by Engqvist et al. is able to capture the uni-axial response in a satisfactory manner, the initial biaxial response is too stiff. To this end, a new format of the elastic free energy is proposed that results in a better prediction of the initial response during biaxial loading. The proposed format for the elastic free energy also results in a better prediction of the non-linear pre-peak behaviour and an overall better prediction of the macroscopic peak. It should be noted that to observe the deviation in the initial response, experiments performed under multi-axial loading were required. Using the proposed format of the elastic free energy, the model is able to capture the macroscopic mechanical response for the three load cases considered within this study. The model is also able to capture well the overall mesoscopic response in terms of the strain field, compared to full-field 3D-surface DIC.

Acknowledgement

The financial support from the Crafoord foundation, grant no. 20110521, 20120632 and 20151017 is greatly acknowledged.

A Anisotropy tensor

The anisotropy tensor proposed by Cinader and Burghardt (1998) is defined as

$$\boldsymbol{A} = \begin{bmatrix} A_{11} & A_{12} \\ A_{21} & A_{22} \end{bmatrix} = \begin{bmatrix} \{\cos^2\phi\} & \{\cos\phi\sin\phi\} \\ \{\cos\phi\sin\phi\} & \{\sin^2\phi\} \end{bmatrix}, \tag{24}$$

where $\{[\cdot]\}$ is

$$\{[\cdot]\} = \frac{\int_0^\pi [\cdot] F(\phi) \mathrm{d}\phi}{\int_0^\pi F(\phi) \mathrm{d}\phi} \tag{25}$$

calculated from a 2D profile of the outer contours of the CODF projected onto the xy-plane, cf. Figure 1b. In (24) and (25), ϕ is the azimuthal angle and $F(\phi)$ is the value of the CODF as a function of the azimuthal angle. Cinader and Burghardt (1999) introduced the anisotropy factor as the difference between the eigenvalues of $\boldsymbol{A}$, i.e.,

$$AF = \sqrt{(A_{11} - A_{22})^2 + 4A_{12}^2}, \tag{26}$$

which is 0 for isotropy and 1 for perfect orientation. The average orientation angle, χ, is given by the direction of the eigenvector associated to the largest eigenvalue of $\boldsymbol{A}$.

References

Alastrué, V., Martinez, M., Doblaré, M., Menzel, A., 2009. Anisotropic micro-sphere-based finite elasticity applied to blood vessel modelling. Journal of the Mechanics and Physics of Solids 57 (1), 178–203.

Ames, N. M., Srivastava, V., Chester, S. A., Anand, L., 2009. A thermo-mechanically coupled theory for large deformations of amorphous polymers. Part II: Applications. International Journal of Plasticity 25 (8), 1495–1539.

Anand, L., Gurtin, M. E., 2003. A theory of amorphous solids undergoing large deformations, with application to polymeric glasses. International Journal of Solids and Structures 40 (6), 1465–1487.

Argon, A., 1973. A theory for the low-temperature plastic deformation of glassy polymers. Philosophical Magazine 28 (4), 839–865.

Arruda, E. M., Boyce, M. C., 1991. Evolution of plastic anisotropy in amorphous polymers during finite straining. In: Boehler, J.-P., Khan, A. S. (Eds.), Anisotropy and Localization of Plastic Deformation. Elsevier Applied Science, London, pp. 483–488.

Arruda, E. M., Boyce, M. C., 1993. A three-dimensional constitutive model for the large stretch behavior of rubber elastic materials. Journal of the Mechanics and Physics of Solids 41 (2), 389–412.

Arruda, E. M., Boyce, M. C., Jayachandran, R., 1995. Effects of strain rate, temperature and thermomechanical coupling on the finite strain deformation of glassy polymers. Mechanics of Materials 19 (2), 193–212.

Avril, S., Bonnet, M., Bretelle, A.-S., Grediac, M., Hild, F., Ienny, P., Latourte, F., Lemosse, D., Pagano, S., Pagnacco, E., et al., 2008. Overview of identification methods of mechanical parameters based on full-field measurements. Experimental Mechanics 48 (4), 381–402.

Borgqvist, E., Wallin, M., Ristinmaa, M., Tryding, J., 2015. An anisotropic in-plane and out-of-plane elasto-plastic continuum model for paperboard. Composite Structures 126, 184–195.

Boyce, M., Arruda, E., 1990. An experimental and anaiytical investigation of the large strain compressive and tensile response of glassy polymers. Polymer Engineering & Science 30 (20), 1288–1298.

Boyce, M. C., Arruda, E. M., Jayachandran, R., 1994. The large strain compression, tension, and simple shear of polycarbonate. Polymer Engineering & Science 34 (9), 716–725.

Boyce, M. C., Parks, D. M., Argon, A. S., 1988. Large inelastic deformation of glassy polymers. Part I: rate dependent constitutive model. Mechanics of Materials 7 (1), 15–33.

Chevalier, L., Calloch, S., Hild, F., Marco, Y., 2001. Digital image correlation used to analyze the multiaxial behavior of rubber-like materials. European Journal of Mechanics - A/Solids 20 (2), 169–187.

Chowdhury, K., Talreja, R., Benzerga, A. A., 2008. Effects of manufacturing-induced voids on local failure in polymer-based composites. Journal of Engineering Materials and Technology 130 (2), 021010.

Cinader, D. K., Burghardt, W. R., 1998. Mixed orientation state induced by expansion flow of a thermotropic liquid-crystalline polymer. Macromolecules 31 (25), 9099–9102.

Cinader, D. K., Burghardt, W. R., 1999. X-ray scattering studies of orientation in channel flows of a thermotropic liquid–crystalline polymer. Journal of Polymer Science Part B: Polymer Physics 37 (24), 3411–3428.

Cohen, A., 1991. A Padé approximant to the inverse Langevin function. Rheologica Acta 30 (3), 270–273.

Dafalias, Y. F., 2001. Orientation distribution function in non-affine rotations. Journal of the Mechanics and Physics of Solids 49 (11), 2493–2516.

Dreistadt, C., Bonnet, A.-S., Chevrier, P., Lipinski, P., 2009. Experimental study of the polycarbonate behaviour during complex loadings and comparison with the Boyce, Parks and Argon model predictions. Materials & Design 30 (8), 3126–3140.

Engqvist, J., Wallin, M., Hall, S. A., Ristinmaa, M., Plivelic, T. S., 2016a. Measurement of multi-scale deformation of polycarbonate using x-ray scattering with in-situ loading and digital image correlation. Polymer 82, 190–197.

Engqvist, J., Wallin, M., Ristinmaa, M., Hall, S. A., Plivelic, T. S., 2016b. Modelling multi-scale deformation of amorphous glassy polymers with experimentally motivated evolution of the microstructure.

Grytten, F., Daiyan, H., Polanco-Loria, M., Dumoulin, S., 2009. Use of digital image correlation to measure large-strain tensile properties of ductile thermoplastics. Polymer Testing 28 (6), 653–660.

Harrysson, A., Ristinmaa, M., 2008. Large strain elasto-plastic model of paper and corrugated board. International Journal of Solids and Structures 45 (11), 3334–3352.

Harrysson, M., Ristinmaa, M., Wallin, M., Menzel, A., 2010. Framework for deformation induced anisotropy in glassy polymers. Acta Mechanica 211 (3-4), 195–213.

Hasan, O., Boyce, M., 1995. A constitutive model for the nonlinear viscoelastic viscoplastic behavior of glassy polymers. Polymer Engineering & Science 35 (4), 331–344.

Hild, F., Roux, S., 2006. Digital image correlation: from displacement measurement to identification of elastic properties–a review. Strain 42 (2), 69–80.

Holopainen, S., Wallin, M., 2013. Modeling of the Long-Term Behavior of Glassy Polymers. Journal of Engineering Materials and Technology 135 (1), 011001.

Hu, Y., Xia, Z., Ellyin, F., 2003. Deformation behavior of an epoxy resin subject to multiaxial loadings. part i: Experimental investigations. Polymer Engineering & Science 43 (3), 721–733.

Johlitz, M., Diebels, S., 2011. Characterisation of a polymer using biaxial tension tests. part i: Hyperelasticity. Archive of Applied Mechanics 81 (10), 1333–1349.

Miehe, C., Diez, J. M., Göktepe, S., Schänzel, L.-M., 2011. Coupled thermoviscoplasticity of glassy polymers in the logarithmic strain space based on the free volume theory. International Journal of Solids and Structures 48 (13), 1799–1817.

Miehe, C., Göktepe, S., Diez, J. M., 2009. Finite viscoplasticity of amorphous glassy polymers in the logarithmic strain space. International Journal of Solids and Structures 46 (1), 181–202.

Miehe, C., Göktepe, S., Lulei, F., 2004. A micro-macro approach to rubber-like materials – Part I: the non-affine micro-sphere model of rubber elasticity. Journal of the Mechanics and Physics of Solids 52 (11), 2617–2660.

Parsons, E., Boyce, M., Parks, D., 2004. An experimental investigation of the large-strain tensile behavior of neat and rubber-toughened polycarbonate. Polymer 45 (8), 2665–2684.

Parsons, E., Boyce, M., Parks, D., Weinberg, M., 2005. Three-dimensional large-strain tensile deformation of neat and calcium carbonate-filled high-density polyethylene. Polymer 46 (7), 2257–2265.

Poulain, X., Kohlman, L., Binienda, W., Roberts, G., Goldberg, R., Benzerga, A., 2013. Determination of the intrinsic behavior of polymers using digital image correlation combined with video-monitored testing. International Journal of Solids and Structures 50 (11), 1869–1878.

Ravi-Chandar, K., Ma, Z., 2000. Inelastic deformation in polymers under multiaxial compression. Mechanics of Time-Dependent Materials 4 (4), 333–357.

Tomita, Y., 2000. Constitutive modelling of deformation behavior of glassy polymers and applications. International Journal of Mechanical Sciences 42 (8), 1455–1469.

Treloar, L., Riding, G., 1979. A non-Gaussian theory for rubber in biaxial strain. I. Mechanical properties. In: Proceedings of the Royal Society of London A: Mathematical, Physical and Engineering Sciences. Vol. 369. The Royal Society, pp. 261–280.

Treloar, L. R. G., 1975. The physics of rubber elasticity. Oxford University Press, USA.

Wang, M. C., Guth, E., 1952. Statistical theory of networks of non-gaussian flexible chains. The Journal of Chemical Physics 20, 1144.

Wu, P., van der Giessen, E., 1993. On improved network models for rubber elasticity and their applications to orientation hardening in glassy polymers. Journal of the Mechanics and Physics of Solids 41 (3), 427–456.